PHASE SELECTION IN THE K500 CYCLOTRON AND THE DEVELOPMENT OF A NON-LINEAR TRANSFER MATRIX PROGRAM

by

Bruce Forrest Milton

A DISSERTATION

Submitted to
Michigan State University
in partial fulfillment of the requirements
for the degree of

DOCTOR OF PHILOSOPHY

Department of Physics and Astronomy

1986

ABSTRACT

PHASE SELECTION IN THE K500 CYCLOTRON
AND THE DEVELOPMENT OF A NON-LINEAR
TRANSFER MATRIX PROGRAM

By

Bruce Forrest Milton

A method has been developed for the rapid calculation of particle orbits in a cyclotron with spiral-shaped dees. The method uses second order matrix transfer methods and has been implemented in the FORTRAN program "SOMA", (Second Order MAtrix). SOMA has been checked against the slower orbit integration program SPRGAPZ. A combination of SPRGAPZ and SOMA has been used to investigate the phase selection process in the Michigan State University K500 cyclotron. This study led to the design of hardware necessary for phase selection and the ancillary beam diagnostic equipment. Finally SOMA calculations and the phase selection calculations are compared to experimental results.

ACKNOWLEDGMENTS

I would like to thank Dr. Henry Blosser for giving me the opportunity to work at this unique laboratory. I am also deeply indebted to Dr. Morton Gordon for the help with the transfer matrix program, and Dr. Felix Marti whose patient guidance and assistance kept me going.

Thanks are also due to all those many cyclotron employees with whom I have had the pleasure of working. I have learnt much from their experience and will always remember the comraderie.

Finally I would like to thank my parents, both of whom showed me that this was possible, and without whose constant love and support this wouldn't have been possible.

TABLE OF CONTENTS

List of Tables

List of Tables

List of Figures

Figure

Page

Figure

Page

Figure

Page

Figure

Page

Figure

Page

Figure

Page

Figure

Page

Figure

Page

1. Introduction

At present the majority of accelerator studies at the National Superconducting Cyclotron Laboratory are devoted to two cyclotrons, the K500 and the K800. The K500 cyclotron has been in operation since 1982, and is running a regular schedule of experiments. The K800 is under construction and is expected to begin testing with beam in 1987. In the case of the K500 the effort is directed at improving beam quality and intensity, while K800 work is devoted to more fundamental design considerations. The two cyclotrons have many similarities; size is their most obvious difference. The material reported here will be dealing only with the K500, but in most cases is equally applicable to the K800.

The K500 cyclotron at Michigan State University[1,2,3] is a multi-particle, variable-energy machine. The bending limit is K_b =520 MeV, and the focusing limit is K_f=160 MeV, where the energy limit in MeV/u is either $K_b(Q/A)^2$ or $K_f(Q/A)$, whichever is smaller[4]. The compact magnet has a pill-box-shaped yoke that completely encloses the cyclotron. The main field is produced by two pairs of circular superconducting coils located just beyond the extraction radius (see Figures 1-1 and 1-2). The flutter is created by three spiral-shaped

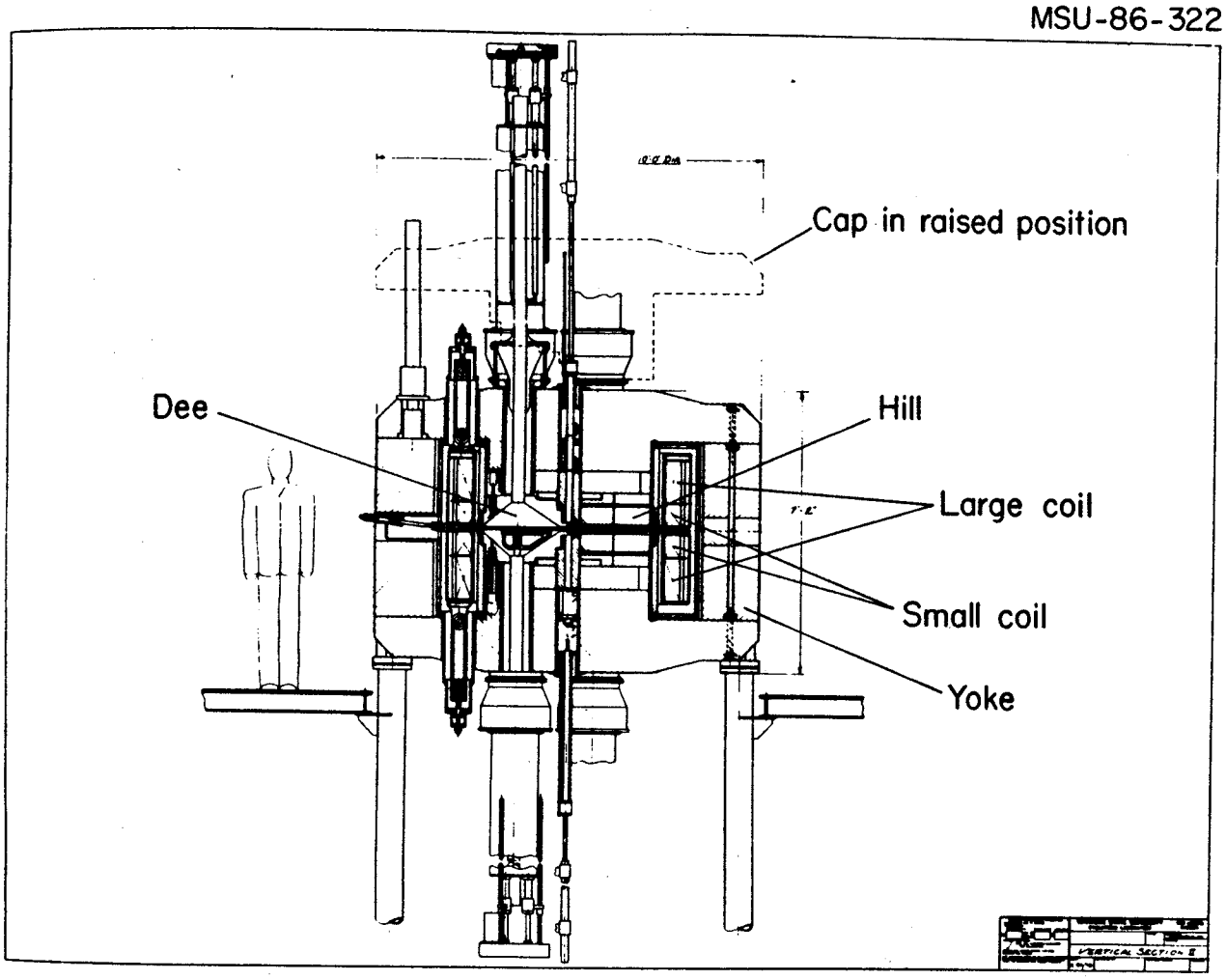

Figure 1-1. Vertical section of the K500 cyclotron.

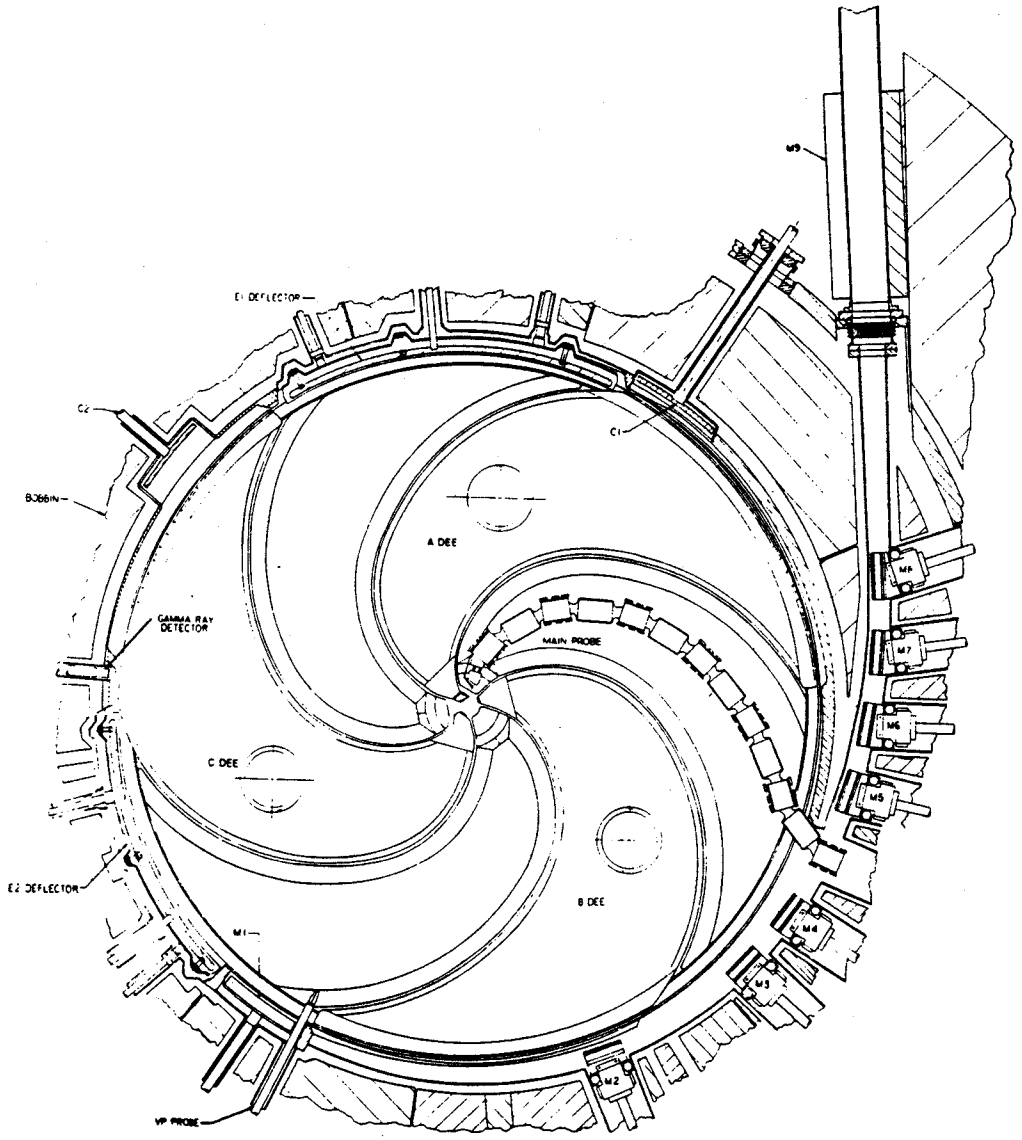

Figure 1-2. Median plane view of the K500 cyclotron. "A" hill is located between the "C" dee and the "A" dee.

hills. The magnet gap on the hills is 6.54 cm. The RF system[5,6] consists of three dees located in the valleys between the hills (where the magnet gap is 36"), and can be operated over a frequency range of 9 MHz to 27 MHz. Figure 1-3 shows the range of energies and charge states that can be accelerated. Originally the K500 ran with an internal Penning Ion Source (PIG), but as of March 1986 it has been coupled to an Electron Cyclotron Resonance (ECR) ion source[7].

The K500 cyclotron has several unique features that make it an interesting case study. The high magnetic field (B_0=3T to 5T) leads to a very compact magnet design, which in turn leads to a small separation between turns of the internal beam. The small size of the cyclotron necessitates that all the attached hardware must be compact in nature, as space is at a premium. The small magnet gap and the tight spiral result in a median plane field with large gradients. In general these features place stringent requirements on any approximations that are made. Because the dees are spiral shaped, the azimuth of the gap crossing is a function of radius, consequently dealing appropriately with the gaps adds an additional complication to any orbit computation routines[8].

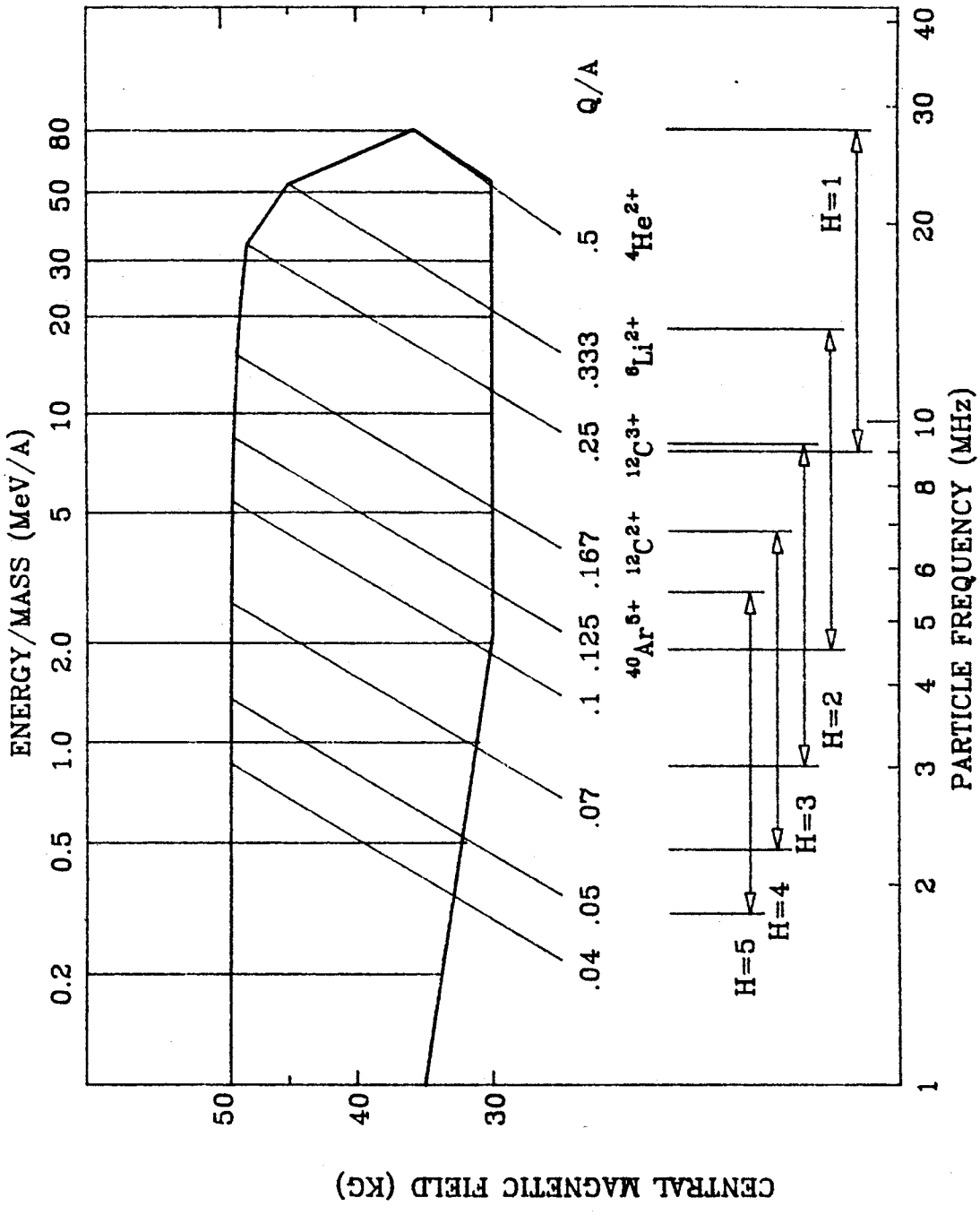

Figure 1-3. The K500 operating diagram.

Transfer matrix programs[9, 37] provide the ability to compute many orbits in a relatively short time. This greatly facilitates the investigation of bulk properties of the beam. In addition, these codes are quite powerful for simulating the output that would be obtained from a diagnostic device such as a beam probe under different operating conditions. Unfortunately none of the transfer matrix codes available were suitable for use with the K500 cyclotron because of the spiral shaped dees, and the large field derivatives, so the program SOMA (Second Order Matrix Approximation) was developed. The design of this program will be the subject of chapter 2.

Most of the time it is desirable to run the cyclotron in a manner that gives the most extracted current. Of course there are exceptions, and in many such cases it is desirable to reduce the phase spread of the beam, thus improving the time resolution of the beam, and reducing the loss of internal beam on cyclotron components[10]. One such situation is accelerator studies where the ability to observe distinct turns is a major advantage. Phase selection of the internal beam using the coupling between the horizontal and longitudinal motions has been used for many years, but nevertheless every such system requires a detailed

investigation of its feasibility. Such an investigation will be presented in chapter 3. In the case of the K500 the highly non-linear nature of the central region and the low number of turns involved makes orbit tracking with a numerical integration program the preferred choice. After the central region, the transfer matrix code provides a rapid method of tracking the selected beam to extraction. This makes comparison of experimental results to computations much faster.

In order to perform phase selection in the K500 cyclotron a rather intricate set of hardware was constructed[11], and this will be presented in chapter 4. This hardware had to provide the necessary control functions, within the constraints of the limited space available and the high magnetic field. As a result a large effort was put into the construction and installation of the drive mechanism. The construction of the viewer port (V.P.) probe allowed for improved beam diagnostics which helped in understanding the beam behaviour with the slits in place. Also the V.P. probe drive made use of the gamma probe convenient and easy . The γ probe allowed the direct measurement of the internal beam's phase width, so it was invaluable for observing the results of the phase slits.

In chapter 5 the results from a set of measurements of orbit properties in the K500 cyclotron are presented. Most of the measurements seek to confirm the computed magnetic properties rather than discover unknowns. As will be seen the agreement between running conditions and computations is quite good. The measurements also confirm that the phase selection system operates in a manner consistent with the calculations of chapter 3.

2. SOMA: A Cyclotron Orbit Code Using Second Order Transfer Matrices

2.1 Introduction

For many years computer programs for the design of charged particle transport systems have made use of a matrix algebra formalism. The procedure is based on the fact that to first order the final conditions may be expressed as simple integrals of a few particular first order trajectories (matrix elements) characterizing a system. In these codes; beam-line elements are represented by idealized components for which the trajectories were derived analytically. The programs then compute a transfer matrix for the whole system by multiplying together the transfer matrices for each of the elements in the system. The results provide rapid physical insight into the design of systems, leaving ray tracing to final design confirmation, and the computation of higher order effects. In a procedure described by K. Brown[12], this technique was generalized to include second order effects in the very successful program "TRANSPORT". Some years ago a simple extension of the

transfer matrix ideas in beamline codes was made to allow them to be used for the design of synchrotrons. Today several matrix programs for synchrotron design exist that correctly treat second and even higher order abberations.

The extension to cyclotrons is more difficult since the beam path does not consist of a set of discrete single function elements, but rather a single, very complex magnetic field, which varies as a function of radius and therefore as a function of energy. The well known solution to this problem is to compute the first order trajectories around a closed (equilibrium) orbit, (EO), for a set of energies spanning the range of the cyclotron. Results of this type of calculation are commonly expressed using the variables ω_0, ν_r and ν_z (the orbital, radial and axial focussing frequencies). Historically, as cyclotron running time became more valuable, and computer time less expensive, it became increasingly popular to track orbits in the appropriate magnetic field, in order to have a better understanding of the beam behaviour. When only a small number of orbits need to be tracked in order to understand the overall properties of the system this technique proved to be very valuable. In cases where many orbits need to be followed, the large amount of CPU time required to do the

numerical integration makes this procedure very demanding on the available computer facilities. It was found that in cases where bulk properties such as the radial-longitudinal coupling are being investigated, a high degree of accuracy in the individual orbits is not required. This meant that a program that computed the transfer matrix elements and then used them to determine the orbits of a large group of particles, (each with different starting conditions) would allow rapid investigation of these phenomena.

At TRIUMF (Vancouver, Canada) the first order transfer matrix program "COMA"[9] was developed based on these principles. In this case the transfer matrix elements are computed by the equilibrium orbit code "CYCLOPS"[13] and output at any number of azimuths, for a set of energies. The minimum number of azimuths at which matrices are necessary is determined by the number of accelerating gaps. These matrix coefficients are then fed into COMA, and the program selects a set of initial conditions for a set of particles from a given distribution (see section 2.5). The initial conditions are multiplied by the appropriate first order matrix thus determining the orbit parameters at the first accelerating gap. At the gap a delta function model is used to evaluate the energy gain of the particle. The conditions

at this gap can then be multiplied by the appropriate matrix to determine the conditions at the next gap, and so on. The actual matrix coefficients used are determined by interpolating between the values that were computed by "CYCLOPS", and stored at a set of discrete energies. Tests of "COMA" in a TRIUMF magnetic field[9] show that for static runs in regions away from the stop bands, and with initial displacements as large as 2.0 in. from the EO the errors were similar to the changes that occur when the Runge-Kutta step size is changed. In the case of accelerated orbits a particle with an initial 0.25 in. radial amplitude had an error of 0.001 in. after 165 turns. Checks which involved passing through stop bands showed larger errors, but the results were still usable.

The sucess of "COMA" suggested that such a program would be very useful for accelerator studies at MSU. However two major differences between TRIUMF and the MSU superconducting cyclotrons prevented the direct use of "COMA". The more obvious difference is the accelerating gaps, which follow a spiral in the K500 and K800 cyclotrons, rather than the more conventional radial line. This difference implies a more complicated gap crossing routine, similar to the one implemented in the program "SPRGAPZ"[8]. It also complicates

the bookkeeping, as radial lines (used for output at a constant angle) cross the accelerating gaps. The other important difference is in the magnet structure. The K500 has a high field magnet (5T) with a 6.35 cm gap and a tight spiral, while TRIUMF is a low field magnet (.5T) with a 52.8 cm gap and modest spiral. The smaller magnet gap allows larger azimuthal derivatives of the magnetic field, while the tight spiral generates large radial derivatives. In a transfer matrix program the first order matrix elements are a function of the first derivatives of the magnetic field, while the second order coefficients include terms involving the second derivatives and so on. Thus the more rapidly varying field allows the second order effects to be significantly larger. In fact with initial displacements as small as 0.010" there were significant differences between the transfer matrix program and the orbit integration routine (see 2.6). This was the motivation for developing a transfer matrix code in which the second order effects were included. It should be noted that a transfer matrix program requires that the equilibrium orbit exists. If the magnetic field contains large stop bands such as those that would result if the first harmonic component of the field is large in the region of $\nu_r=1.0$, then this would not be true. This

restricts the use of these programs to cases where resonance crossings are fast and the field imperfections small. A separate treatment for harmonic bump coils will be given in section 2.7.

In the following sections the equations of motion of a charged particle will be developed and then expanded about the equilibrium orbit. After the method by which the solutions to the first order differential equations are found has been demonstrated, the second second order contributions will be computed. Following this the effects of the spiral gap shape will be discussed. Finally there will be an outline of the routines used by SOMA, and some comparison with an orbit integrating program.

The approach used to find the matrix elements is a perturbation expansion, analogous to the Born aproximation in quantum mechanics. First an exact solution is sought for the case where the equations of motion (about the EO) are linear. As is well known, the solutions to this can be found by integrating the orbits of two rays, (displaced from the EO), between the two points for which the transfer is needed. Then the quadratic terms are added to the equations of motion and treated as a perturbation. That is to say that solutions are sought that are a combination of the exact linear solutions (the eigenfunctions of the unperturbed

case). As in the Born approximation the solutions are formed using a Green's function. It will be shown in section 2.2.4 that the Green's function in this case is very simple. It should be noted that because the equations of motion are truncated we no longer have a Hamiltonian and so the solutions are not symplectic.

2.2 Calculation of Transfer Matrix Elements

2.2.1 Equations of Motion

The Hamiltonian with θ as the independent variable, for a charged particle in a magnetic field with median plane symmetry is given by,[14]

$$H = - r\, p_\theta - \frac{1}{b}\, r\, A_\theta \qquad (2\text{-}1)$$

As is done in all the orbit programs currently in use at NSCL, a length unit "a" and a field unit "b" are defined as,

$$a = c/\omega_0 \qquad b = m_0 \omega_0 / q \qquad (2\text{-}2)$$

where $\omega_0 = 2\pi\nu_{rf}/h$ if ν_{rf} is the nominal RF frequency, m_0 is the rest mass, q is the particle charge, c is the velocity of light in vacuum, and h is the harmonic number. We then take the momentum unit to be $m_0 c/a$ so that momenta are expressed in units of length.

Assuming that the magnetic field has median plane symmetry, and is given in the median plane by $B=B(r,\theta)$ then to second order in z, near the median plane:

$$B_z = -B + \frac{1}{2} z^2 \left(\frac{\partial^2 B}{\partial r^2} + \frac{1}{r}\frac{\partial B}{\partial r} + \frac{1}{r^2}\frac{\partial^2 B}{\partial \theta^2}\right),$$

$$B_r = -z\frac{\partial B}{\partial r}, \qquad (2\text{-}3)$$

$$B_\theta = -\frac{z}{r}\frac{\partial B}{\partial \theta}.$$

If the field, B, is divided by the field unit b such that

$$B(r,\theta) \rightarrow B(r,\theta)/b,$$

then Hamilton's equations yield,

$$r' = \frac{dr}{d\theta} = \frac{r\,p_r}{\sqrt{(p^2 - p_r^2 - p_z^2)}},$$

$$p_r' = \frac{dp_\theta}{d\theta} = \sqrt{(p^2 - p_r^2 - p_z^2)} - r\,B_z + z'\,B_\theta,$$

$$z' = \frac{dz}{d\theta} = \frac{r\,p_z}{\sqrt{(p^2 - p_r^2 - p_z^2)}}, \qquad (2\text{-}4)$$

$$p_z' = \frac{dp_z}{d\theta} = z\left(r\frac{\partial B}{\partial r} - \frac{r'}{r}\frac{\partial B}{\partial \theta}\right), \text{ and}$$

$$\tau' = \frac{d\tau}{d\theta} = \frac{\gamma\, r}{\sqrt{(p^2 - p_r^2 - p_z^2)}}$$

(where $\gamma = 1 + E/m_o c^2$).

The zero order solution to these differential equations is known as the Equilibrium Orbit (EO), which, in a magnetic

field having N sectors, and no imperfection, satisfies the periodicity conditions,

$$r_0(\theta + \theta_0) = r_0(\theta) \ , \quad p_{r0}(\theta + \theta_0) = p_{r0}(\theta), \quad \theta_0 = 2\pi/N.$$

We then wish to expand in terms of the displacements ($x, p_x, z,$ and p_z) from the EO where;

$$r = r_0 + x \ , \qquad p_r = p_{r0} + p_x \ , \qquad \tau = \tau_0 + X \ .$$

To simplify the results, we divide the equation for the derivatives into terms of different order in the expansion coefficients. As for notation, the digit in the subscript of each term will refer to the order of that term. Also the second order terms will be separated into those that depend on x^2 (as well as $x\,p_x$ and p_x^2), and those that depend on z^2. Thus the r_{x2} contains the terms in the expansion of r that depend on x^2, $x\,p_x$, and p_x^2. The overall derivatives using this notation are,

$$r' = r'_0 + r'_1 + r'_{x2} + r'_{z2}$$

$$p'_r = p'_{r0} + p'_{r1} + p'_{rx2} + p'_{rz2} \ ,$$

$$z' = z'_1 + z'_2 \ ,$$

$$p'_z = p'_{z1} + p'_{z2} \ ,$$

$$\tau' = \tau'_0 + \tau'_1 + \tau'_{x2} + \tau'_{z2} \ .$$

The results of expanding the equations 2-4 for the derivatives in terms of x, p_x, z, and p_z, and identifying the orders of the various terms is given below. In each of these equations, (which shall be labeled 2-5), where r or p_r appear on the right hand side of the equation, they refer to the values of r or p_r for the equilibrium orbit. Also the equations will use $p_\theta = (p^2 - p_{r0}^2)^{1/2}$, the theta component of the momentum for the EO. The zeroth order components are:

$$r'_0 = r\, p_r / p_\theta ,$$

$$p'_{r0} = p_\theta - r\, B ,$$

$$\tau'_0 = \frac{\gamma\, r}{p_\theta} ;$$

the first order terms are:

$$r'_1 = \frac{p_r}{p_\theta} x + \frac{r\, p^2}{p_\theta^3} p_x ,$$

$$p'_{r1} = - \frac{p_r}{p_\theta} p_x - (B + r \frac{\partial B}{\partial r}) x ,$$

$$z'_1 = \frac{r}{p_\theta} p_z ,$$

$$p'_{z1} = z (r \frac{\partial B}{\partial r} - \frac{p_r}{p_\theta} \frac{\partial B}{\partial \theta}) .$$

$$\tau'_1 = \frac{\gamma}{p_\theta} x + \frac{\gamma r p_r}{p_\theta^3} p_x ;$$

second order terms are:

$$r'_{x2} = \frac{p^2}{p_\theta^3} x p_x + \frac{3}{2} \left(\frac{r p^2 p_r}{p_\theta^5} \right) p_x^2 ,$$

$$r'_{z2} = \frac{1}{2} \frac{r p_r}{p_\theta^3} p_z^2 ,$$

$$p'_{rx2} = - \frac{1}{2} \frac{p^2}{p_\theta^3} p_x^2 - \frac{1}{2} \left(2 \frac{\partial B}{\partial r} + r \frac{\partial^2 B}{\partial r^2} \right) x^2 ,$$

$$p'_{rz2} = - \frac{1}{2} \frac{p_z^2}{p_\theta} + \frac{1}{2} r \left(\frac{\partial^2 B}{\partial r^2} + \frac{1}{r} \frac{\partial B}{\partial r} + \frac{1}{r^2} \frac{\partial^2 B}{\partial \theta^2} \right) z^2 + \frac{1}{p_\theta} \frac{\partial B}{\partial \theta} z p_z ,$$

$$z'_2 = p_z \left(\frac{x}{p_\theta} + \frac{r p_r}{p_\theta^3} p_x \right) ,$$

$$p'_{z2} = z \left(\frac{\partial B}{\partial r} + r \frac{\partial^2 B}{\partial r^2} - \frac{p_r}{p_\theta} \frac{\partial^2 B}{\partial r \partial \theta} \right) x - \frac{p^2}{p_\theta^3} \frac{\partial B}{\partial \theta} z p_x ,$$

$$\tau'_{x2} = \frac{\gamma p_r}{p_\theta^3} x p_x + \frac{1}{2} \frac{\gamma r}{p_\theta^3} \left(1 + 3 \frac{p_r^2}{p_\theta^2} \right) p_x^2 ,$$

$$\tau'_{z2} = \frac{1}{2} \frac{\gamma r}{p_\theta^3} p_z^2 .$$

The procedure for finding r_o and p_{ro} is the same as that used in the equilibrium orbit codes "GENSPEO" and "CYCLOPS", and is described in detail in reference 13. The method for

finding the first and second order matrices will be discussed in the next two sections.

2.2.2 First Order Matrix

In order to find the first order transfer matrices X and Z as defined by,

$$\begin{pmatrix} x \\ p_x \end{pmatrix}_{\theta_f} = X(\theta_f, \theta_i) \begin{pmatrix} x \\ p_x \end{pmatrix}_{\theta_i}$$

$$\begin{pmatrix} z \\ p_z \end{pmatrix}_{\theta_f} = Z(\theta_f, \theta_i) \begin{pmatrix} z \\ p_z \end{pmatrix}_{\theta_i},$$

we need two independent solutions, denoted (x_1, p_{x1}) and (x_2, p_{x2}) to the equations for x', p_x' and two solutions denoted (z_1, p_{z1}) and (z_2, p_{z2}) for the equations for z' and p_z'. We also require the correction, X, to the time coordinate, (τ), such that for a displaced orbit $\tau \rightarrow \tau + X$. For an orbit with initial displacements $x(\theta_i)$ and $p_x(\theta_i)$, X will be given by,

$$X(\theta_f) = X_1(\theta_f, \theta_i)\, x(\theta_i) + X_2(\theta_f, \theta_i)\, p_x(\theta_i)$$

were X_1 and X_2 are to be found. It proves most convenient to choose the initial conditions,

$$x_1(\theta_i) = 1 \qquad p_{x1}(\theta_i) = 0$$

$$x_2(\theta_i) = 0 \qquad p_{x2}(\theta_i) = 1$$

$$z_1(\theta_i) = 1 \qquad p_{z1}(\theta_i) = 0$$

$$z_2(\theta_i) = 0 \qquad p_{z2}(\theta_i) = 1 .$$

because then,

$$X(\theta_f, \theta_i) = \begin{bmatrix} x_1(\theta_f) & x_2(\theta_f) \\ p_{x1}(\theta_f) & p_{x2}(\theta_f) \end{bmatrix} ,$$

$$Z(\theta_f, \theta_i) = \begin{bmatrix} z_1(\theta_f) & z_2(\theta_f) \\ p_{z1}(\theta_f) & p_{z2}(\theta_f) \end{bmatrix} ,$$

$$X_1' = \gamma \left[\frac{x_1}{p_\theta} + \frac{r\, p_r}{p_\theta^3} p_{x1} \right] ,$$

$$X_2' = \gamma \left[\frac{x_2}{p_\theta} + \frac{r\, p_r}{p_\theta^3} p_{x2} \right] .$$

The values of x_1, p_{x1} etc. are computed by integrating the first order equations (2-5) along the equilibrium orbit between θ_i and θ_f. As in all our orbit codes, the integration routine uses the Runge - Kutta method of Gill[15], with a step size of two degrees.

2.2.3 Second Order Matrix Elements

In the case of a first order transfer, where the final conditions are given as linear functions of the initial conditions, the results are exact solutions of the differential equations obtained when the equations of motion

are expanded to first order . When the final conditions are given to second order in the initial conditions, the results are an approximate solution to the differential equations that are a result of a second order expansion. Inherent in this difference is that the method of finding the second order matrix elements must be different from that used to find the first order elements. The approach outlined below is similar to that used by K. Brown[12]. In this approach the orbits are to be given as a second order Taylor expansion in the initial displacements from the equilibrium orbit. It is then required that the expanded orbits satisfy a set of differential equations that have been formed by expanding the equations of motion to second order. For the first order expansion coefficients this generates a set of first order homogeneous, linear differential equations. For the second order expansion coefficients the differential equations are similar except that they are not homogeneous. The non-homogeneous part of the equations has the form of a driving function. Finally the second order coefficients are evaluated via a Green's function integral containing the driving function of the particular coefficient, and the solutions of the homogeneous equations.

A convenient statement of the problem is that we require the matrices A , D and E as defined by,

$$\begin{pmatrix} x \\ p_x \end{pmatrix}_{\theta_f} = X(\theta_f, \theta_i) \begin{pmatrix} x \\ p_x \end{pmatrix}_{\theta_i} + A(\theta_f, \theta_i)\ V(\theta_i)$$

$$\begin{pmatrix} z \\ p_z \end{pmatrix}_{\theta_f} = Z(\theta_f, \theta_i) \begin{pmatrix} z \\ p_z \end{pmatrix}_{\theta_i} + D(\theta_f, \theta_i)\ V(\theta_i)$$

$$X(\theta_f) = X_1\ x(\theta_i) + X_2\ p_x(\theta_i) + E(\theta\ , \theta_i)\ V(\theta_i)$$

where,

$$V(\theta) = \begin{bmatrix} x^2 \\ x\ p_x \\ p_x^2 \\ x\ z \\ x\ p_z \\ p_x\ z \\ p_x\ p_z \\ z^2 \\ z\ p_z \\ p_z^2 \end{bmatrix}_\theta$$

Inspection of the differential equations 2-5 shows that some of the rows of A and D will be identically zero, so to eliminate carrying these rows we define,

$$V_x(\theta) = \begin{bmatrix} x^2 \\ x\ p_x \\ p_x^2 \\ z^2 \\ z\ p_z \\ p_z^2 \end{bmatrix}_\theta \qquad V_z(\theta) = \begin{bmatrix} x\ z \\ x\ p_z \\ p_x\ z \\ p_x\ p_z \end{bmatrix}_\theta$$

Thus the equations become,

$$\begin{pmatrix} x \\ p_x \end{pmatrix}_\theta = X(\theta, \theta_i) \begin{pmatrix} x \\ p_x \end{pmatrix}_{\theta_i} + A(\theta, \theta_i)\ V_x(\theta_i)\ ,$$

$$\begin{pmatrix} z \\ p_z \end{pmatrix}_\theta = Z(\theta, \theta_i) \begin{pmatrix} z \\ p_z \end{pmatrix}_{\theta_i} + D(\theta, \theta_i)\ V_z(\theta_i)\ , \qquad (2\text{-}6)$$

$$X(\theta) = X_1(\theta)\ x(\theta_i) + X_2(\theta)\ p_x(\theta_i) + E(\theta, \theta_i)\ V_x(\theta_i).$$

The elements of matrices A and D are simply the second order coefficients of a Taylor's expansion of the coordinates. If the differential equations (2-5) are written in matrix notation, then they become;

$$\frac{d}{d\theta}\begin{pmatrix} x \\ p_x \end{pmatrix}_\theta = K(\theta) \begin{pmatrix} x \\ p_x \end{pmatrix}_\theta + \alpha(\theta)\ V_x(\theta)$$

$$\frac{d}{d\theta}\begin{pmatrix} z \\ p_z \end{pmatrix}_\theta = L(\theta) \begin{pmatrix} x \\ p_x \end{pmatrix}_\theta + \beta(\theta)\ V_z(\theta) \qquad (2\text{-}7)$$

$$\frac{dX(\theta)}{d\theta} = m_1\ x(\theta) + m_2\ p_x(\theta) + \gamma(\theta)\ V_x(\theta)\ .$$

where the elements of α, β, and γ are tabulated in table 2-1.

If the equations (2-6) are substituted into the differential equations (2-5), the result will be a differential equation containing terms to second order in the expansion coefficients. Proceeding in this manner, and retaining only terms of second order or less, $V_x(\theta)$ and $V_z(\theta)$ are ,

$$V_x = \begin{bmatrix} X_{11}^2\, x_0^2 + 2\, X_{11}\, X_{12}\, x_0\, p_{x0} + X_{12}^2\, p_{x0}^2 \\ X_{11}\, X_{21}\, x_0^2 + (X_{11}\, X_{22} + X_{12}\, X_{21})\, x_0\, p_{x0} + X_{12}\, X_{22} p_{x0}^2 \\ X_{21}^2\, x_0^2 + 2\, X_{21}\, X_{22}\, x_0\, p_{x0} + X_{22}^2\, p_{x0}^2 \\ Z_{11}^2\, z_0^2 + 2\, Z_{11}\, Z_{12}\, z_o\, p_{z0} + Z_{12}^2\, p_{z0}^2 \\ Z_{11}\, Z_{21}\, z_o^2 + (Z_{11}\, Z_{22} + Z_{12}\, Z_{21})\, z_0\, p_{z0} + Z_{12}\, Z_{22}\, p_{z0}^2 \\ Z_{21}^2\, z_0^2 + 2\, Z_{21}\, Z_{22}\, z_0\, p_{z0} + Z_{22}^2\, p_{z0}^2 \end{bmatrix}$$

and,

$$V_z = \begin{bmatrix} X_{11}Z_{11}x_0z_0 + X_{11}Z_{12}x_0p_{z0} + X_{12}Z_{11}p_{x0}z_0 + X_{12}Z_{12}p_{x0}p_{z0} \\ X_{11}Z_{21}x_0z_0 + X_{11}Z_{22}x_0p_{z0} + X_{12}Z_{21}p_{x0}z_0 + X_{12}Z_{22}p_{x0}p_{z0} \\ X_{21}Z_{11}x_0z_0 + X_{21}Z_{12}x_0p_{z0} + X_{22}Z_{11}p_{x0}z_0 + X_{22}Z_{12}p_{x0}p_{z0} \\ X_{21}Z_{21}x_0z_0 + X_{21}Z_{22}x_0p_{z0} + X_{22}Z_{21}p_{x0}z_0 + X_{22}Z_{22}p_{x0}p_{z0} \end{bmatrix}$$

where the subscript zero implies that the initial values of the coordinate are to be used.

Continuing the substitution and collecting the coefficients of the initial values (x_0, p_{x0} etc.) a differential equation for each first and second order coefficient is obtained. The result shows a systematic pattern,

$$X'_{11} = k_{11}\, X_{11} + k_{12}\, X_{21} \qquad X'_{21} = k_{21}\, X_{11} + k_{22}\, X_{21}$$

$$X'_{12} = k_{11}\, X_{12} + k_{12}\, X_{22} \qquad X'_{22} = k_{21}\, X_{12} + k_{22}\, X_{22}$$

Table 2-1. The elements of the arrays α and β. These arrays contain the coefficients of the displacements (x, p_x etc.) found in the differential equations 2-5.

$$\alpha_{12} = p^2 / p_\theta^3$$

$$\alpha_{13} = 1.5\ r\ p^2\ p_r / p_\theta^5$$

$$\alpha_{16} = .5\ r\ p_r / p_\theta^3$$

$$\alpha_{21} = -\frac{\partial B}{\partial r} - \frac{1}{2}\ r\ \frac{\partial^2 B}{\partial r^2}$$

$$\alpha_{23} = -\ .5\ p^2 / p_\theta^3$$

$$\alpha_{24} = .5\ r\ \left(\frac{\partial^2 B}{\partial r^2} + \frac{1}{r}\ \frac{\partial B}{\partial r} + \frac{1}{r^2}\ \frac{\partial^2 B}{\partial \theta^2}\right)$$

$$\alpha_{25} = \frac{1}{p_\theta}\ \frac{\partial B}{\partial \theta}$$

$$\alpha_{26} = -\ .5 / p_\theta$$

$$\beta_{12} = 1 / p_\theta$$

$$\beta_{14} = r\ p_r / p_\theta^3$$

$$\beta_{21} = \frac{\partial B}{\partial r} + r\ \frac{\partial^2 B}{\partial r^2} - \frac{p_r}{p_\theta}\ \frac{\partial^2 B}{\partial r \partial \theta}$$

$$\beta_{23} = -\ \frac{p^2}{p_\theta^3}\ \frac{\partial B}{\partial \theta}$$

$$\gamma_2 = \gamma\ p_r / p_\theta^3$$

$$\gamma_3 = \frac{1}{2}\ \frac{\gamma\ r}{p_\theta^3}\ \left(1 + 3\ \frac{p_r^2}{p_\theta^2}\right)$$

$$\gamma_6 = \frac{1}{2}\ \frac{\gamma\ r}{p_\theta^3}$$

$$a'_{1n} = k_{11}\, a_{1n} + k_{12}\, a_{2n} + f_{1n}$$

$$a'_{2n} = k_{21}\, a_{1n} + k_{22}\, a_{2n} + f_{2n}$$

where the f's are functions of the first order coefficients and the elements of α. These driving functions are tabulated in Table 2-2. A more compact statement of these results is,

$$\frac{d}{d\theta} X = K(\theta)\ X \qquad \frac{d}{d\theta} Z = L(\theta)\ Z$$

(2-8)

$$\frac{d}{d\theta} A_n = K(\theta)\ A_n + F_n(\theta) \qquad \frac{d}{d\theta} D_n = L(\theta)\ D_n + G_n(\theta)$$

(2-9)

$$F_n(\theta) = \begin{bmatrix} f_{1n}(\theta) \\ f_{2n}(\theta) \end{bmatrix} \qquad G_n(\theta) = \begin{bmatrix} g_{1n}(\theta) \\ g_{2n}(\theta) \end{bmatrix}$$

(2-10)

$$A_n(\theta) = \begin{bmatrix} a_{1n}(\theta) \\ a_{2n}(\theta) \end{bmatrix} \qquad D_n(\theta) = \begin{bmatrix} d_{1n}(\theta) \\ d_{2n}(\theta) \end{bmatrix}$$

$$\frac{d}{d\theta} \gamma_n = m_1\, a_{1n} + m_2\, a_{2n} + h_n \ .$$

The equations in the first row are the differential equations for the first order coefficients, the solutions of which are already known from section 2.2.2 . The differential equations for the second order terms A_n and D_n are very similar in form to the first order equations, except for the presence of a driving term (F_n or G_n). Since

Table 2-2. The driving functions which appear in the differential equations 2-9. The values of the α's and the β's are listed in table 2-2.

$$f_{11} = \alpha_{12} X_{11} X_{21} + \alpha_{13} X_{21}^2$$

$$f_{12} = \alpha_{12} (X_{11} X_{22} + X_{12} X_{21}) + 2 \alpha_{13} X_{21} X_{22}$$

$$f_{13} = \alpha_{12} X_{12} X_{22} + \alpha_{13} X_{22}^2$$

$$f_{14} = \alpha_{16} Z_{21}^2$$

$$f_{15} = 2\alpha_{16} Z_{21} Z_{22}$$

$$f_{16} = \alpha_{16} Z_{22}^2$$

$$f_{21} = \alpha_{21} X_{11}^2 + \alpha_{23} X_{21}^2$$

$$f_{22} = 2 \alpha_{21} X_{11} X_{12} + 2 \alpha_{23} X_{21} X_{22}$$

$$f_{23} = \alpha_{21} X_{12}^2 + \alpha_{23} X_{22}^2$$

$$f_{24} = \alpha_{24} Z_{11}^2 + \alpha_{25} Z_{11} Z_{21} + \alpha_{26} Z_{21}^2$$

$$f_{25} = 2 \alpha_{24} Z_{11} Z_{12} + \alpha_{25} (Z_{11} Z_{22} + Z_{12} Z_{21})$$
$$+ 2 \alpha_{26} Z_{21} Z_{22}$$

$$f_{26} = \alpha_{24} Z_{12}^2 + \alpha_{25} Z_{12} Z_{22} + \alpha_{26} Z_{22}^2$$

$$g_{11} = \beta_{12} X_{11} Z_{21} + \beta_{14} X_{21} Z_{21}$$

$$g_{12} = \beta_{12} X_{11} Z_{22} + \beta_{14} X_{21} Z_{22}$$

$$g_{13} = \beta_{12} X_{12} Z_{21} + \beta_{14} X_{22} Z_{21}$$

Table 2-2 (cont'd).

$$g_{14} = \beta_{12} x_{12} z_{22} + \beta_{14} x_{22} z_{22}$$

$$g_{21} = \beta_{21} x_{11} z_{11} + \beta_{23} x_{21} z_{11}$$

$$g_{22} = \beta_{21} x_{11} z_{12} + \beta_{23} x_{21} z_{12}$$

$$g_{23} = \beta_{21} x_{12} z_{11} + \beta_{23} x_{22} z_{11}$$

$$g_{24} = \beta_{21} x_{12} z_{12} + \beta_{23} x_{22} z_{12}$$

$$h_1 = \gamma_2 x_{11} x_{21} + \gamma_3 x_{21}^2$$

$$h_2 = \gamma_2 (x_{11} x_{22} + x_{12} x_{21}) + 2 \gamma_3 x_{21} x_{22}$$

$$h_3 = \gamma_2 x_{12} x_{22} + \gamma_3 x_{22}^2$$

$$h_4 = \gamma_6 z_{21}^2$$

$$h_5 = 2 \gamma_6 z_{21} z_{22}$$

$$h_6 = \gamma_6 z_{22}^2$$

the driving terms are only functions of the first order expansion coefficients (which are known), the solutions to equations 2-9 can be found using a Green's function.

$$A_n(\theta) = \int_0^{\theta} F_n(\theta')\ \Lambda(\theta, \theta')\ d\theta' \ , \text{ and} \qquad (2\text{-}11)$$

$$B_n(\theta) = \int_0^{\theta} G_n(\theta')\ \Lambda(\theta, \theta')\ d\theta' \ , \qquad (2\text{-}12)$$

where Λ is the Green's function.

The solution for the second order expansion coefficients of the time, τ, are much simpler, since the right hand side of equation 2-10 involves functions of the first order expansion coefficients only. Thus,

$$\gamma_n(\theta) = \int_0^{\theta} (m_1\ a_{1n}(\theta') + m_2\ a_{2n}(\theta') + h_n\ )\ d\theta' \ . \qquad (2\text{-}13)$$

If the Green's function is known then the second order matrix elements can be obtained by numerically integrating equations 2-11 , 2-12 and 2-13 , along the EO at the same time as the first order equations are being computed.

2.2.4 The Green's Function[16]

The problem requires the solution of,

$$\left[I \frac{d}{d\theta} - K(\theta) \right] A_n(\theta) = F_n(\theta) ,$$

where I is the unit matrix and K is either K or L as defined in equation 2-7. The solution, X of the homogenous equation,

$$\left[I \frac{d}{d\theta} - K(\theta) \right] X_n(\theta) = 0 ,$$

is known. The Green's function must be a solution of;

$$\left[I \frac{d}{d\theta} - K(\theta) \right] \Lambda_n(\theta, \theta') = I \, \delta(\theta - \theta') ,$$

subject to the conditions,

$$\Lambda = 0 \quad \theta < \theta'$$

and $\Lambda(\theta = \theta' + \epsilon) = I$.

Since Λ is a solution of the homogenous equation for $\theta > \theta'$ (or $\theta < \theta'$) it must be a linear combination of X. If $Y(\theta')$ is a matrix to be determined, then,

$$\Lambda(\theta > \theta') = X(\theta) \, Y(\theta') .$$

The boundary conditions at $\theta = \theta'$ give,

$$\Lambda(\theta = \theta' + \epsilon) = I = X(\theta') \; Y(\theta')$$

$$\therefore \; Y(\theta') = X^{-1}(\theta')$$

$$\therefore \quad \Lambda(\theta, \theta') = X(\theta) \; X^{-1}(\theta') .$$

$\Delta(\theta) = X_{11}(\theta) \; X_{22}(\theta) - X_{12}(\theta) \; X_{21}(\theta) = 1$ so,

$$X^{-1}(\theta') = \begin{bmatrix} X_{22}(\theta') & -X_{12}(\theta') \\ -X_{21}(\theta') & X_{11}(\theta') \end{bmatrix}$$

2.3 Crossing the Accelerating Gaps[17]

When the equations for the matrix elements are integrated along the equilibrium orbit they start and end on radial lines that pass through the point where the EO crosses the gap. As a result when the displaced rays are transferred up to the gap, the values for the displacements (x, p_x, etc.) are the values along a radial line. In order to compute the effects of the acceleration correctly, the values of r, p_r and τ are needed at the point the displaced orbit crosses the gap. Since the values of the orbit at this point are not known, they must be estimated. Moving the displaced orbit onto the gap first requires the calculation of $\delta\theta$ (see Figure 2-1), which in turn requires the value of δr. The angle of the gap $\theta_g(r)$ is a given function of the form,

$$\theta_g(r) = \theta_0 - \Theta(r) ,$$

which has been input to the program. In our case the gaps have been entered as a table, (GAPTH), of theta values at equal ΔR_g intervals in radius. A double three point Lagrangian interpolation[18] is used to find the first and second derivatives;

$$\frac{d\theta_g}{dr} = \alpha_1 \qquad \frac{d^2\theta_g}{dr^2} = \alpha_2 .$$

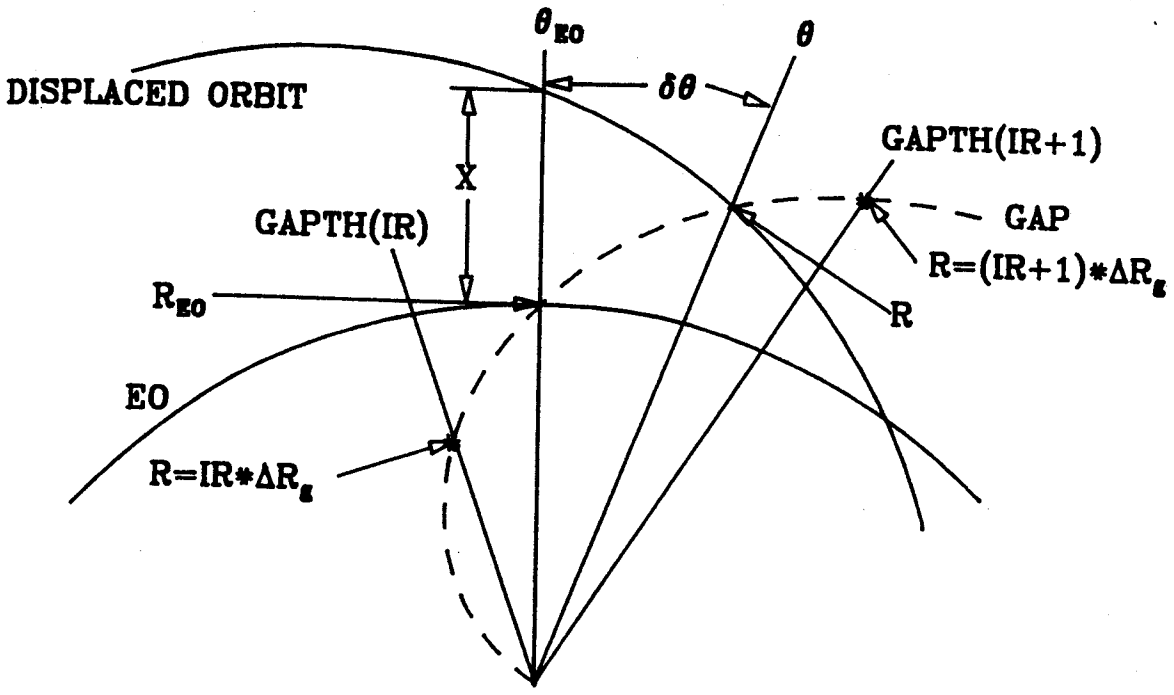

Figure 2-1. The geometry of the gap crossing correction. The gap position is given at points Gapth(ir). $\delta\theta$ is the angle through which the orbit must be moved.

The required $\delta\theta_g$ corresponding to a δr (unknown) can be divided into first and second order components, as can δr, so:

$$\delta\theta_g = \delta\theta_1 + \delta\theta_2 ,$$

$$\delta r = \delta r_1 + \delta r_2 .$$

Using the Taylor expansion for $\delta\theta_g$, and δr,

$$\delta\theta_g = \frac{d\theta_g}{dr}\,\delta r + \frac{1}{2}\,\frac{d^2\theta_g}{dr^2}\,\delta r^2$$

$$= \frac{d\theta_g}{dr}\,(\delta r_1 + \delta r_2) + \frac{1}{2}\,\frac{d^2\theta_g}{dr^2}\,\delta r_1^2 \qquad (2\text{-}13)$$

$$\delta r = x + r'\,\delta\theta + \frac{1}{2}\,r''\,\delta\theta^2$$

$$= x + (r_0' + x')\,\delta\theta_1 + r_0'\,\delta\theta_2 + \frac{1}{2}\,r_0''\,\delta\theta_1^2 .$$

where the zero subscript indicates the EO value. Collecting terms of the same order,

$$\delta r_1 = x + r_0'\,\delta\theta_1$$

$$\delta r_2 = r_0\,\delta\theta_2 + x'\,\delta\theta_1 + \frac{1}{2}\,r_0''\,\delta\theta_1^2 .$$

If these values for δr are then substituted into equation (2-13) and the first order terms collected,

$$\delta\theta_1 = \frac{d\theta_g}{dr}\,(x + r_0'\,\delta\theta_1) .$$

so,

$$\delta\theta_1 = \frac{x\ (d\theta_g / dr)}{1 - r_0'\ (d\theta_g/dr)} .$$

Now that the values of $\delta\theta_1$ and δr_1 have been determined, it remains to find δr_2.

$$\delta r_2 = r_0'\ \delta\theta_2 + x'\ \delta\theta_1 + \frac{1}{2}\ r_0''\ \delta\theta_1^2$$

$$\delta\theta_2 = \frac{d\theta_g}{dr}\ \delta r_2 + \frac{1}{2}\ \frac{d^2\theta_g}{d^2 r}\ \delta r_1^2$$

$$= \frac{d\theta_g}{dr}\ r_0'\ \delta\theta_2 + \frac{d\theta_g}{dr}\ (x'\ \delta\theta_1 + \frac{1}{2}\ r_0''\ \delta\theta_1^2) + \frac{1}{2}\ \frac{d^2\theta_g}{d^2 r}\ \delta r_1^2$$

$$\delta\theta_2 = \frac{(x'\ \delta\theta_1 + \frac{1}{2}\ r_0''\ \delta\theta_1^2)(d\theta_g/dr) + \frac{1}{2}\ \delta r_1^2\ (d^2\theta_g/dr^2)}{1 - r_0'\ (d\theta_g / dr)}$$

So, using the appropriate values for the derivatives gives,

$$\delta\theta_1 = \frac{x\ \alpha_1}{1 - r_0'\ \alpha_1} ,$$

$$\delta\theta_2 = \frac{(x'\ \delta\theta_1 + \frac{1}{2}\ r_0''\ \delta\theta_1^2)\ \alpha_1 + \frac{1}{2}\ \delta r_1^2\ \alpha_2}{1 - r_0'\ \alpha_1} .$$

The procedure for calculating the changes in each of the orbit coordinates introduced by $\delta\theta$ follows the same method used to find δr. If q is any coordinate then,

$$q \rightarrow q + \delta q ,$$

where,

Table 2-3. The derivatives of the orbit coordinates necessary for the calculation of the gap correction. The symbol "q" is any of the particle parameters. The primes are differentiation with respect to θ.

q	q'_o	q'_1	q''_o
r	$r\, p_r / p_\theta$	$\frac{p_r}{p_\theta} x + \frac{r\, p^2}{p_\theta^3} p_x$	$\frac{p_r}{p_\theta} r'_o + \frac{r\, p^2}{p_\theta^3} p'_{ro}$
p_r	$p_\theta - r\, B$	$-\frac{p_r}{p_\theta} p_x - (B + r\frac{\partial B}{\partial r}) x$	$-\frac{p_r}{p_\theta} p'_{ro} - (B + r\frac{\partial B}{\partial r}) r'_o$
z	0	$r\, p_z / p_\theta$	0
p_z	0	$z\,(r \frac{\partial B}{\partial r} - \frac{p_r}{p_\theta} \frac{\partial B}{\partial \theta})$	0
τ	$\gamma\, r / p_\theta$	$\frac{\gamma}{p_\theta} x + \frac{\gamma\, r}{p_\theta^3} p_r\, p_x$	$\frac{\gamma}{p_\theta} r'_o + \frac{\gamma\, r}{p_\theta^3} p_r\, p'_{ro}$

$$\delta q \simeq q' \, \delta\theta + \frac{1}{2} q'' \, \delta\theta^2$$

$$\simeq (q_0' + q_1') \, \delta\theta + \frac{1}{2} q_0'' \, \delta\theta^2 \, .$$

The values of the necessary derivatives are tabulated in Table 2-3. In order to compute all these derivatives the values of $p_\theta - r B$, $B + r \frac{\partial B}{\partial r}$, and $r \frac{\partial B}{\partial r} - \frac{p_r}{p_\theta} \frac{\partial B}{\partial \theta}$ are stored along with the other EO values when the transfer matrices are being computed.

Now that the values of r, p_r and τ are known on the gap the effect of the RF voltage can be computed. The computation of the acceleration process is identical to that used in the numerical integration code "SPRGAPZ", and is described in detail in reference 8. It suffices here to say that both the energy and p_r are modified by this routine.

Before proceeding to perform the transfer up to the next gap, the values of the displacements on a radial line are again required. Since the energy has changed, so has the equilibrium orbit, and thus this is not simply a reversal of the previous process. This time both the azimuth of the EO and of the orbit are known, ie.,

$$\delta\theta = \delta\theta_g - \delta\theta_{EO} \, .$$

This time the difficulty arises because the values of the displacement from the EO, along the radial line, are not known. What is known is,

$$x_g = r_g - r_0 \ ,$$

$$p_x = p_{rg} - p_{r0} \ ,$$

z_g and p_{zg} .

The subscript "g" refers to the values on the gap. In the following, coordinates without a subscript will be understood to be evaluated on the radial line that passes through the point at which the EO crosses the gap. The required corrections δr and δp_r are,

$$\delta r = r_g - r \ ,$$

$$\delta p_r = p_{rg} - p_r \ .$$

As before,

$$\delta r = r_0' \ \delta\theta + x' \ \delta\theta + \frac{1}{2} r_0'' \ \delta\theta^2 \ ,$$

$$\delta p_r = p_{r0}' \ \delta\theta + p_x' \ \delta\theta + \frac{1}{2} p_{r0}'' \ \delta\theta^2 \qquad (2\text{-}14)$$

The displacements on the gap (which are known) are given by,

$$x_g = r_g - r_0 = x + \delta r \ .$$

$$p_{xg} = p_{rg} - p_{r0} = p_x + \delta p_r \ .$$

Putting these values for x and p_x into equations (2-14) gives,

$$\delta r = r'_0\,\delta\theta + \frac{1}{2} r''_0\,\delta\theta^2 + \left(\frac{p_r}{p_\theta} x_g + \frac{r\,p^2}{p_\theta^3} p_{xg}\right)\delta\theta - \frac{p_r}{p_\theta}\delta\theta\,\delta r - \frac{rp^2}{p_\theta^3}\delta\theta\,\delta p_r$$

$$\delta p_r = p'_{r0}\,\delta\theta + \frac{1}{2} p''_{r0}\,\delta\theta^2 + \left[-\frac{p_r}{p_\theta} p_{xg} - \left(B + r\frac{\partial B}{\partial r}\right) x_g\right]\delta\theta + \left[\frac{p_r}{p_\theta}\delta p_r + \left(B + r\frac{\partial B}{\partial r}\right)\delta r\right]\delta\theta .$$

Rearranging these equations and identifying the derivatives of x_g and p_{xg} leads to,

$$\delta r\left(1 + \frac{p_r}{p_\theta}\delta\theta\right) + \left(\frac{r\,p^2}{p_\theta^3}\delta\theta\right)\delta p_r = \Delta r$$

$$-\delta r\left(B + r\frac{\partial B}{\partial r}\right)\delta\theta + \left(1 - \frac{p_r}{p_\theta}\delta\theta\right)\delta p_r = \Delta p_r , \qquad (2\text{-}15)$$

where Δr and Δp_r are the values of δr and δp_r respectively if x_g and p_{xg} are used in place of x and p_x. Equations (2-15) are a set of linear equations in δr and δp_r, the solution to which is given by,

$$\delta r = \left[\Delta r - \left\{\frac{p_r}{p_\theta}\Delta r + \frac{r\,p^2}{p_\theta^3}\Delta p_r\right\}\delta\theta\right] / \text{DET}$$

$$\delta p_r = [\Delta p_r + \{ \frac{p_r}{p_\theta} \Delta p_r + (B + r \frac{\partial B}{\partial r}) \Delta r \} \delta\theta] / DET$$

$$DET = 1 - \frac{p_r^2}{p_\theta^2} \delta\theta^2 + (B + r \frac{\partial B}{\partial r}) \frac{r\, p^2}{p_\theta^3} \delta\theta^2 .$$

It is necessary to retain all the terms so that if the accelerating voltage is zero, moving onto and back off the gap will not result in a change in the values of the coordinates. Calculation of the changes in z and p_z follow the same pattern, so:

$$\delta z = \frac{r}{p_\theta} p_z \delta\theta$$

$$\delta p_z = z (r \frac{\partial B}{\partial r} - \frac{p_r}{p_\theta} \frac{\partial B}{\partial \theta}) \delta\theta$$

$$\delta z = \frac{r}{p_\theta} \delta\theta (p_{zg} - \delta p_z)$$

$$\delta p_z = (r \frac{\partial B}{\partial r} - \frac{p_r}{p_\theta} \frac{\partial B}{\partial \theta}) \delta\theta (z_g - \delta z)$$

$$\delta z + \frac{r}{p_\theta} \delta\theta \delta p_z = \frac{r}{p_\theta} \delta\theta p_{zg} = \Delta z$$

$$(r \frac{\partial B}{\partial r} - \frac{p_r}{p_\theta} \frac{\partial B}{\partial \theta}) \delta\theta \delta z + \delta p_z = (r \frac{\partial B}{\partial r} - \frac{p_r}{p_\theta} \frac{\partial B}{\partial \theta}) \delta\theta z_g = \Delta p_z$$

$$\delta z = [\Delta z - \frac{r}{p_\theta} \delta\theta \Delta p_z] / DETZ$$

$$\delta p_z = [\ \Delta p_z - (r \frac{\partial B}{\partial r} - \frac{p_r}{p_\theta} \frac{\partial B}{\partial \theta})\ \delta\theta\ \delta z\ ]\ /\ DETZ$$

$$DETZ = 1 - \frac{r}{p_\theta} (r \frac{\partial B}{\partial r} - \frac{p_r}{p_\theta} \frac{\partial B}{\partial \theta})\ \delta\theta^2$$

The calculation of $\delta\tau$ is considerably simpler, because there are no coupled equations. The correction to τ is,

$$\delta\tau = \tau_0' \delta\theta + \tau_1' \delta\theta + \tau_0'' \delta\theta^2$$

in which the only unknown value, τ_1' , depends on x and p_x.

$$\tau_1' = \frac{\gamma}{p_\theta} x + \frac{\gamma r}{p_\theta^3} p_r p_x = \frac{\gamma}{p_\theta} (x_g - \delta r) + \frac{\gamma r}{p_\theta^3} p_r (p_{xg} - \delta p_r)$$

$$= \frac{\gamma}{p_\theta} x_g + \frac{\gamma r}{p_\theta^3} p_r p_{xg} - \frac{\gamma \delta r}{p_\theta} - \frac{\gamma r}{p_\theta^3} p_r \delta p_r$$

$$= \tau_{1g} - \frac{\gamma \delta r}{p_\theta} - \frac{\gamma r}{p^3{}_\theta} p_r \delta p_r .$$

So.

$$\delta\tau = \Delta\tau - (\frac{\gamma \delta r}{p_\theta} + \frac{\gamma r}{p_\theta^3} p_r \delta p_r)\ \delta\theta .$$

Once the corrections have been computed the substitution,

$$q \rightarrow q + \delta q ,$$

is made, and everything is set to make the transfer to the next gap.

2.4 Program Algorithms

SOMA is designed to operate as a self-contained unit with the exception of the magnetic field grid which must be produced by a separate program (the grid is the same as that used by SPRGAPZ and CYCLONE). At the beginning of each run the program either computes the transfer matrix elements or reads them in from a binary file produced during a previous run. If the matrices are to be computed then the magnetic field and gap table are read in. Then the program searches for equilibrium orbits using the procedure of Gordon and Welton[19], for a set of specified energies. After each EO is found a search is made for the points at which the EO crosses the gaps, and when found the values of r, p_r and θ at these points are stored. A separate routine is then used to integrate the equations of section 2.2 along the EO from one gap location to the next. The integration technique is again a standard Runge-Kutta[15]. In the input stream it can be specified whether first order elements or both first order and second order elements are to be collected. The input can also specify up to 10 fixed angles at which the transfer matrix coefficients will be stored. Currently the fixed angles must fall on a standard Runge-Kutta step. After this procedure is repeated for all the selected energies, and if

the main probe option is selected, a probe transfer matrix is then computed for each energy. This is done by integrating from gap 6 up to the track location, which has been input as a table of r, θ values. Finally all the transfer matrices are stored on binary .files.

Once SOMA has an appropriate set of transfer matrices, it then reads in the parameters common to all particles. This includes the dee voltage, the locations of slits and probes, and the set of transfer equations required. In fact several options exist for the transfer as shown in Table 2-4. Care should be taken when choosing options other than 1 and 6, since these two are the only cases in which a complete expansion to a given order is done. That is to say that case

Table 2-4. --The order of the various parts of the transfer as a function of the input parameter N.

N	x	z
1	first	first
2	2^{nd} in x_0, 1^{st} in z_0	first
3	1^{st} in x_0 and z_0	second
4	2^{nd} in x_0, 1^{st} in z_0	second
5	2^{nd} in x_0 and z_0	first
6	2^{nd} in x_0 and z_0	second

one is the first order solution, case 6 is the second order solution, and all the others are a mixture of the two. For example, if N=4 then the program uses exact median plane equations of motion, allows x to couple into z, but does not couple z into x. Cases 2 through 5 are useful for determining what terms are responsible for a given effect.

The next step is computing the starting conditions for all the particles (up to 5,000 may be run) and storing them. The various possible sets of starting conditions are discussed in section 2.5 . Particles are then run one at a time, each being run until it reaches a turn limit, an energy limit, or a radius limit, whichever comes first.

At each gap a test is performed to determine if any requested fixed angles fall between the current gap and the next gap. If a fixed angle is found then the particle parameters $(x, p_x, z, p_z, \tau, r, p_r)$ are computed for that angle and stored. The fashion in which the parameters are stored depends on what the fixed angle has been designated to represent. After all the fixed angles found have been computed, the program proceeds to compute the transfer to the next gap. At the gap, the parameters $(E, x, p_x, z, p_z, \tau)$ are updated as described in section 2.3, and the process repeats itself as often as necessary. It should be noted that the

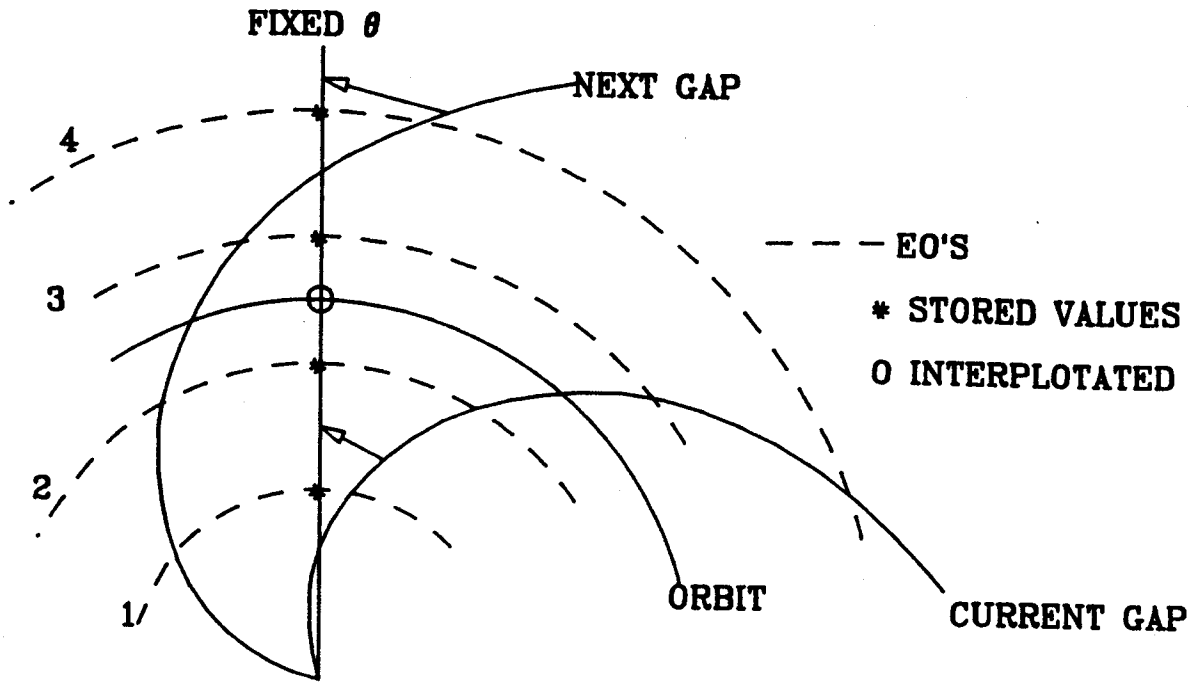

Figure 2-2. The result of a fixed angle crossing a gap. The transfer matrices of the orbits labeled 1, 2, and 3 are correct for a transfer from the current gap to the fixed angle, while that for orbit 4 is not. In this case the orbit being calculated would use the values stored for 1, 2, 3, and 4 when the interpolation is being done, and would give an incorrect result.

computations for the fixed angles in no way affect the values at the gap.

There is a difficulty that occurs in the region where the fixed angle crosses the accelerating gap. The problem arises because the values of the matrix elements are found by interpolating between values that are stored for fixed energies. In Figure 2-2 one possible scenario is illustrated. In this case the transfer matrices stored for orbits 1, 2, and 3 correspond to transfers from the current gap to the desired fixed angle, but the one stored for orbit 4 is a transfer from the next gap to the fixed angle (see arrows). If, as in this case, the interpolation for the matrix elements on the orbit use the values for orbit 4 and orbit 3 then the results will be incorrect. It should be noted that there are currently no structures in the K500 cyclotron that cross the accelerating gaps. Nevertheless the program prints an error message when a transfer of this type happens.

The fixed angles can be designated as one of two things, either a flag or a probe. The flags themselves are divided into two groups, intercepting and non-intercepting. At a flag if the particle lies between the minimum and maximum values for that flag, the orbit parameters are stored. If the flag is intercepting then the particle is considered

removed from the beam, and the next particle is begun, otherwise the run continues unchanged. After all the particles have been run the program will produce scatter plots of any pairs of the orbit coordinates, at any of the possible 20 flag locations. A slit can be described as 2 intercepting flags located at the same azimuth. For detailed ray tracing the particle parameters at all gaps and azimuths (or some combination thereof) can be printed out.

A probe consists of a differential and a main jaw, which can have up to 3 axial divisions or 60 phase divisions. The probe is considered to move outward in radial steps. Upon finding the orbit parameters at the probe azimuth the program determines in which steps the particle would give a current reading. The requirements for this determination are that the probe location does not intercept an earlier turn of the same particle, but does intercept the the current turn. For each bin that these requirements are met the bin count is augmented by 1. There are 20,000 bins available to be divided between the z (or ø) bins and the radial bins. At the end of the run the probe bin values are written in a binary file which can then be used as input to a plotting routine.

2.5 Starting Conditions

A transfer matrix program is used to run large groups of particles, so the generation of starting conditions is of great importance. As a result the program offers a variety of methods, each with its own particular use. The input routine has the ability to calculate the horizontal and vertical eigen-ellipses, the accelerated equilibrium orbit (AEO), and the average central phase, all at a given energy known as the central energy. Any combinations of these values can be used by the various routines used to generate the starting conditions, or the values of these parameters can be set in the input stream.

The simplest routine reads in the values E (energy), x, p_x, z, and p_z on gap 1 for each particle. A similar but more complicated routine reads in the values of E, r, p_r, z, and p_z on gap 1. These two crude techniques are oriented towards cases in which either specific orbits are being tracked, or the initial conditions are being determined by another program. The first technique can also be used to re-start a previous run from the stored final conditions.

The next group of routines are those designed to generate the starting conditions for a group of particles which fill ellipses. The ellipses can be either eigen-ellipses or be

input as a major axis, minor axis and a tilt. The center of the x, p_x ellipse can be displaced from the equilibrium orbit by either an amount determined to be the offset of the AEO or by an amount given in the input stream. In all these cases a specified interval of phase is divided into equal steps, and each starting phase is given an ellipse to be filled using one of the techniques discussed below.

In chapter 5 a special input routine is used. In this case it was desired to run a set of particles which matched the conditions at the exit of the central region. In Figure 2-3 the energy and the displacements x and p_x for a group of particles which were run outwards from the spiral inflector for seven turns with the program CYCLONE are shown. Each of the rays run would in effect be a central ray for a given phase. In each frame the solid line is a function of the form noted in that frame. It can be seen that with appropriate choice of the slope, the linear approximation for x and p_x is quite good. When using this special routine, instead of keeping the displacements in x and p_x for the center of the $x\text{-}p_x$ ellipse, and the starting energy, the same for all starting phases, the coefficients of these functions can be input to SOMA and it will use them to

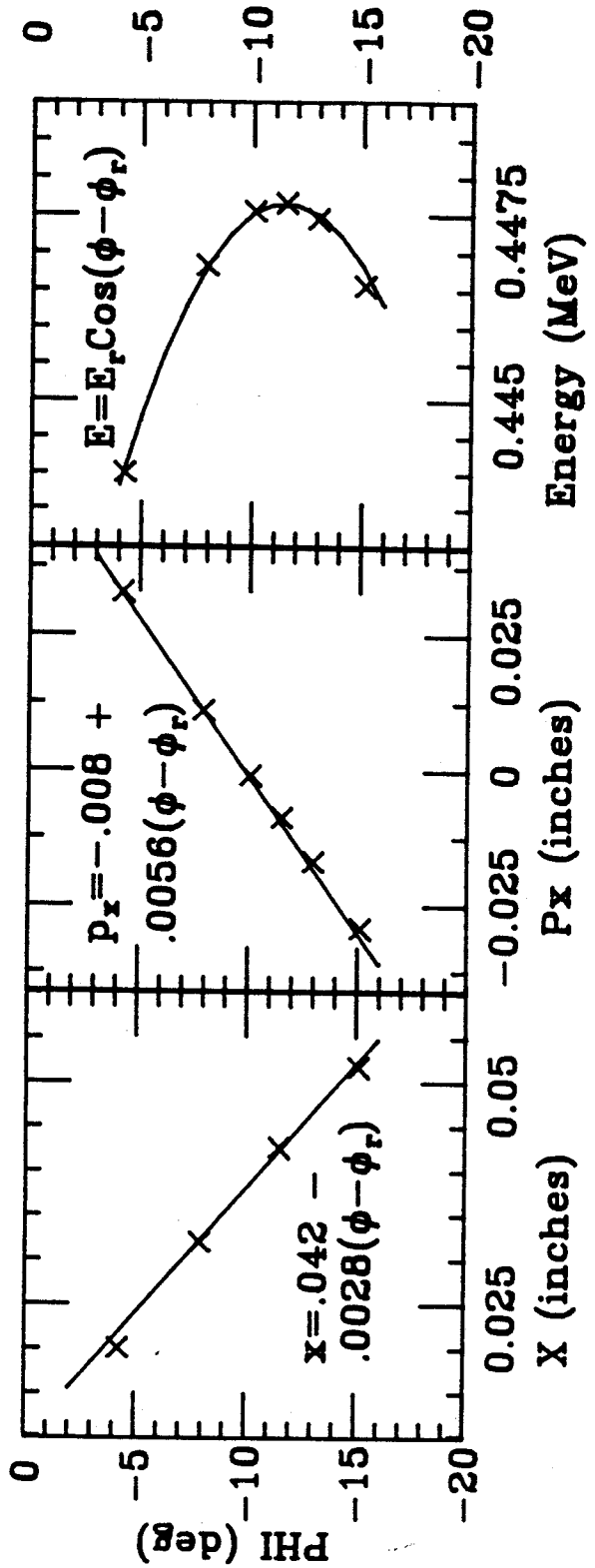

Figure 2-3. Starting conditions at the exit of the central region. The solid lines are the values the program would use for the centre of the ellipse. The crosses are the values obtained when orbits are numerically integrated from the spiral inflector to turn 7 using the code CYCLONE.

calculate the ellipse center and the initial energy for each starting phase.

In the other ellipse-type routines the starting energy can be randomly distributed about the central energy if desired. In all of these cases the ellipse can either be uniformly populated, or randomly populated. The most convenient choice is to populate the ellipse being studied uniformly, and to populate randomly the other ellipse, (eq. uniformly populate the $x\text{-}p_x$ ellipse and randomly populate the $z\text{-}p_z$ ellipse), to get an idea of the spread caused by the coupling. Uniformly populating both ellipses implies a large number of particles. The random population is produced using a standard random number generator to select x and p_x values between 0 and the ellipse maximum. Then the program checks to see if the coordinates fall within the ellipse proper, and if not it selects new values for x and p_x, until they do. The uniform population is done by assigning a square of fixed area to a point which is located at the center of the square. Points are placed in phase space until no more squares will fit into the ellipse.

2.6 Comparison of SOMA with SPRGAPZ

In this section the results of median plane calculations with the program SOMA will be compared with the results obtained with the orbit integration code SPRGAPZ. The tests discussed are only a sample of the many checks preformed. The program SPRGAPZ integrates the exact median plane equations of motion, and the linearized z motion equations. This allows the coupling of the x motion into the z motion, but not the z motion into the x motion. In the following section comparison of the z motion will be done with the program SPRGAPZ4 which uses equations for the vertical motion that are valid to fourth order in z. There are three areas from which one expects to generate differences between SOMA and SPRGAPZ. The most obvious source is the transfer matrices themselves. As the transfer matrix technique is an approximation of a given order there will be contributions from the higher order terms. In this case it is expected that the error would be proportional to the next term in the Taylor expansion. In Figure 2-4 the differences after one turn (without acceleration) are shown. As in all the figures involving comparisions of orbits between SPRGAPZ and SOMA the differences are plotted against a measure of the initial displacment from the EO. In each a set of rays lying on the boundry of an eigen-ellipse was run. and the maximum

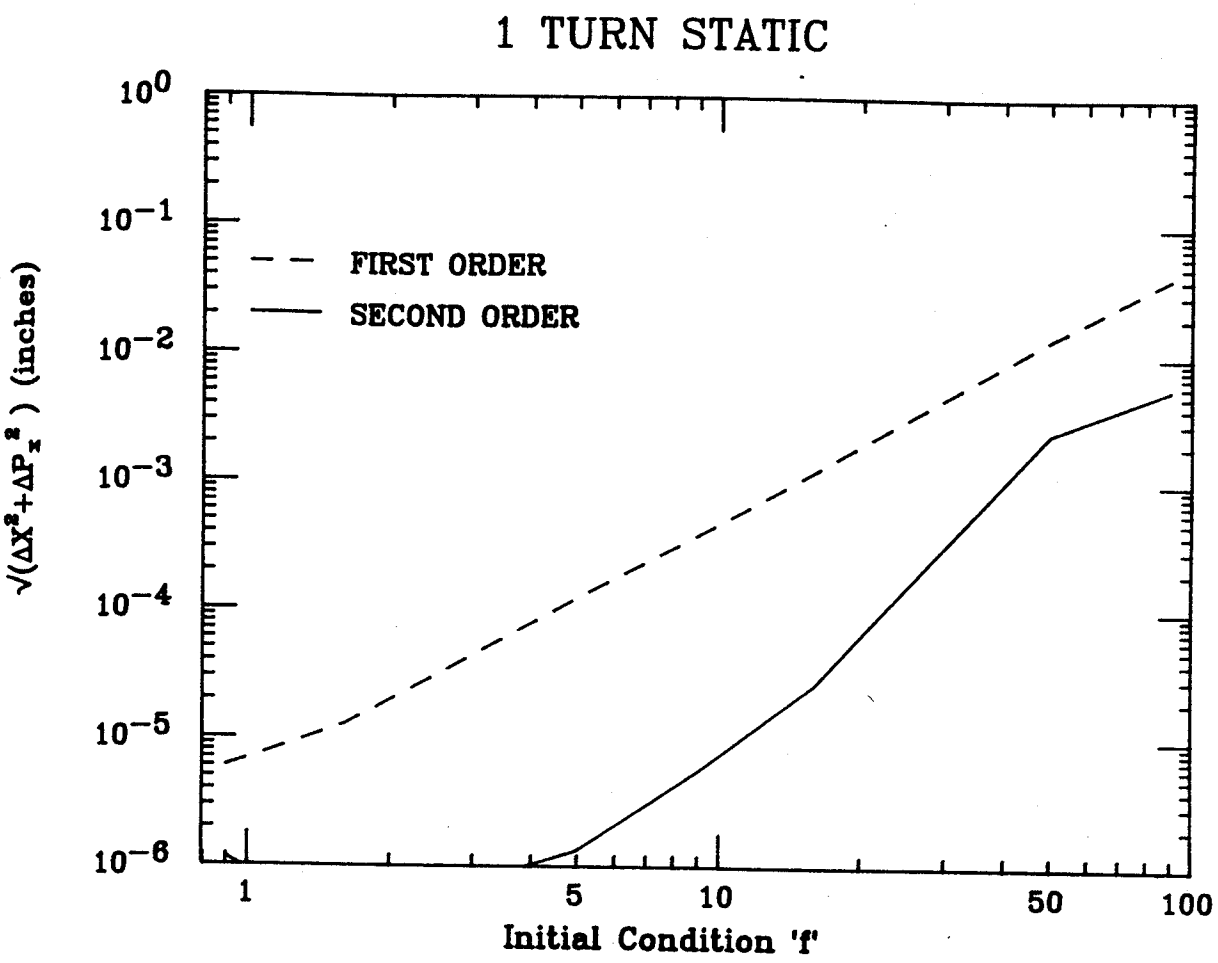

Figure 2-4. Differences between SOMA and SPRGAPZ as a function of the initial displacements from the EO. Each ray was run one turn without acceleration. The initial conditions of each ray are such that it falls on the boundry of an eigen-ellipse of area $(0.2)\,f^2$ mm-mrad. The stability region ends around f=150.

difference for each ellipse was plotted. The area of the eigen-ellipse was $0.2f^2$ mm-mrad. If the expansion is done to first order the error function goes as $(5.6E-6)f^2$. At this radius, (16"), an emittance of 5 mm-mrad corresponds to a maximum orbit center displacement of 0.03". If the expansion is taken to second order the the error is proportional to $(1.6E-8)f^3$, in other words the errors are third order in x. In the first order case the results are exactly the same as that found if the first order equations of motion are integrated numerically. Note that this is not true for the second order case where the solution is to second order in the exact first order solution, not an exact solution of the non-linear differential equation.

There is also a difference generated by the interpolation of the matrix elements when the orbit's energy lies between the stored values. In Figure 2-5 the differences between SPRGAPZ and SOMA are plotted for different interpolation step sizes. For each step size a ray was run whose energy was exactly halfway between two stored values, (the worst possible case). The initial condition of the ray was a displacement of 0.003", and the results are plotted after one turn without acceleration. At this energy (11 MeV) a step size of .2 MeV results in differences of less than a

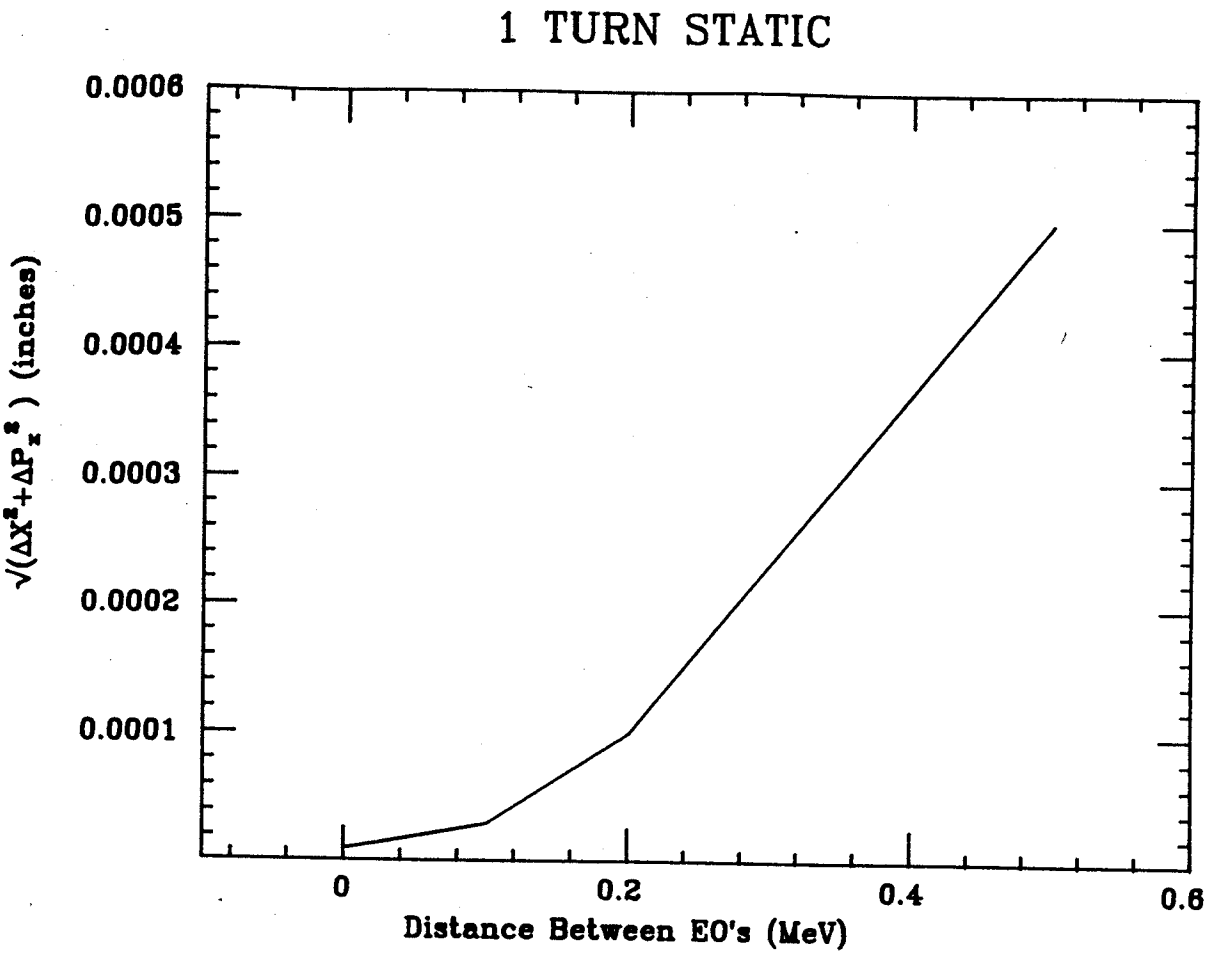

Figure 2-5. The differences between SOMA and SPRGAPZ when the spacing between stored values is changed. The initial displacement was ±0.03". and run for one turn without acceleration.

tenth of a mil. Larger step sizes lead to much larger errors.

The third source of differences is the gap crossing routine. These are the hardest to measure as they only occur when the accelerating voltage is on, so both of the other two effects will be present at the same time. The situation is also confused by an uncertainty in the location at which the orbit crosses the gap. Since the final orbit is not sensitive to small variations in the gap position this uncertainty is only a problem when looking at specific values on a gap. In Figure 2-6 the differences after 100 turns with acceleration are shown as a function of the initial displacement from the EO. These differences are the sum of all three sources of error. As can been seen in the figure the differences for first and second order do not have different slopes as they did in Figure 2-4. This is mostly caused by the fact that accelerated orbits are always displaced from the EO, so even the F=0 ray has a displacment of at least 0.02" from the EO at many points. There are also errors caused by the gap crossing routine, which are seperate from those caused by the expansion technique. A comparison of a first order transfer with first order gap crossings, and a first order transfer with second order gap crossings is also shown in Figure 2-6 . This illustrates

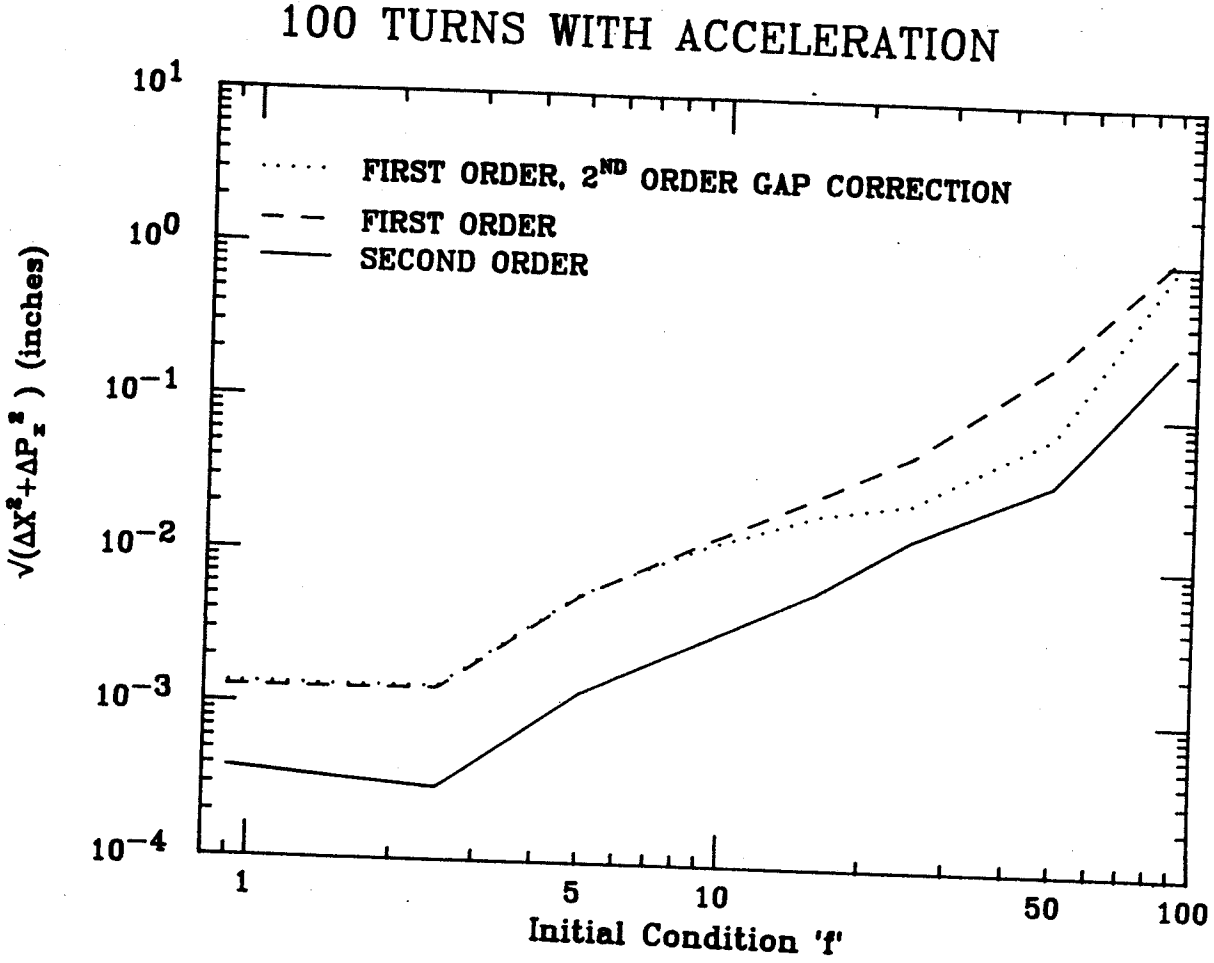

Figure 2-6. The difference in r (and p_r) between SOMA and SPRGAPZ for rays which have been run for 100 turns with acceleration.

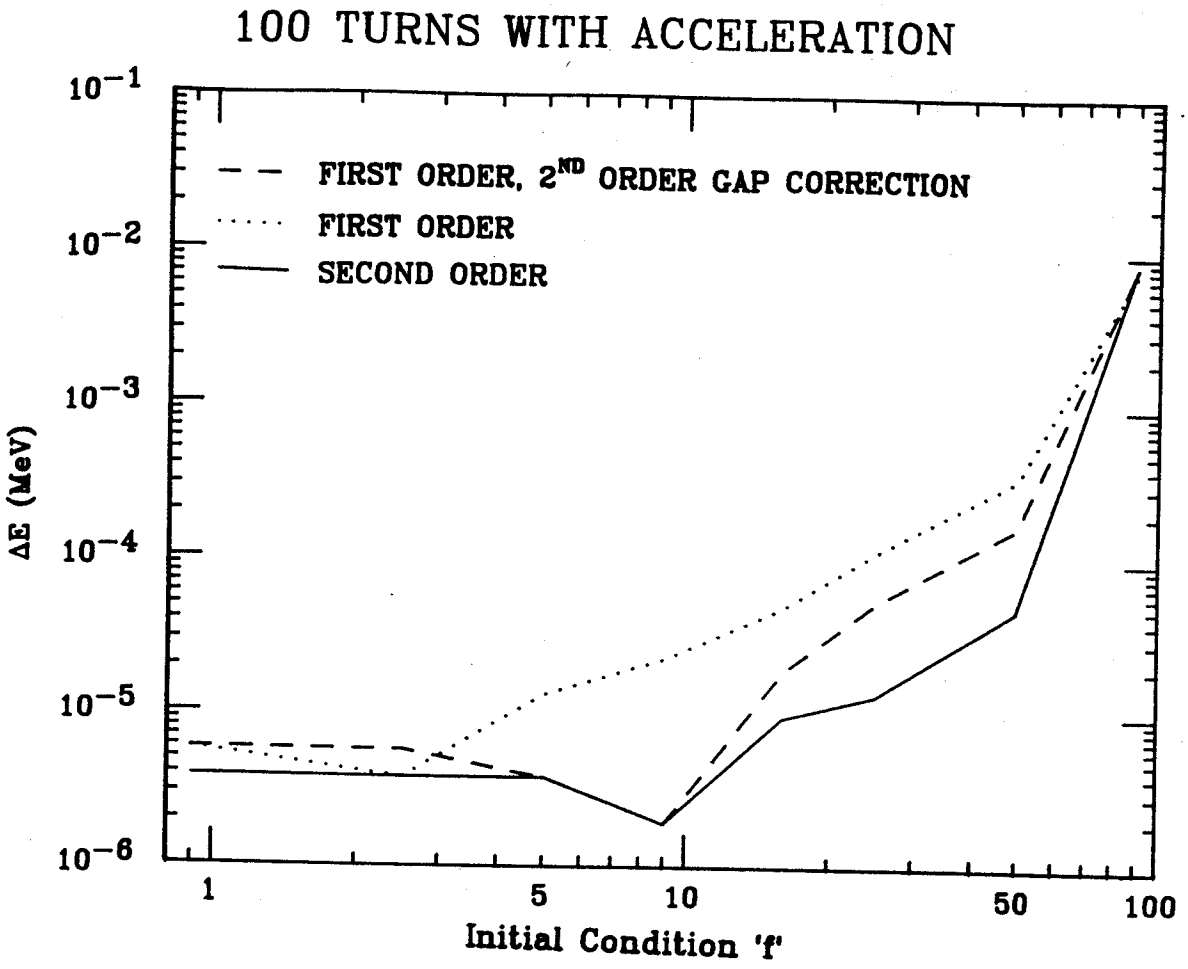

Figure 2-7. The difference in energy for rays for the same rays shown in Figure 2-6.

that the orbits are relatively insensitive to the gap position. Those differences that do occur, arise because of differences in the energy gain as shown in Figure 2-7. In this figure the the difference in energy is plotted for the same rays as shown in Figure 2-6. For the rays of small initial emittances the error is 5 parts in 10^7, which is the same magnitude as the round-off error. The difference in x for a ray which is initially 30 mils from the EO (ϵ=5mm-mrad) after 100 turns, is only 1 mil in x and p_x combined. certainly adequately small unless ray tracing is being done.

2.7 Treatment of Harmonic Field Bumps[20]

As shown by M.M. Gordon[35] the perterbations of the radial oscillations due to asymetric accelerating kicks, can be duplicated using an equivalent field bump. It is therefore reasonable to assume that the effects of the field bump can be represented by making appropriate changes in p_r (and p_z) at each of the 6 accelerating gap locations. That is to say the field bump is to be represented by a series of delta functions, such that,

$$b(r,\theta) = \sum u_k(r)\ \delta(\theta-\theta_k(r)), \qquad k=1,2,\ldots,6.$$

The values of the $u_k(r)$ can be chosen to give the appropriate first and second harmonic bumps, while suppressing all 3N components.

Using equations 2-4 we find that the appropriate momentum kicks must be such that,

$$\Sigma\ \delta p_r(k) = -r\ b$$

$$\Sigma\ \delta p_z(k) = z\left[\ r\ \frac{\partial b}{\partial r} - \frac{p_r}{p_\theta}\ \frac{\partial b}{\partial \theta}\ \right]$$

$$b = g_1 \sin(\theta) + h_1 \cos(\theta) + g_2 \sin(2\theta) + h_2 \cos(2\theta),$$

where g_1, h_1, g_2 and h_2 are the measured bump components at this r. We therefore define u_k, v_k, and w_k such that at gap k the impulses are;

$$\delta p_r(k) = -r\ u_k\ , \text{ and } \delta p_z(k) = z\ r\ v_k + z\frac{p_r}{p_\theta}\ w_k\ ,$$

so;

$$\sum_k u_k \delta(\theta - \theta_k) = g_1 \sin(\theta) + h_1 \cos(\theta) + g_2 \sin(2\theta) + h_2 \cos(2\theta)$$

$$\sum_k v_k \delta(\theta - \theta_k) = \frac{dg}{dr}_1 \sin(\theta) + \frac{dh}{dr}_1 \cos(\theta) + \frac{dg}{dr}_2 \sin(2\theta) + \frac{dh}{dr}_2 \cos(2\theta)$$

$$\sum_k w_k \delta(\theta - \theta_k) = h_1 \sin(\theta) - g_1 \cos(\theta) + 2h_2 \sin(2\theta) - 2g_2 \cos(2\theta)$$

Using orthoganality these three equations give us four linear equations for each of u, v, and w. The 3N harmonics can be surpressed by requiring that the sum of the even k

terms and the sum of the odd k terms are zero, and thus there are six equations for six unknowns. In matrix notation the linear system to be solved is,

$$\begin{bmatrix} \sin(\theta_1) & \sin(\theta_2) & \cdots\cdots & \sin(\theta_6) \\ \cos(\theta_1) & \cos(\theta_2) & \cdots\cdots & \cos(\theta_6) \\ \sin(2\theta_1) & \sin(2\theta_2) & \cdots\cdots & \sin(2\theta_6) \\ \cos(2\theta_1) & \cos(2\theta_2) & \cdots\cdots & \cos(2\theta_6) \\ 1 & 0 & 1\ 0\ 1 & 0 \\ 0 & 1 & 0\ 1\ 0 & 1 \end{bmatrix} \begin{bmatrix} u_1 & v_1 & w_1 \\ u_2 & v_2 & w_2 \\ u_3 & v_3 & w_3 \\ u_4 & v_4 & w_4 \\ u_5 & v_5 & w_5 \\ u_6 & v_6 & w_6 \end{bmatrix} = \pi \begin{bmatrix} g_1 & dg_1/dr & h_1 \\ h_1 & dh_1/dr & -g_1 \\ g_2 & dg_2/dr & 2h_2 \\ h_2 & dh_2/dr & -2g_2 \\ 0 & 0 & 0 \\ 0 & 0 & 0 \end{bmatrix}$$

SOMA uses the IMSL, (International Mathematical and Statistical Libararies INC), subroutine LEQIF to solve this system of equations at each radius value at which a bump profile has been given. The values of u_k, v_k and w_k are stored in a table at the beginning of the run. Each time an orbit crosses a gap, (k), the program interpolates in the table to find the values for u_k, v_k, w_k at the orbit radius, and then computes the impulses,

$$\delta p_r = -r\ u_k,$$

$$\delta p_z = z(r\ v_k + \frac{p_r}{p_\theta}\ w_k).$$

Figure 2-8 shows a typical example of an orbit calculated with SPRGAPZ and SOMA. In this case the orbit begins on the

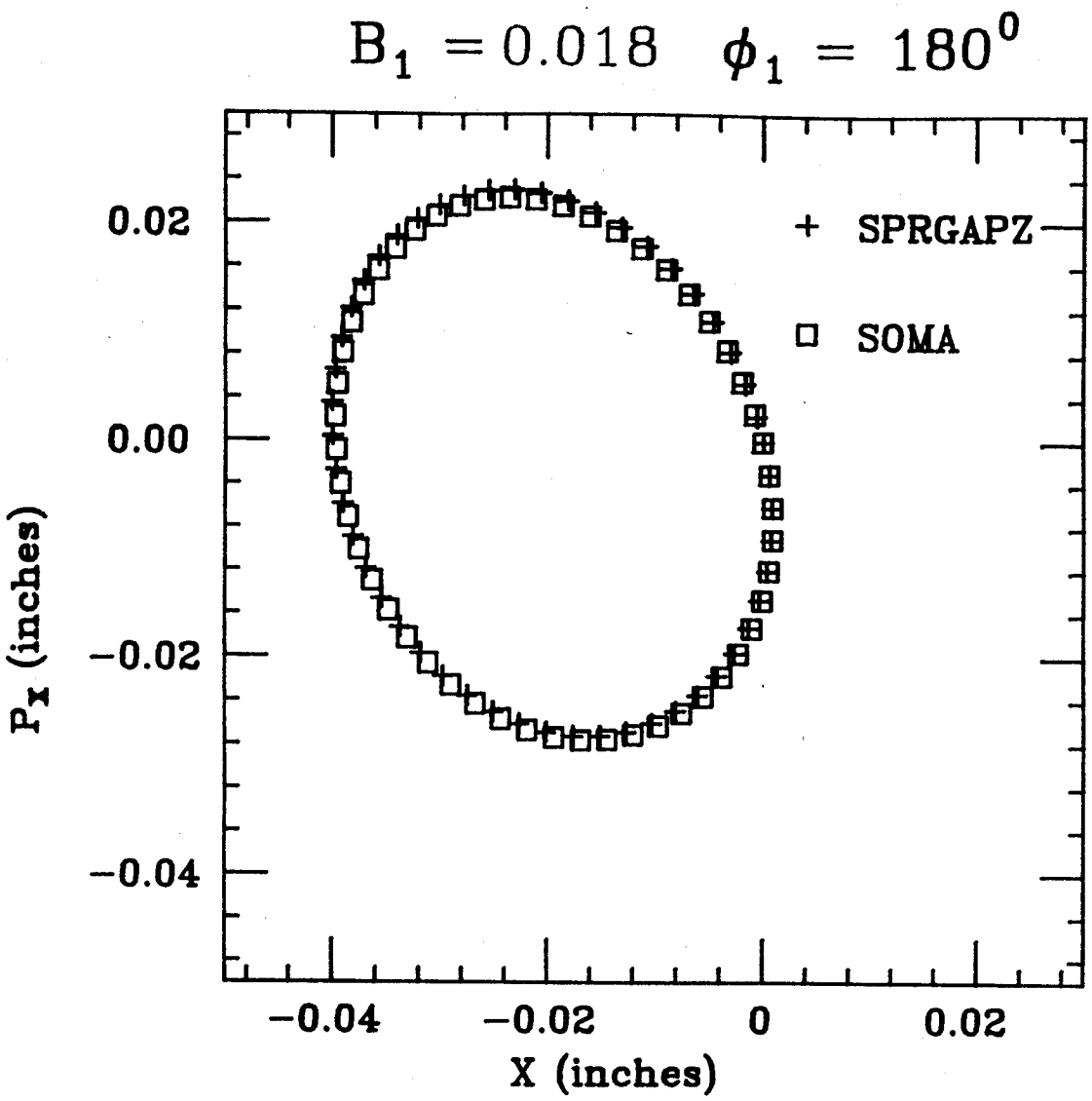

Figure 2-8. A sample precession cycle as calculated by SPRGAPZ and SOMA for a field with a first harmonic. The orbit began on the EO.

EO for E=4 MeV and then the bump causes it to precess. When run with a wide varity of initial conditions, and different bump magnitudes the results were always qualitatively the same as those shown in Figure 2-8.

2.8 Vertical Motion

In order to observe the non-linear z-motion offered by SOMA a simple comparision case was run. A set of 64 rays was formed from all the possible combinations of eight rays located on the perimeter of the vertical eigen-ellipse with emmitance of 75 mm-mrad, and eight rays located on the perimeter of a 35 mm-mrad eigen-ellipse in the horizontal plane. The magnetic field was the same $^{12}C^{4+}$ 30 MeV/u field used before, so the emittances correspond to a final emittance at extraction (30 MeV/u) of ϵ_z = 30 mm-mrad and ϵ_x = 14 mm-mrad. The same rays were also run with the code SPRGAPZ4[36] which correctly treats the magnetic field to fourth order in z (ie. the equations of motion have terms of fourth order in z). All particles were run for 300 turns (field geometry was for a 500 turn total), so most of the acceleration region is covered.

In Figure 2-9 are shown the results from both the SOMA and SPRGAPZ4 runs. In both cases the points all lie very

near the eigen-ellipse, and the spread due to the different $x\text{-}p_x$ values is approximately $\pm 0.02''$ on an ellipse with a half major axis of $0.2''$. The fact that this spreading is very similar in both cases indicates that the contribution of the z^3 term in SPRGAPZ4 is very small, since it is not included in SOMA. There is however a small difference in the amount of rotation around the ellipse boundry in the two cases which leads to a possible combined z, p_z error of $0.026''$. This is probably again caused by the poor EO closure on the spiral gaps. If SOMA is run without the x motion coupling into the z, (N=5 in Table 2-4), then the 8 points in each group become one as would be expected.

3.0 A Computational Examination of Phase Selection in the K500 Cyclotron

3.1 Introduction

Phase Selection is generally used in cyclotrons when it is desired to achieve single turn extraction and its associated benefits[21]. Although we may wish to take advantage of single turn extraction eventually, our initial goal is to achieve separated turns over most of the acceleration region so that detailed accelerator studies can be carried out. As shown in Figure 3-1, the high magnetic field in the K500 cyclotron leads to a turn separation which is rather small compared to the turn width associated with the phase spread. If one also includes the spatial extent of the beam (the x, p_x size) then it is apparent that with the $\pm 15^0$ phase width transmitted by the central region, distinct turns would be observable only for the first few inches. If on the other hand the phase width were reduced to $\pm 2^0$, separated turns would be observable for all of the acceleration process and beam centering could be determined. Centering is of great practical importance

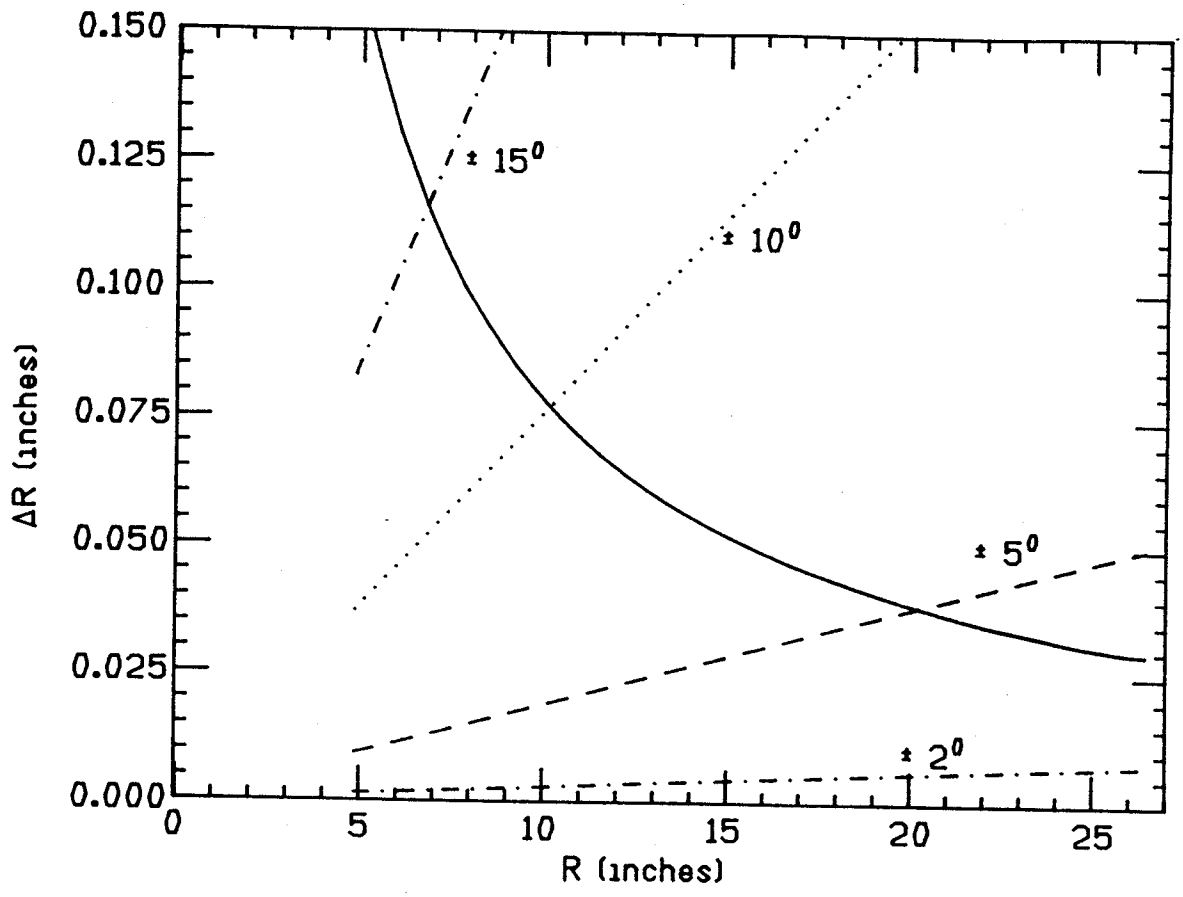

Figure 3-1. Plots of simple estimates of the turn separation and turn widths associated with different phase widths. The turn separation (solid curve) is estimated using $\Delta R=\Delta E^{*}R/2^{*}E$ while the full width of a turn with a given $\Delta\phi$ is found using $\Delta R=(\Delta\phi)^{2}{}^{*}R/4$.

because it reduces phase oscillations, minimizes the effects of non-linearities and makes extraction much less sensitive to the dee voltage[22]. Separated turns also allow the measurement of the radial focusing frequency ν_r, and, with an induced coherent oscillation, the axial frequency ν_z.

Phase selection in cyclotrons is performed by taking advantage of the coupling between the radial (r, p_r) and longitudinal (E-ø) motions of the particles[23]. Figure 3-2 gives a typical plot of radius versus starting time. Note the horseshoe shape, with the peak occurring at the starting time corresponding to the largest average energy gain per turn up to that point. The shape of this curve is a direct consequence of the cos(ø) dependence, (where ø is the average phase), of the energy gain. In the case of an axially injected beam it is possible to populate all the starting phases that will clear the posts in the central region. When running with an internal ion source this is not necessarily true as the source to puller voltage is used to pull ions from the source and thus the density of ions will be dependant on the starting time. With the flexibility offered by an axial injection system it is possible to design the

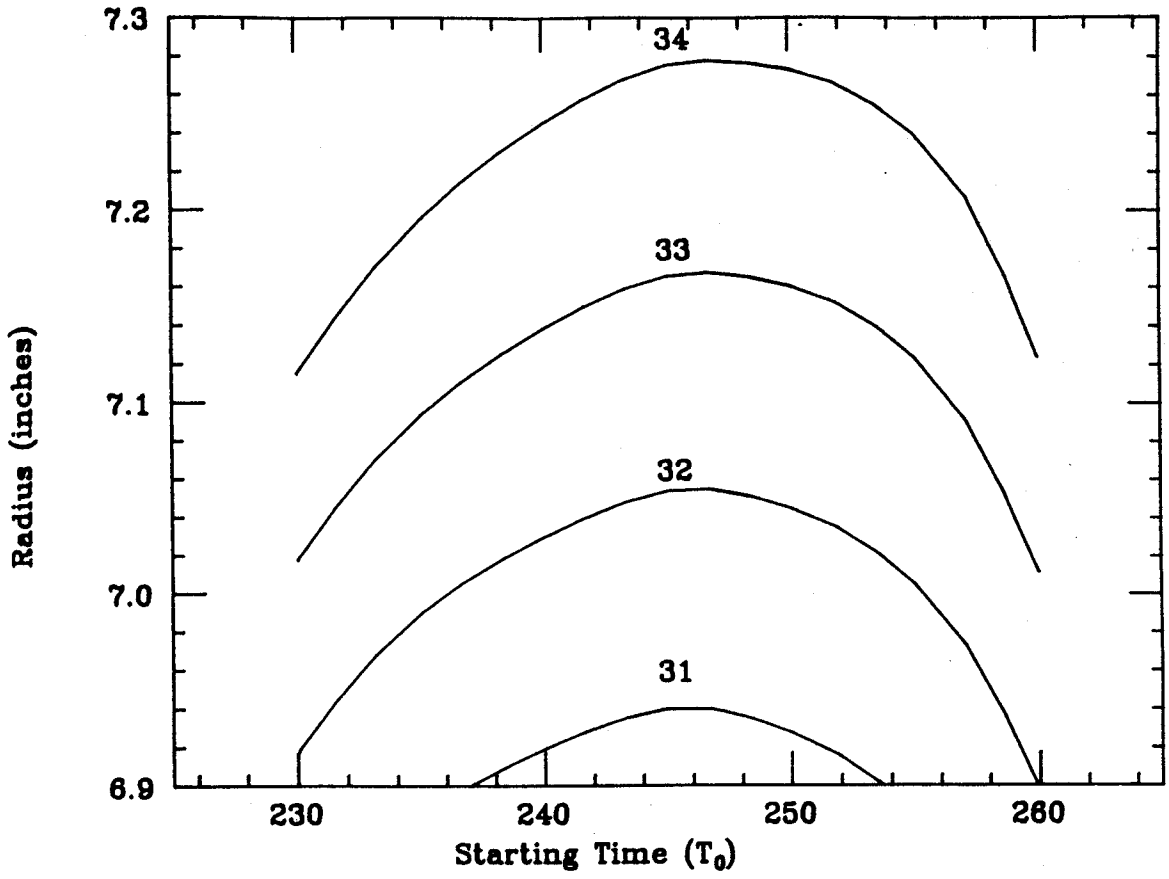

Figure 3-2 The radius of the central ray, shown as a function of starting time, for four successive turns. Note the typical horse-shoe shape resulting from the cos(ø) dependence of the energy gain.

central region to allow only the desired portions of the curves in Figure 3-2 to survive the first turn.

At the center of the horseshoes in Figure 3-2 there is no radial dispersion with phase. On the other hand, on either the leading or trailing edges, the radius is strongly dependent on the phase. As we wish to separate particles with different phases on the basis of the radius differences this feature will be very much needed. (In section 3-4 there will be a discussion of how the slope of the curves can be modified). Given that we require a one-to-one correspondence between radius and phase, it will be necessary to insure that only one side of the horseshoe is populated. When the beam is axially injected into the K500 the particles with a starting time of $\tau_0=250^0$ have the largest energy gain per turn in the middle of the cyclotron, ie. by the time they reach 15" they are at the center of the horseshoe. Also the particles with $\tau_0=260^0$ have the least centering error at 15", so it would be advantageous to populate the starting phases between 250^0 and 260^0. The process of selecting which starting times are populated will be referred to as "coarse selection", since it will limit the phase width in the machine to $\pm 10^0$, while the more careful selection at 7" will be referred to as "fine selection".

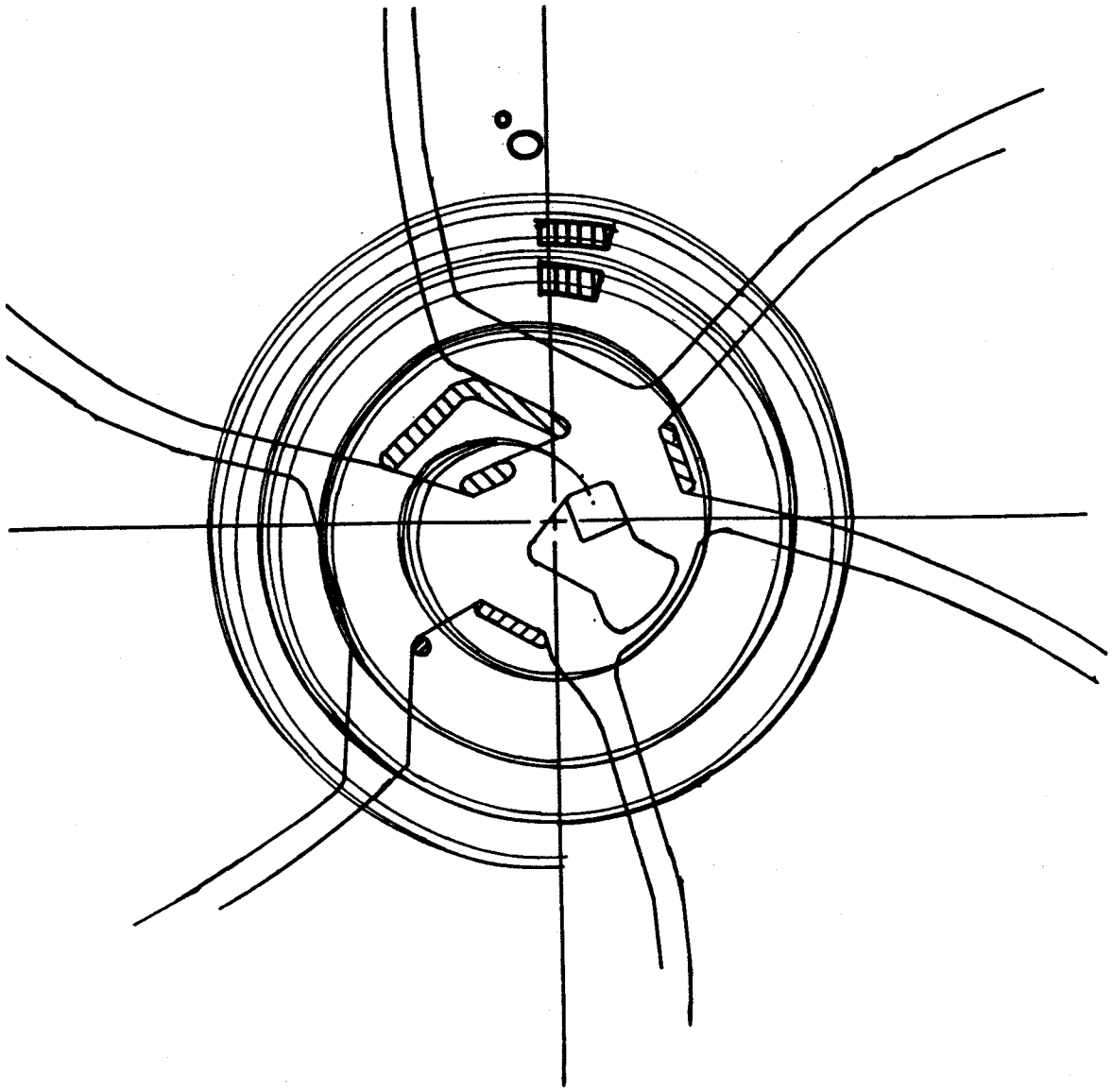

Figure 3-3. Electrode structure for the K500 first harmonic central region using a PIG source. Four orbits are shown corresponding to starting times (from outermost at $\theta=0^0$ to innermost), τ_0=230. 240. 250. and 260 degrees. The peak electric field between the source and puller is achieved at τ_0=270. A slit is located on the 0^0 hill extension of the center plug allowing easy installation and removal. This slit removes all particles whose starting times do not fall between 230 and 250 degrees.

3.2 Coarse Selection

The first stage of the phase selection process is a coarse selection made near the center of the machine where the large turn separation allows the installation of a slit with a large enough frame to avoid the possibility of undesired phases passing outside the frame. If such a system were designed to transmit only 20^0 of phase the situation illustrated in Figure 3-2 would be single valued. In Figure 3-3 such an aperture is shown for the first harmonic central region using a Penning Ion source. In this figure we have superimposed 4 orbits on a median plane section of the central region electrode structure. The four rays have starting times, τ_0, of $230^0, 240^0, 250^0$, and 260^0 and an initial $x=p_x=0$. As shown, only the 240^0 and 250^0 rays pass through the slot formed by a U shaped block mounted on the hill portion of the center plug, (230^0 almost does). (By locating the slit on the center plug it can be removed and inserted by pulling the center plug, a considerably easier task than raising the magnet cap.) Since a τ_0 of 270^0 corresponds to the peak electric field in the source-to-

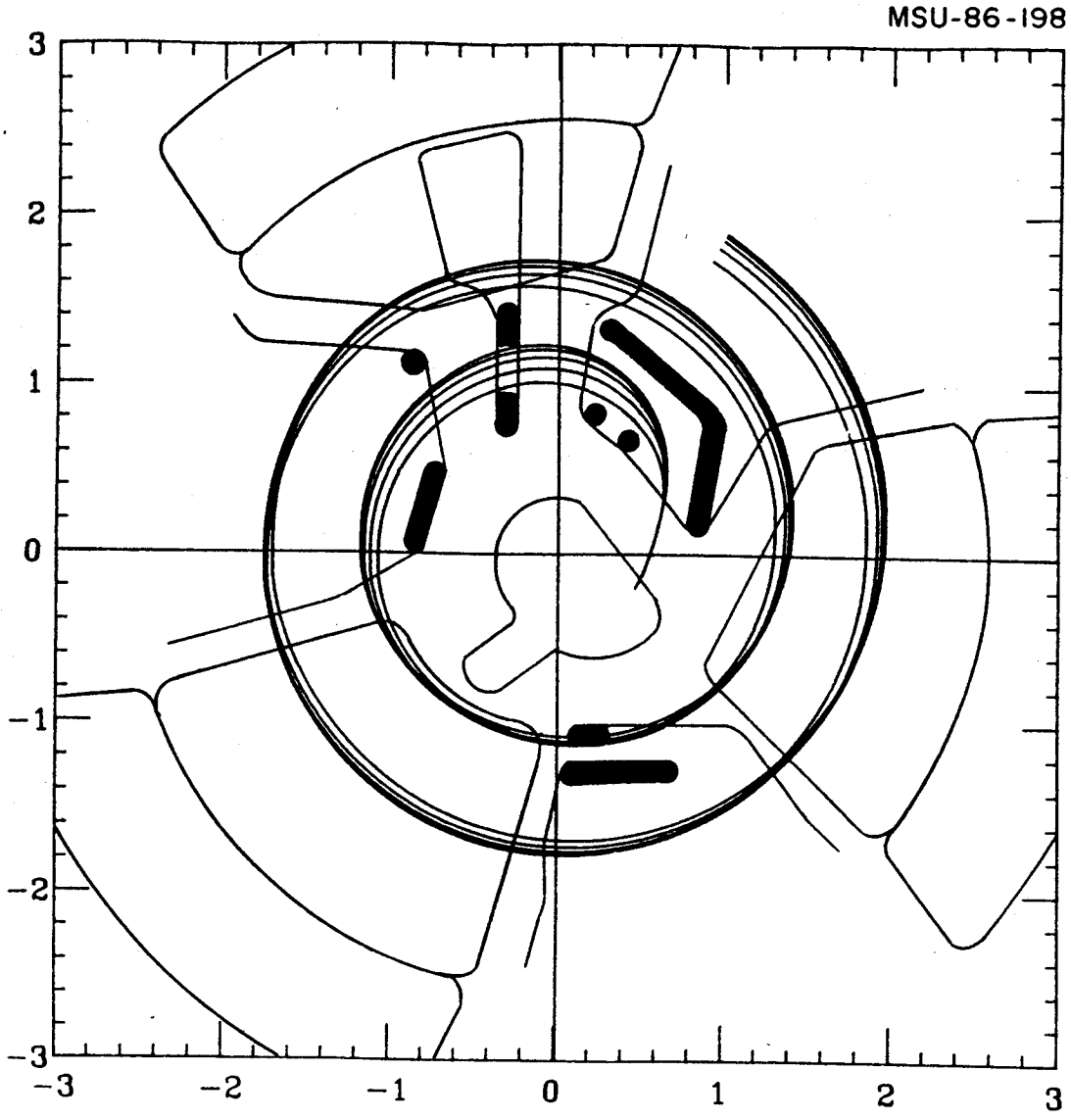

Figure 3-4. The electrode structure for the first harmonic central region with axial injection. The window frame attached to the dummy dee following the puller is used to neutralize the coupling between the first and second dees. Five orbits are shown corresponding to starting times of 230^0 (outer-most at window), 240^0, 250^0, 260^0, and 270^0 (inner-most). By narrowing the radial width of the window it will be easy to remove those starting times lying outside 245^0 to 260^0.

puller gap it is unlikely that many ions outside the 230^{o}-260^{o} range shown can enter the first turn. In the case of later starting times (towards 270^{o}) there is insufficient time to cross the source-to-puller gap, and for the earlier times there is insufficient electric field to pull the ions from the source. The solution in the case of an axially injected beam is quite different as shown in Figure 3-4 for a first harmonic mode. In this central region the RF coupling between dees is neutralized by a window frame structure mounted on the dummy dee which screens one dee from another. By enlarging the radial extent of the vertical sections of this frame it can also be used to select a group of starting times, in this case between 245^{o} and 260^{o}. With this particular central region the $\tau_0=250^{o}$ ray has the least centering error at 15", whereas in the PIG case best centering occurred for the ray with $\tau_0=240^{o}$. In both cases the phase spread transmitted by the narrow slit is approximately $\pm$ 10^{o} around the "centered" orbit.

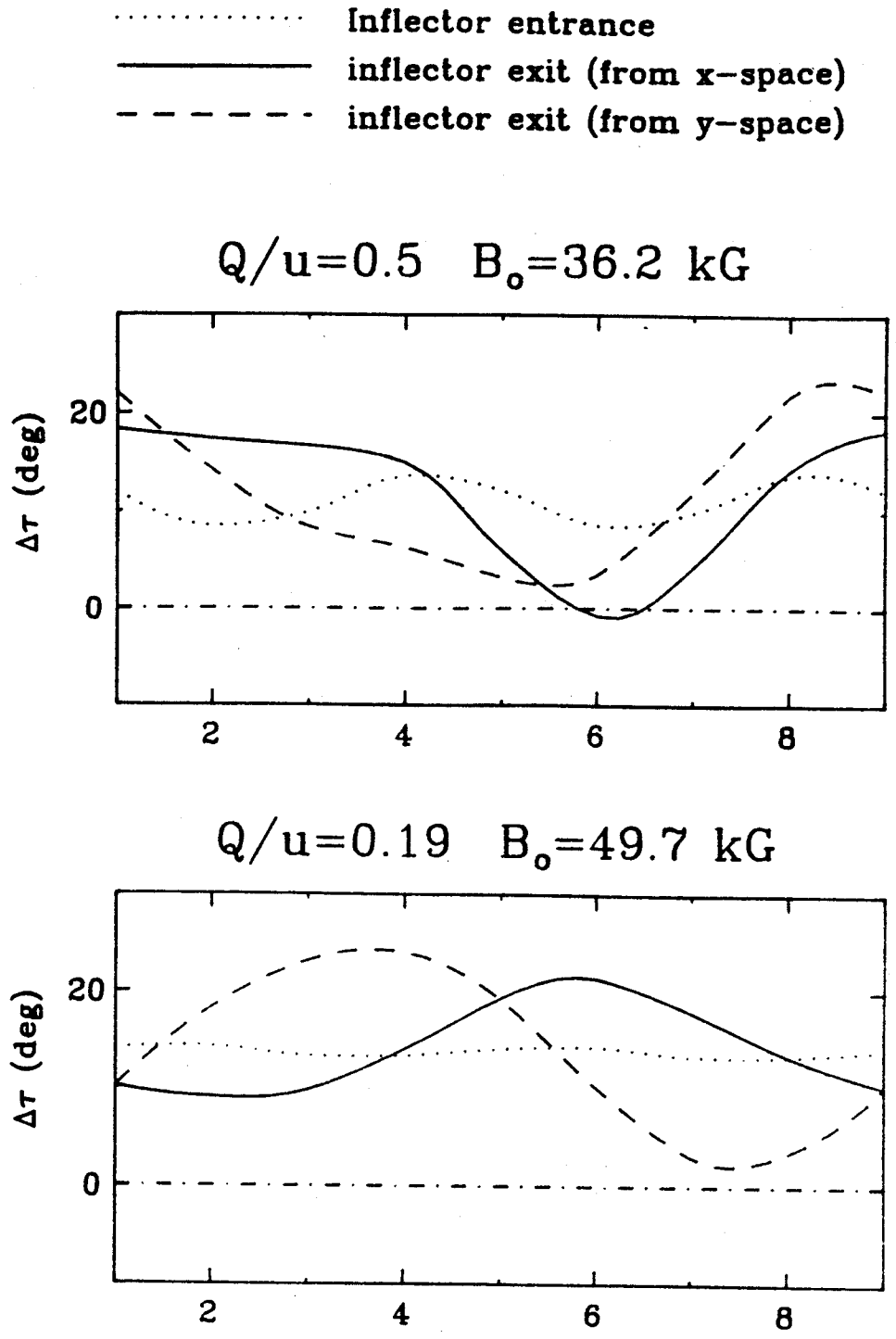

Figure 3-5. RF time differences for particles on the boundary of a 100π mm-mrad phase space with respect to the central ray. The dotted line indicates the difference at the entrance of the inflector. The solid and dashed lines show the differences at the inflector exit. The abscissa is just an arbitrary parameter around the boundary of the phase space.

3.3 Phase Selection for Axially Injected Beams

Conventional wisdom would say that a phase selection system is not necessary when the beam is being axially injected, since the beam can be pre-bunched before entering the cyclotron. In fact we do use a buncher located just before the entry into the cyclotron yoke, but there is a fair amount of de-bunching of the beam as it traverses the yoke[24] and inflector. This debunching is illustrated in Figure 3-5, where the difference in starting times is plotted as a function of particle number. (There are 8 particles distributed around the perimeter of an ellipse.) As the bunched beam will have a phase spread in the neighborhood of ten degrees the beam entering the cyclotron will again have a phase spread of thirty degrees; the only difference now is that the buncher phase is another adjustable parameter. In the case of the axially injected beam there is a further concern that the non-linearities in the spiral inflector will produce a distorted phase space which could make phase selection difficult. To reduce this effect we can work with a small beam spot. It was found that if the analysis system in the beam transport system was used to select a beam with an emittance of 25π mm-mrad (unnormalized) that after the strong focusing that takes

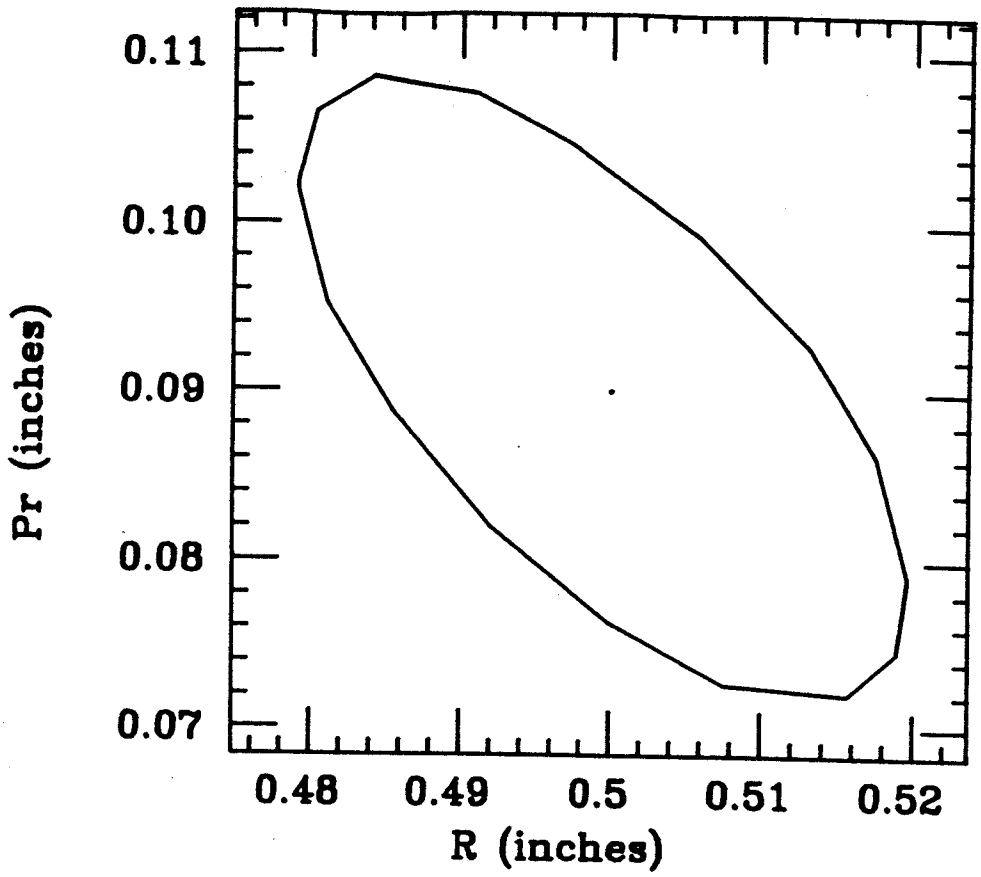

Figure 3-6. The phase space at the exit of the inflector when the initial beam has an emittance of 25π mm-mrad. The momenta have been divided by qB_0 to express them in units of length.

place during the yoke traversal, the beam spot size at the entrance to the inflector would be 1 mm in diameter. The gap in the inflector is 4 mm, so a 1 mm beam should pass through sufficiently far away from the electrodes to avoid serious non-linearities. (See Figure 3-6, a plot of $x\text{-}p_x$ at the exit of the inflector.) To insure that the spot size at the entrance of the inflector is indeed 1 mm in diameter the collimator at the inflector entrance could be replaced with one that has a 1 mm hole instead of the usual 4 mm. In cases where the beam intensity from the ECR ion source is high, this will still leave sufficiently large beam currents to run experiments. So far as distortions are concerned the only remaining question is whether or not the electric fields on the first few turns would distort the phase space. In Figure 3-7 we show the results when a group of eight rays populating the perimeter of the ellipse shown in Figure 3-6 are accelerated forward 3 turns using the Program CYCLONE[25]. This program integrates the equations of motion in the measured magnetic field and in an electric field which has been computed with a relaxation code. For each ray several different starting times were run, so the values of R and P_r at the final position are plotted as a function of the average phase on the last turn. By interpolating to get the

Figure 3-7. The R and Pr plotted for a group of rays that started on the perimeter of the ellipse shown in figure 3-6, after 3 turns, as functions of their average phase. In the middle frame the results of interpolating to find each ray at an average phase of -4^0 is shown. Note the ellipse shows no distortion.

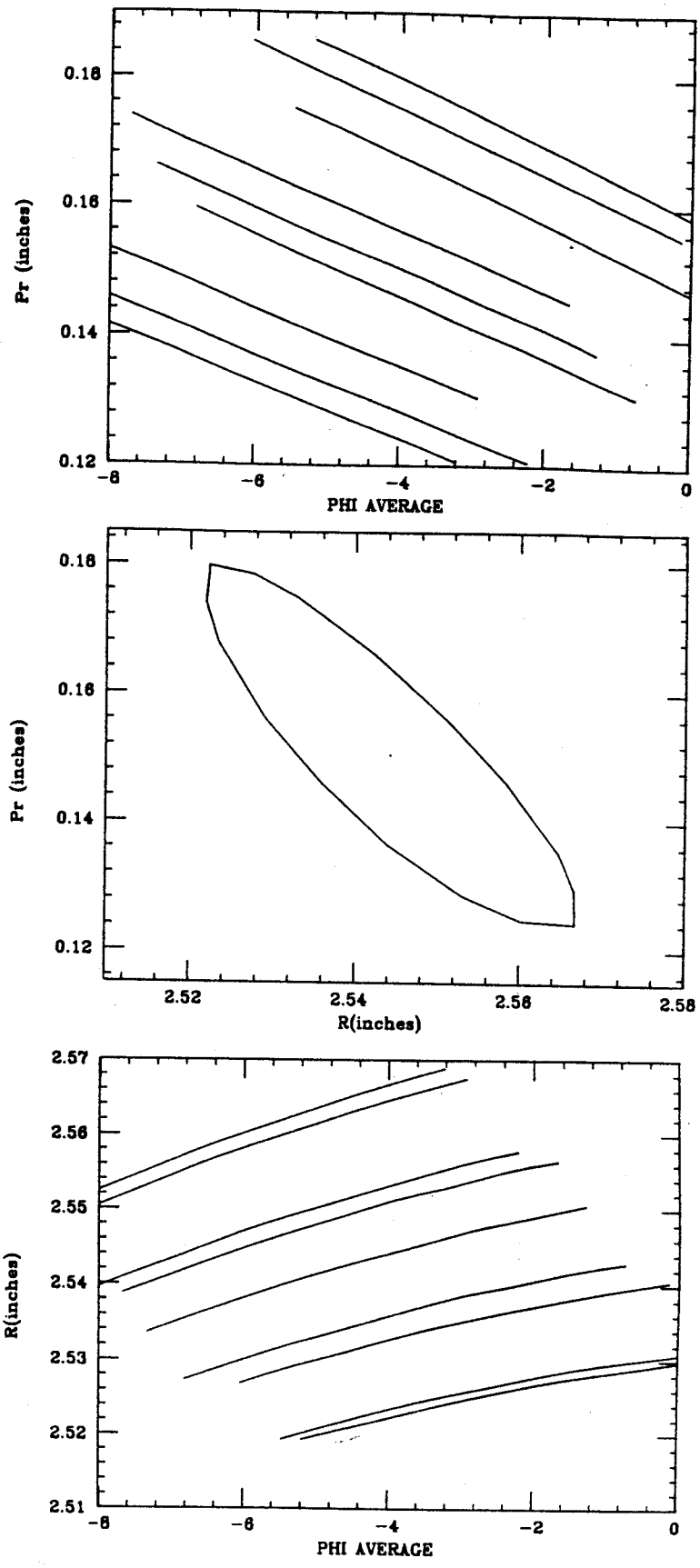
0.18
0.16
0.14
0.12
Pr (inches)
-8
-6
-4
-2
0
PHI AVERAGE
0.18
0.16
0.14
0.12
Pr (inches)
2.52
2.54
2.56
2.58
R(inches)
2.57
2.56
2.55
2.54
2.53
2.52
2.51
R(inches)
-8
-6
-4
-2
0
PHI AVERAGE

Figure 3-7.

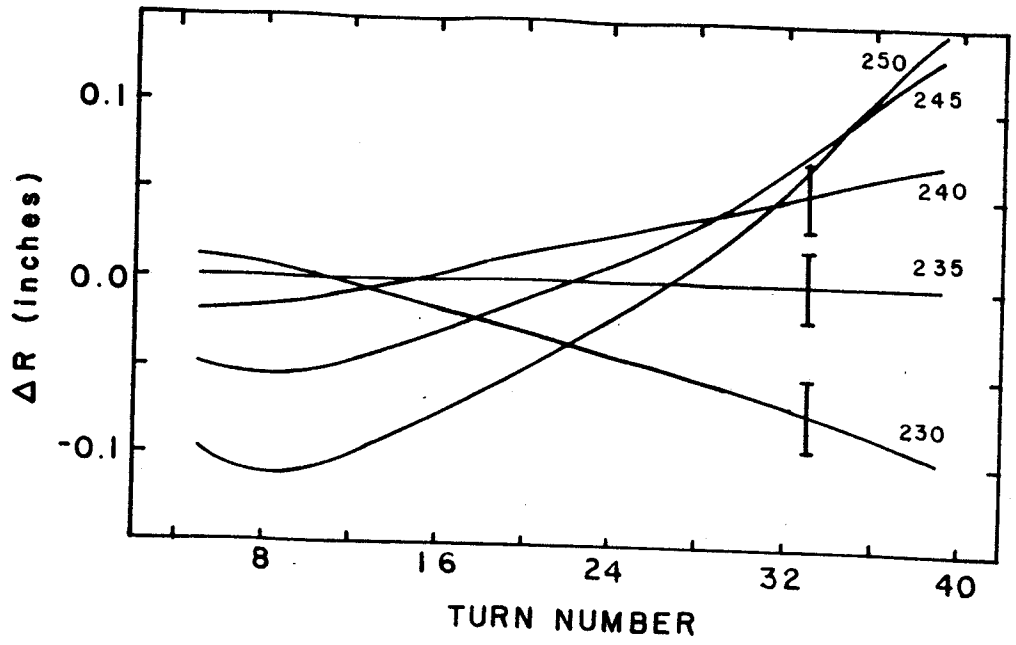

Figure 3-8. Radius difference $r_i - r_0$ at $\theta=84^0$ vs turn number for a family of central rays. Ray 0 leaves the source at $\tau_0=235^0$, the others at the times labeled on the plot. At turn 33 a bar of $\pm.02$ inches is shown to give an idea of the radius variation expected from the r.pr distribution around the central ray.

R, P_r values for the particles with the same average phase we get the ellipse shown in Figure 3-7, which is almost distortion free, as desired. The use of particles with the same average phase is particularly important since these are the particles which will have the same energy gain per turn and therefore they will all arrive at the deflector with almost the same energy. Also by using this grouping of the particles one avoids an apparent distortion which is actually due to the energy dependence of R and P_r.

3.4 Fine Selection

Upon leaving the central region the beam is well behaved and has a phase width of approximately 20^o. It remains to reduce this 20^o to something of the order of 4^o or 5^o. As is apparent in Figure 3-8, at this level of phase selection the radius spread due to the phase is comparable to the beam spot size, so the interaction between these two must be taken into account. To achieve the best possible selection one would like to place the next set of

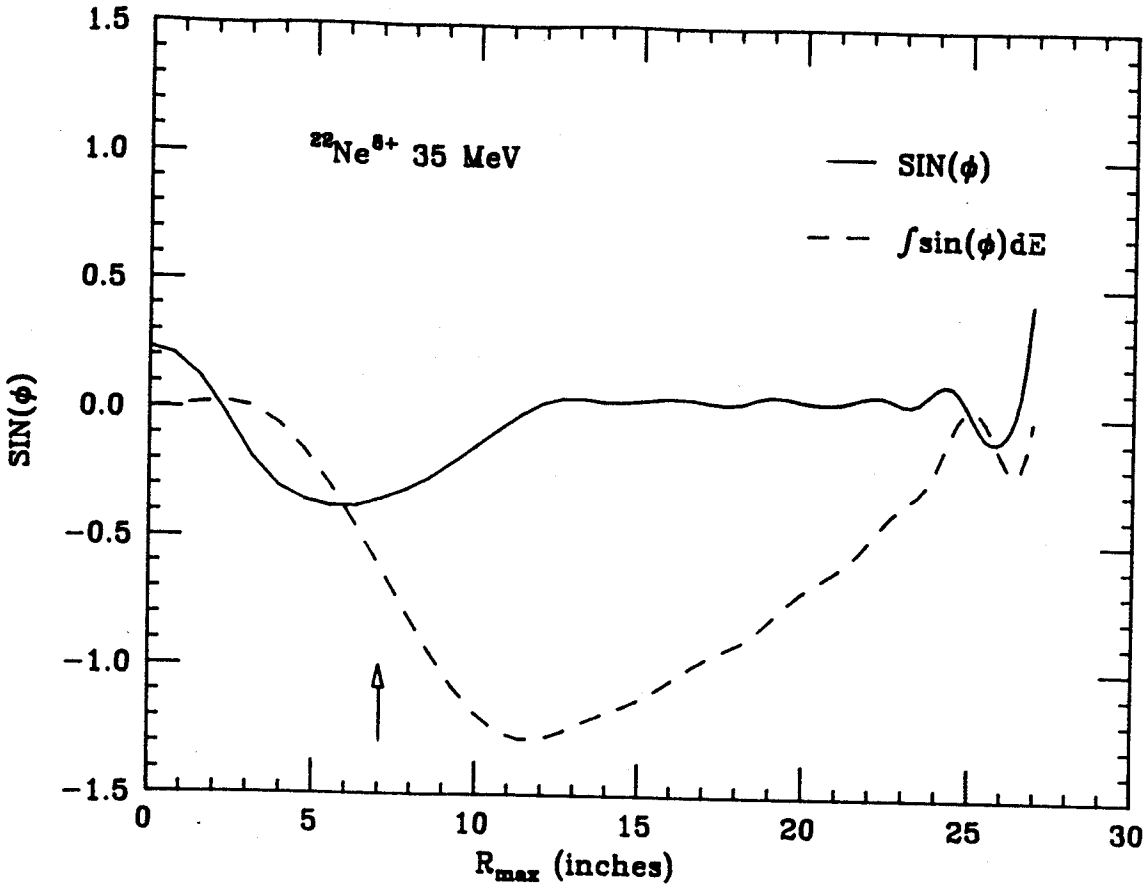

Figure 3-9. A reprsentative K500 phase curve determined using the standard procedures The arrow is located at the radius of the fine selection system.

obstructions where Q, defined by[26]:

$$Q=(\Delta R)/(\Delta \phi) \qquad (3\text{-}1)$$

$$\Delta R = R(\phi_2) - R(\phi_1) \qquad \Delta \phi = \phi_2 - \phi_1$$

is a maximum. At the same time it is advantageous to do the selection as near as possible to the center of the machine, where the beam energy is low, so as to reduce the possible activation of the cyclotron components. At any given radius the ΔR term in equation 3-1 is a result of two separate effects. First there is the change in radius associated with the energy difference between two particles with different phases. It can be shown[26], that a good first order approximation for the energy difference is,

$$\Delta E \simeq - \Delta \phi \int \sin\phi \, dE ,$$

and the resulting radial difference is given by,

$$\Delta R = \frac{1}{2} R \frac{\Delta E}{E} .$$

From these equations it can be seen that the maximum value of Q would be obtained when $\int \sin\phi$ is a maximum. Figure 3-9 shows a representative phase curve and the $\int \sin\phi dE$ for the K500 cyclotron. At 7" the integral of $\sin\phi$ is large but is not at a maximum. Increasing the value of the integral at 7" would entail sharpening the initial drop in the phase curve, which would lead to a quite different phase history for the inner part of the machine. The phase curve shown in the figure has been chosen to meet several important criteria. First the large initial positive phase is chosen to gain electric focusing in the first few turns. The negative excursion and subsequent rise back to zero, which is centered about 6", is a result of tailoring the field so that ν_z at 6.5" does not become too small. At this radius the energy is too large for there to be much electric focusing, but the flutter is not yet at a maximum, so a small gradient is added to the field to raise the vertical focusing. At the same time the initial fall-off of the phase curve (inside 2") is determined primarily by the iron geometry of the cyclotron and thus is not easily changed with the trim coils. It will be shown below that with a phase curve determined by these criteria (such as that shown in Figure 3-9) the Q will be sufficiently large at the phase

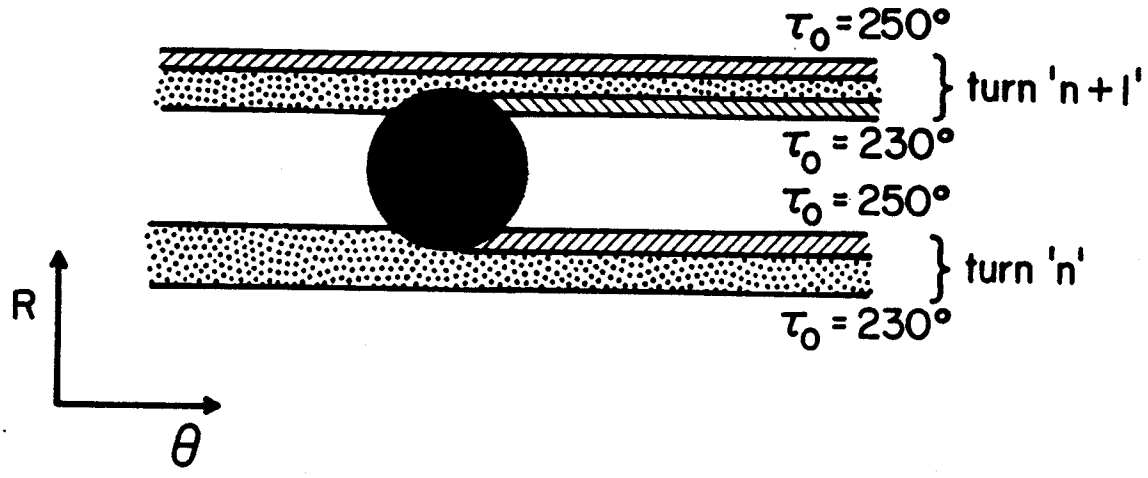

Figure 3-10. A schematic of how a single post can act in a manner similar to a slit. The inner edge of the post scrapes off those particles with too large a radius, while the outside scrapes off those with too low a radius on the next turn. The dotted region is the surviving beam while the cross hatched region is the removed beam

slit location. Since this process also produces a magnetic field with good values of ν_r and ν_z, trim coil power, and the integral of sinø at extraction (near zero), it will be used in the subsequent calculations.

The second source of radius variation with phase is centering. When particles cross the initial gap between the source and the puller the energy they gain is significantly larger than their initial energy, thus their total energy at the exit from the first dee is very sensitive to the voltage present on the dee at the time of crossing. Since the dee voltage is a function of phase the energy will be strongly dependent on the phase of the particle. In the K500 cyclotron the details of the central region require that the phase at the first gap crossing be different from zero, otherwise the radius spread could be made small by running near $\tau_0=270^0$. As seen in Figure 3-4 the variation in energy leads to a large difference in radius at the exit of the first dee. From this gap onward the percentage change in energy at a gap crossing decreases. Soon all the particles have similar rigidities, but the differences in radii remain, so each starting phase will have a different orbit center. All the particles begin their trajectory at the same point (the source exit), so as the orbits precess about the

equilibrium orbit, there will be approximately two locations per turn at which the orbits are all at the same radius. In the K500 the fine selection will be done at two locations, 120^0 apart (but on the same turn). If the phase dependent centering were arranged such that the radii were either dispersed or focussed at one slit location, they would not be at the other location. Phase dependent centering is extremely sensitive to the central region geometry, so the best method of studying it is direct orbit integration, the results of which will be discussed below.

In Figure 3-8 we plot the radius differences $r_i - r_0$ at a fixed azimuth, where r_0 is the ray which leaves a Penning Ion Source at $\tau_0 = 235^o$ (the results for an axially injected beam are qualitatively the same). At the radius of turn 33 (approximately 7") there is a space between trim coil number 2 and trim coil number 3, so at this radius in the center of the hill a 1/2" diameter access hole passes from the liner through the pole and exits on the magnet cap. To preserve the magnetic symmetry there are six such holes but because of the space requirements of the system only two of them are usable, one on hill A and the other on hill B. As can be seen in Figure 3-8 the Q at this turn is quite good (for particles near $\tau_0 = 235^0$), while the turn separation is

still about 100 mils (see Figure 3-1) and the energy is only 6% of the extraction energy. Included in this figure is a bar of ± .02 inches, which is intended to give an indication of the radius variation expected from the x, p_x distribution around the "central ray".

The 100 mil (.100") turn separation at this radius is insufficient to allow the insertion of a slit, but will allow the insertion of a post between turns. Although posts are less common than slits they have been used at other laboratories[26] with good results. In principle, after two turns the post has had the same effect on the beam as a slit, so long as the size of the post is such that it scrapes beam from both the turn before it and the turn after it, as modelled in Figure 3-10. In this mode of operation the high radius particles are scraped from turn "n" on the inner edge of the blade and the low radius particles from the turn "n+1" on the outer edge of the blade. With $\nu_r = 1.01$ the composition of the beam at turn "n+1" is little changed from that at "n" and the post has removed the high and low radii from the successive turns just as a slit would from a single turn.

A more detailed analysis of the selection process, involving the x, p_x spread of the beam, is presented

Figure 3-11. Radius plotted as a function of the starting time for turns 32, 33 and 33 for the PIG geometry in the upper sequence and for turns 29 through 32 in the lower plot for the ECR geometry. Associated with each central ray is a set of 8 rays that populate the circumference of a .02 inch radius circle in R, Pr space. From left to right: the first one shows the situation at θ=84 before the blades are inserted, the next one shows the situation after a 60 mil blade has been inserted at 84^0 and the third shows the effect of inserting a second blade at $\theta=204^0$. The following three frames give the the analogous situation at $\theta=204^0$. Note that the final phase width is around 4 degrees and the full 0.02 inch phase space around the central time survives. The rays with different R, Pr values have a starting phase that gives them the same energy gain per turn as the central ray with which they are associated, thus the horizontal label is actually a measure of the energy gain per turn.

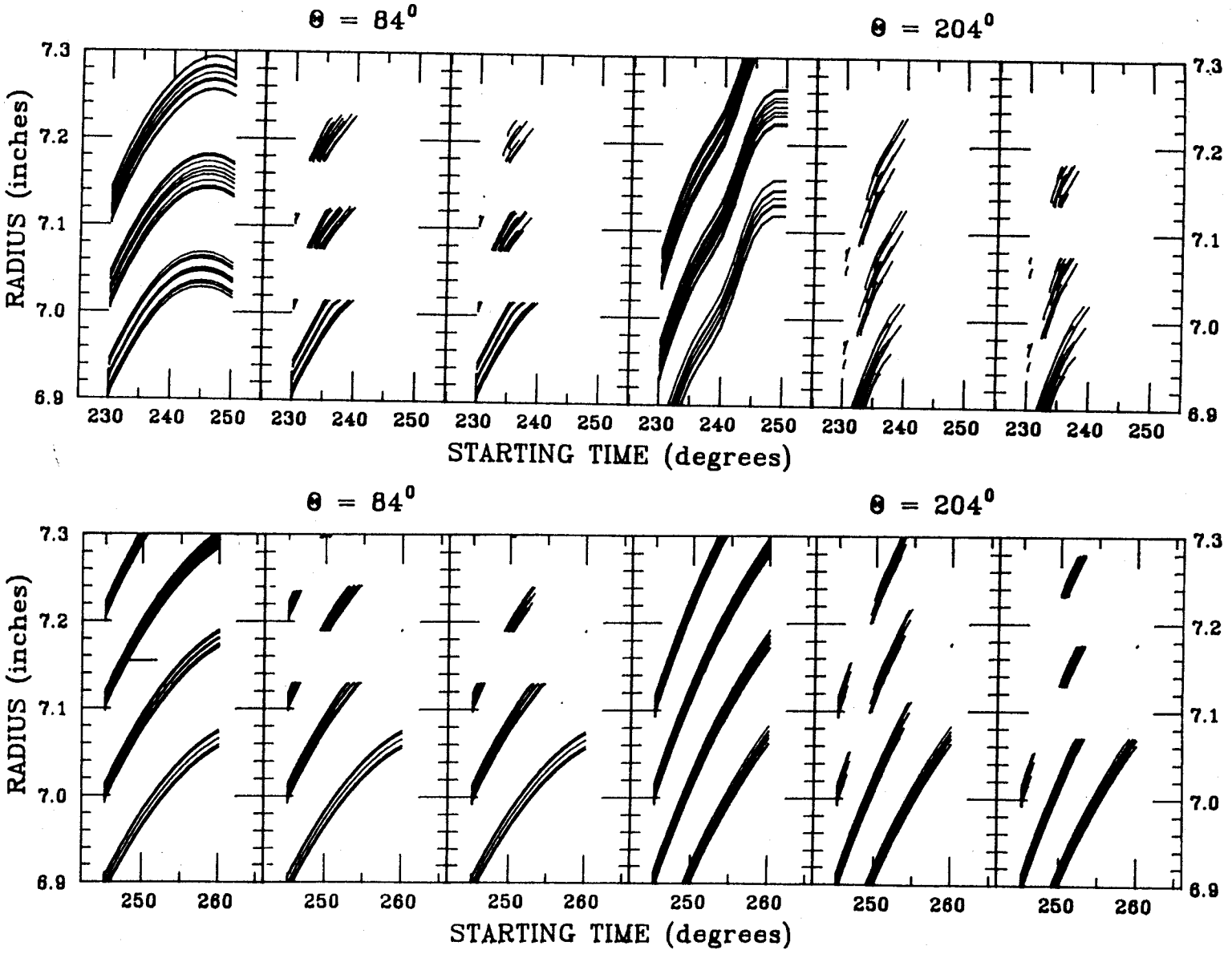
θ = 84°
θ = 204°
RADIUS (inches)
7.3
7.2
7.1
7.0
6.9
230 240 250 230 240 250 230 240 250 230 240 250 230 240 250 230 240 250
STARTING TIME (degrees)
θ = 84°
θ = 204°
RADIUS (inches)
7.3
7.2
7.1
7.0
6.9
250 260 250 260 250 260 250 260 250 260 250 260
STARTING TIME (degrees)

Figure 3-11.

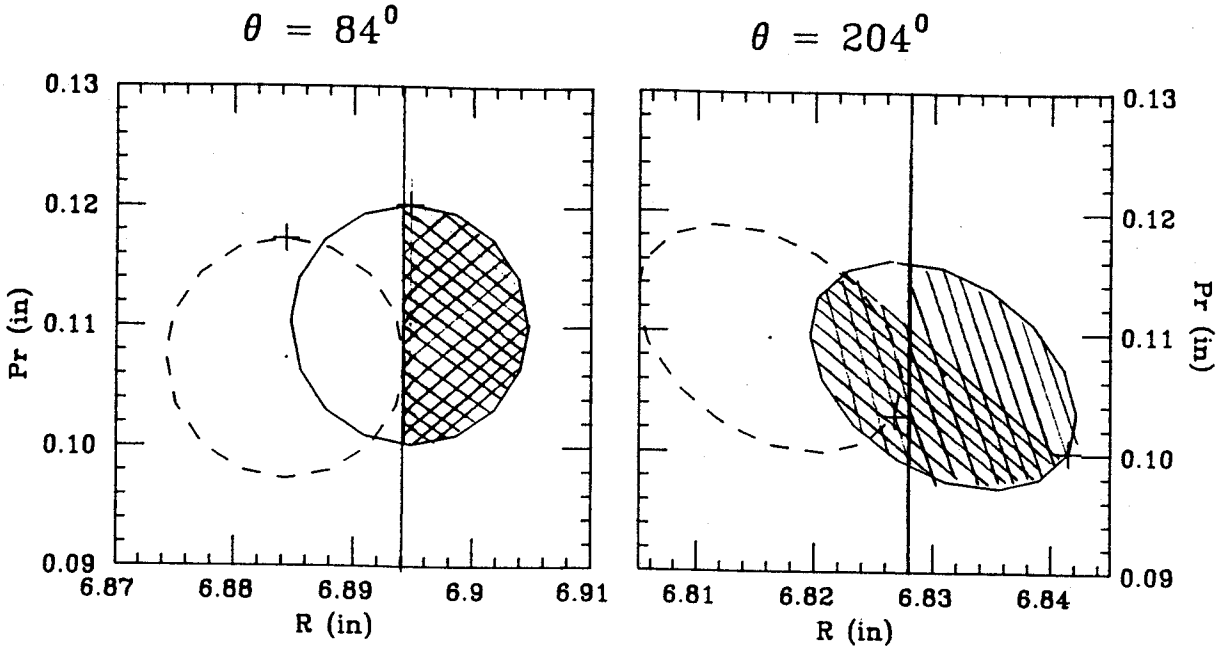

Figure 3-12. A simple demonstration of why two slits are required to do a careful phase selection. Shown are two bundles of rays with a one degree phase difference. Note that at the first azimuth it is impossible to remove all of one phase without affecting the other phase. After the particles have traveled 120^0 in azimuth they have executed a third of a betatron oscillation as highlighted by the cross marking the same ray in both frames. As the shading demonstrates it is now possible to remove almost all of the unwanted phase. In this particular example the two phases are sufficiently close together that a small amount (the unshaded portion) of the unwanted phase passes the second slit.

in Figure 3-11. In this figure we have plotted the radius against a pseudo starting time for three successive turns at the location of the phase slit holes. The horizontal label is referred to as a pseudo starting time because the actual starting times for rays with different values of r, p_r have been adjusted[27] so that all rays with the same horizontal label will have the same energy gain per turn. In the first and fourth (numbering from left to right) the situation is shown with both slit mechanisms retracted. In the second and fifth frames the results are shown after a 60 mil blade has been inserted at an azimuth of 84^o (upper slit mechanism). It can be seen that this blade provides most of the phase selection desired, but it is still necessary to eliminate those unwanted particles whose betatron oscillations have placed them at the same radius as particles with a desired phase. To do this final cleaning up operation a second slit is required. At this radius in the K500 the radial focusing frequency ν_r is close to 1.0. After the azimuth has changed by 120^o, those particles whose large x components moved them towards the radius of the desired phases will now have moved away from the desired phases, as illustrated in Figure 3-12. In the figure two bundles of rays that differ in phase by

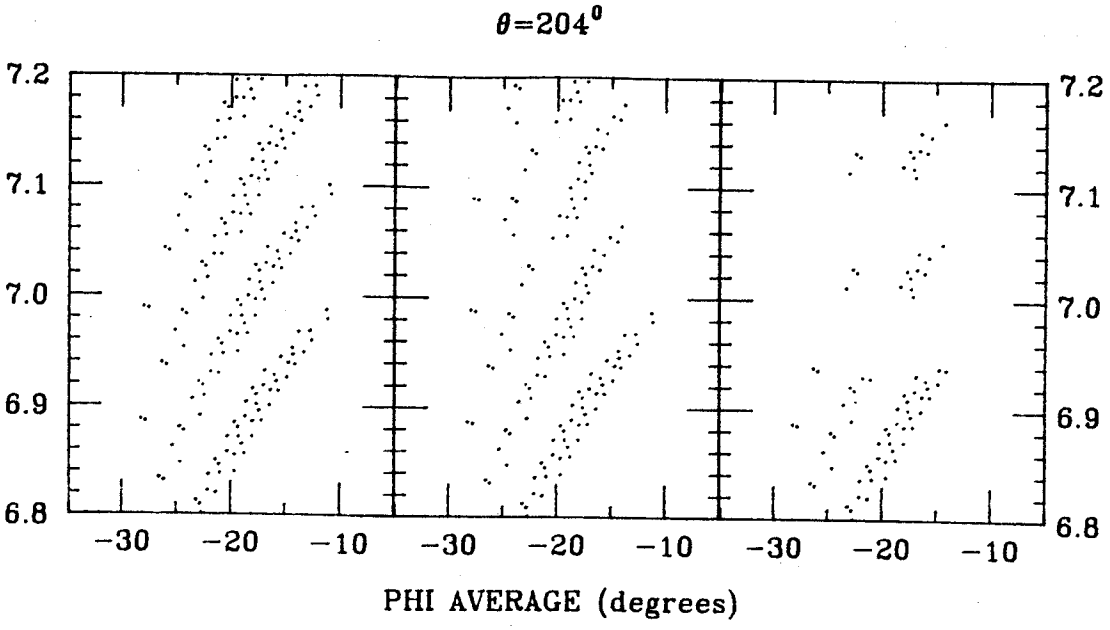

Figure 3-13. The radius plotted at the azimuth of the lower slit as a function of average phase (a good measure of the energy gain per turn) for a distribution of particles which pass through the first turn slit. In this run the first and second harmonics are present in the magnetic field, so it should be compared to figure 3-10, where the particles were run in a field that had perfect three fold symmetry. Four different turns are plotted. In the first frame on the left no slits are present. In the middle frame the upper slit has been inserted, and in the final frame both slits are inserted.

one degree are plotted. As the shading demonstrates, with two slits it is possible to remove almost all of one phase (to the right of the line) while not removing any of the particles whose phase is one degree different. In this example the two phases are sufficiently close together that a small amount (the unshaded portion) of the unwanted phase passes the second slit. The closer the phase of a bundle is to the desired phase, the larger the unshaded region becomes. (In other words, more of the horizontal phase space associated with that phase passes the slit.) It is the particles in the unshaded area which eventually produce the sloping sides of the gaussian-like peak seen in a beam current versus phase plot. In the third and sixth frames of Figure 3-11 the result of placing such an obstruction at an azimuth of 204^{o} (lower slit mechanism) is shown. The group of rays present in the final turn has a phase spread of $\pm 2^{o}$ around the chosen central phase. By correctly tailoring the phase curve and the RF frequency, the particles with the central phase will have the maximum energy (within a given turn) at the outer radii of the machine. In chapter 5 these computations will be compared to experimental results.

3.5 Further Considerations

The discussion up to this point has made use of orbits which were computed in a magnetic field having perfect three fold symmetry. In actuality there are small, but nonetheless important, first and second harmonic components in the K500 magnetic field. When the imperfections are present, care must be taken to center the beam if a truly well defined beam (a primary goal of phase selection) is to reach the extraction radius. At the radius of the phase slits the strongest controls on the beam centering are the relative dee voltages and the relative dee phases. At the same time the dee voltage can be used to fine tune the position of the turns relative to the posts. The technique would then be to provide a reasonably centered beam at the posts by using the relative dee voltages and phases, and the right positioning (fine adjustment only) by using the average energy gain per turn (sum of the dee voltages). The centering at the posts cannot be perfect, as it is desirable to obtain the best centering at a higher radius where the turn number is larger. This centering is achieved by using the center bump coil. In the case of the K500 there is not complete freedom to set the bump coil since it should be set to values which

reduce the first harmonic in the region of the $\nu_r = 1.$ resonance at 5.5".

In the case of a main field for a particle with a charge-to-mass ratio of 0.25 and a final energy of 25 MeV/n, a center bump setting of B_1=12.1G ϕ_1=-70.2^0 meets these criteria. When orbits are run in this field the selection process is not significantly changed as can been seen in Figure 3-13 where data similar to that in Figure 3-11 is shown. In fact those differences that do occur between the case plotted in Figure 3-13 and that in Figure 3-11 can be attributed to the different phase curve used in the two cases. This highlights the need to optimize the phase curve and the starting phase (by positioning the first turn slit) and the size of the posts. The next Figure (3-14) continues the calculation in a field of three fold symmetry the rest of the way out to the deflector entrance. This shows that at least in principle, single turn extraction can be achieved in the K500 cyclotron when running in first harmonic mode. To achieve single turn extraction, however, much work is needed to verify the stability of the various systems, and to determine the correct centering conditions at the resonances near extraction. The phase curve and frequency

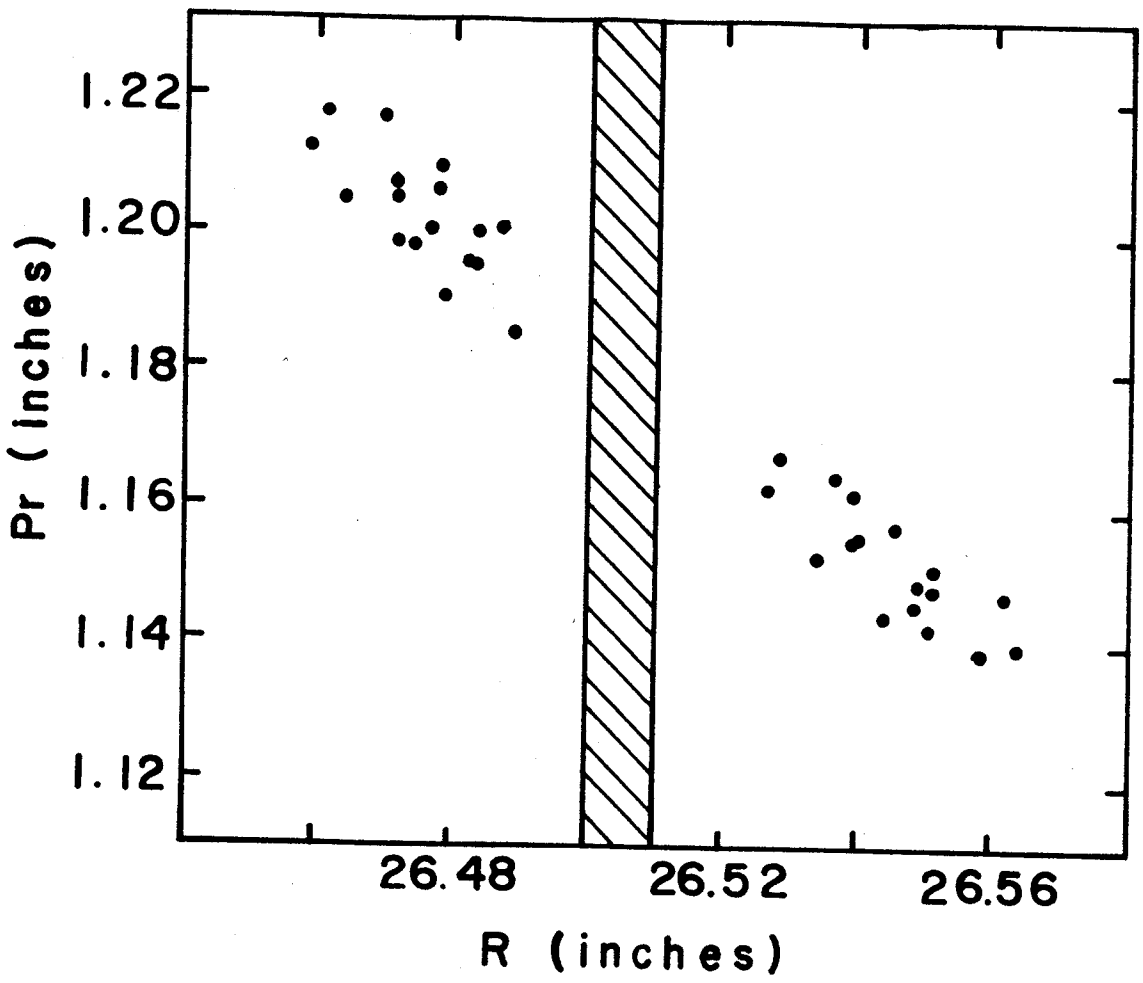

Figure 3-14. R plotted versus Pr for turns 507 and 508 at θ = 336, corresponding to the entrance to the electrostatic deflector. Pr has been divided by $m\omega_0$ to express it in inches. The shaded area corresponds to a possible location of the deflector septum. This plot shows that single turn extraction of the resulting beam should be possible. The energy spread of this group is less than 6 parts in 10^4.

need to be tailored carefully as well by using the procedure described by Gordon[28].

4. Phase Selection Hardware and the VP Probe

4.1 Introduction

During 1985 hardware was constructed to perform the experiments discussed in chapter 5. All of this equipment was constructed for general operational use on the K500 cyclotron. These components fall into two groups; those concerned with phase selection only, and those oriented towards general beam diagnostics. In the second group is the viewer port probe that has proven to be a valuable every day diagnostic device. In the first group is the hardware required to accomplish phase selection as described in chapter 3.

4.2 Phase Selection Hardware

As described in chapter 2, phase selection in the K500 cyclotron requires two small tungsten blades to be inserted between turns 32 and 33 on successive hills. Easy insertion and removal of the blade from the beam chamber and adjustability of the slit position (to accomodate different orbit patterns) were seen to be desirable features of a phase selection system. Also, since the lifetime of the

blades was uncertain, a large effort was expended on developing the ability to change blades with minimum disruption of cyclotron operation. This last feature would also allow for adjustment of blade size (by changing the blades), which is analogous to changing the slit size in a conventional system. Access to the median plane on the hills consists of two, half inch diameter holes located near the center of hills "A" and "B" (see Figure 1-2) at a radius of 7.038". The hole on hill A (θ=83.5^0) emerges on the upper pole cap, while the other (θ=203.5^0) emerges on the lower cap. This requirement is imposed by the relative locations of the center plug gate valves.

The features required are realized by mounting a one inch long tungsten blade (pin) off-center in a small copper cap that is bolted onto the end of a forty inch long stainless steel shaft traversing the magnet poles. Since the pin is located off-axis, rotating the shaft in the access hole results in the desired adjustability in the pin's radius (and an unimportant change in its angle). Moving the shaft up and down by one inch will move the blade in and out of the beam chamber, while pulling the shaft all the way out will allow changing the blades. In actuality the shaft is two concentric stainless steel tubes set up in a spray tube

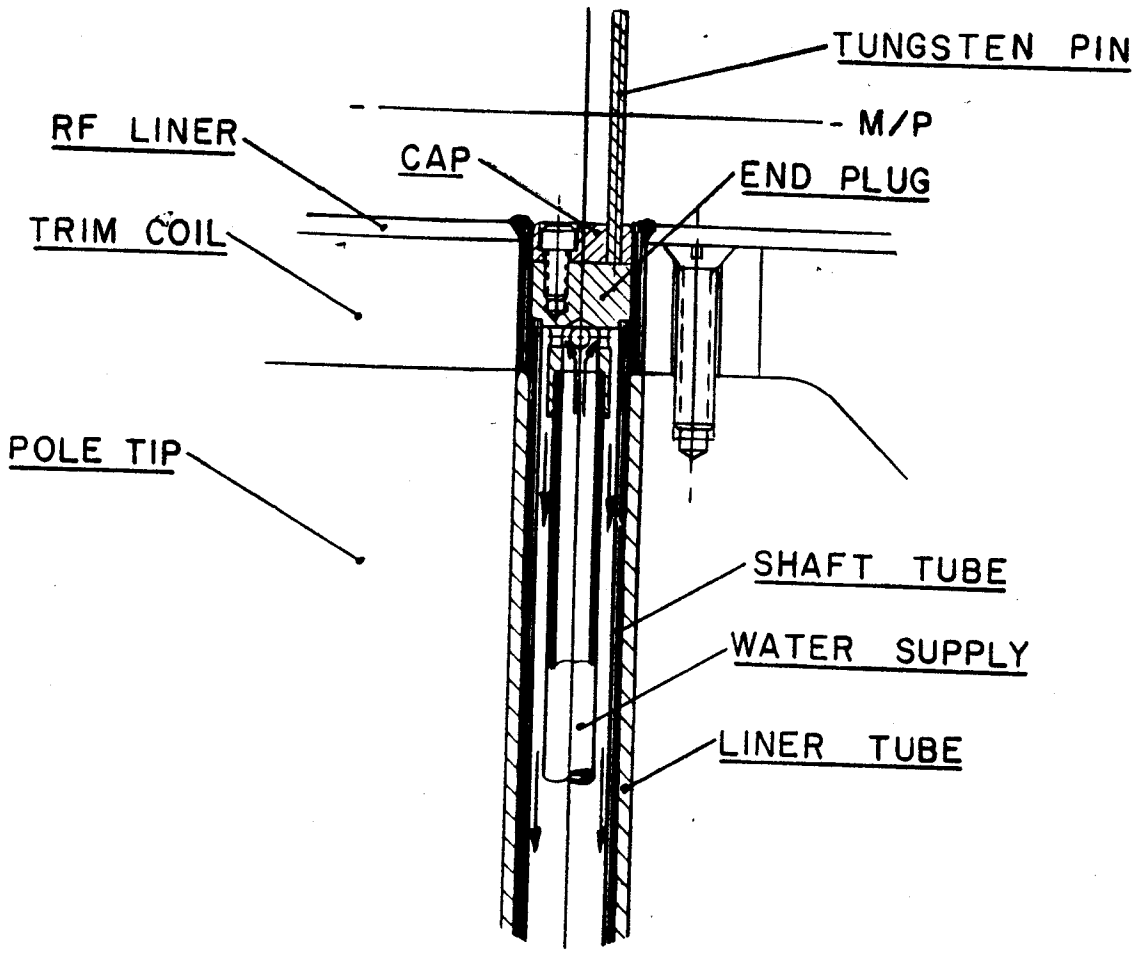

Figure 4-1. The end of the shaft at the median plane of the cyclotron. The sixty-two mil tungsten pin intercepts the unwanted beam. The pin is mounted in a copper cap which is easily removed for rapid pin change. Note: the copper end plug is water cooled so the tungsten will be indirectly cooled.

configuration (as shown in Figure 4-1) so that the beam end of the shaft is water cooled. This feature indirectly cools the tungsten blade which will intercept the unwanted beam.

Control of these functions is provided by a mechanism located between the center plug and the dee stem on the pole cap at the exit of the access hole. The access hole lies beneath the flared portion of the dee stem spinning; the limited space available requires the compact and intricate device shown in Figure 4-2. It can be seen in this figure that the mechanism consists of two major groups of parts, those below the bellows which are rigidly fixed to the pole cap, and those above which are moved up and down on a pair of rails by the pneumatic cylinder. It is this one inch of bellows motion that allows the shaft to move so that the blade can be inserted into, or retracted from, the beam chamber.

Located at the top of the moving section is the rotating water manifold. Inlet water surrounds the shaft in the small chamber formed by the first two coaxial O-rings, passing through the four radial holes in the shaft to reach the center tube. The water returns from the tip between the inner and outer tubes, flowing out through another set of 4 radial holes into the the small chamber formed by the second and third O-rings. Just below the third O-ring the shaft

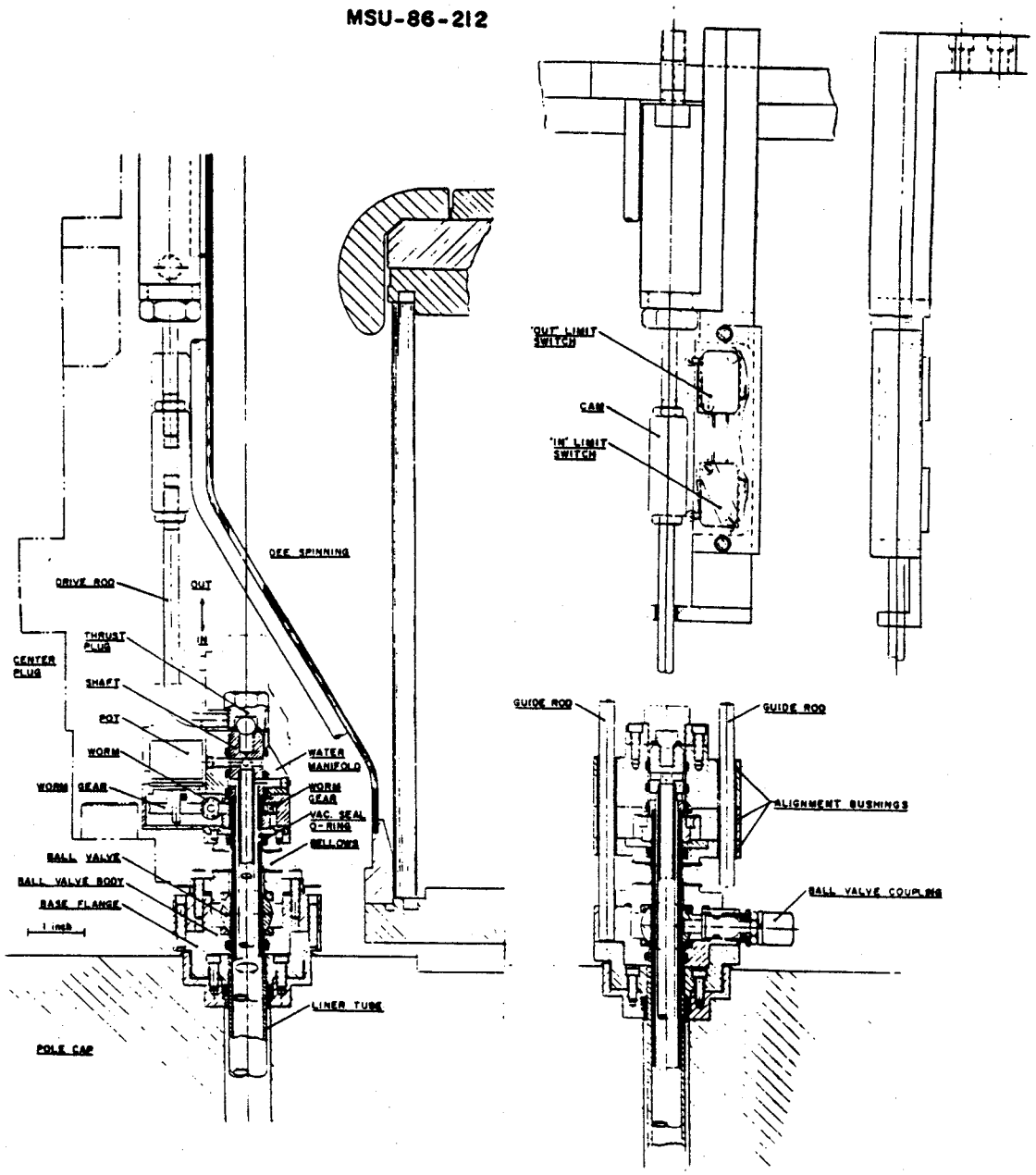

Figure 4-2. Cross section of the phase slit drive mechanism. See text for a description

diameter is reduced to form a shoulder which rests on the worm gear. When the thrust plug screw is tightened this shoulder and the ball bearing in the thrust plug trap the shaft axially so the shaft must travel in and out with the action of the air cylinder. A key on the shaft just below the shoulder mates with a keyway in the worm gear; turning the worm gear causes the shaft to rotate. On the opposite side of the worm, a second worm gear is mounted on a servo potentiometer, providing information about the rotational position of the shaft. The driving worm is driven by a motor mounted three feet away on the dee stem support beam. Torque is transmitted from motor to worm gear by flexible drive cable. This system was chosen so that there would be sufficient room to shield the synchronous motor from the high magnetic field.

The ability to change the blades with the minimum disruption of cyclotron operation requires removing the shaft without raising the cap or otherwise breaking high vacuum. The blade-changing operation begins by removing the thrust plug, exposing a set of threads in the top of the shaft. Removing the two copper patches in the dee stem spinning allows a rod to be passed through the spinning and threaded into the the top of the shaft. Pulling on this rod draws the shaft out of the cyclotron, while the sliding seal

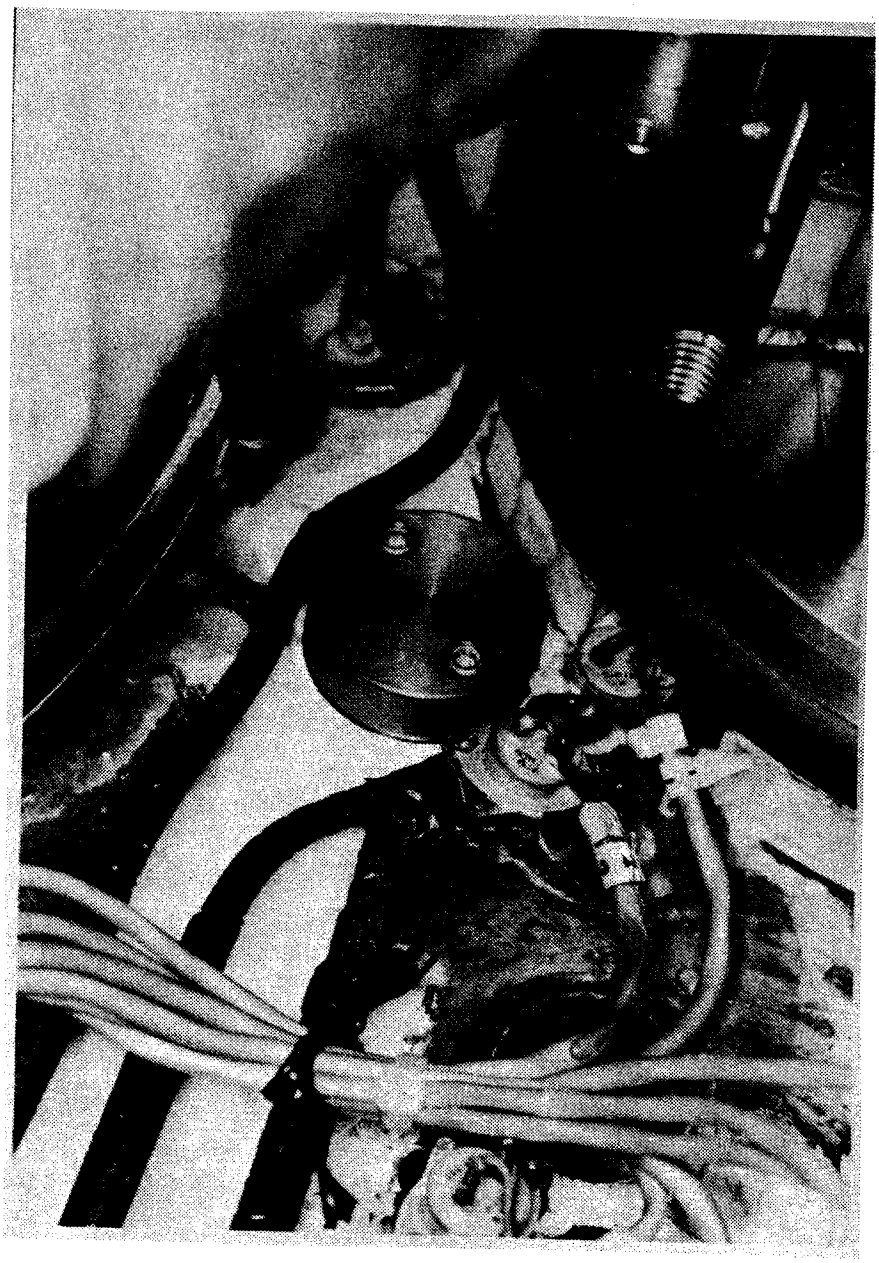

Figure 4-3. The lower phase slit hole before the trim coil leads were moved.

O-ring maintains the vacuum. When the piston is in the retracted position the bellows forms a lock chamber sufficient to accomodate the pin and cap assembly. The ball valve can then be closed using a 1/4" drive rachet wrench to turn the the brass ball valve coupling one quarter turn. Once the valve is closed the shaft can be retracted the rest of the way. Insertion is accomplished by reversing these operations.

The parts below the ball valve form the mount for the rest of the assembly. The base flange is threaded so that it screws onto the tube which separates the liner vacuum from the main vacuum. When fully threaded on, it also compresses the O-ring making the liner vacuum seal. To prevent this flange from backing off, screws pass through 4 of the 12 clearance holes in it and thread into the pole cap. The redundant clearance holes were necessary since the point at which the threads on the liner tube would bottom out was unknown. Above the base flange is the ball valve body, which is also the support for the guide rails. Since the guide rails must have the correct orientation relative to the dee stem, all orientations were made possible by having the bolts holding the ball valve body to the base plate pass through thirty-degree-wide clearance slots to pick-up four of the twelve available threaded holes in the base plate.

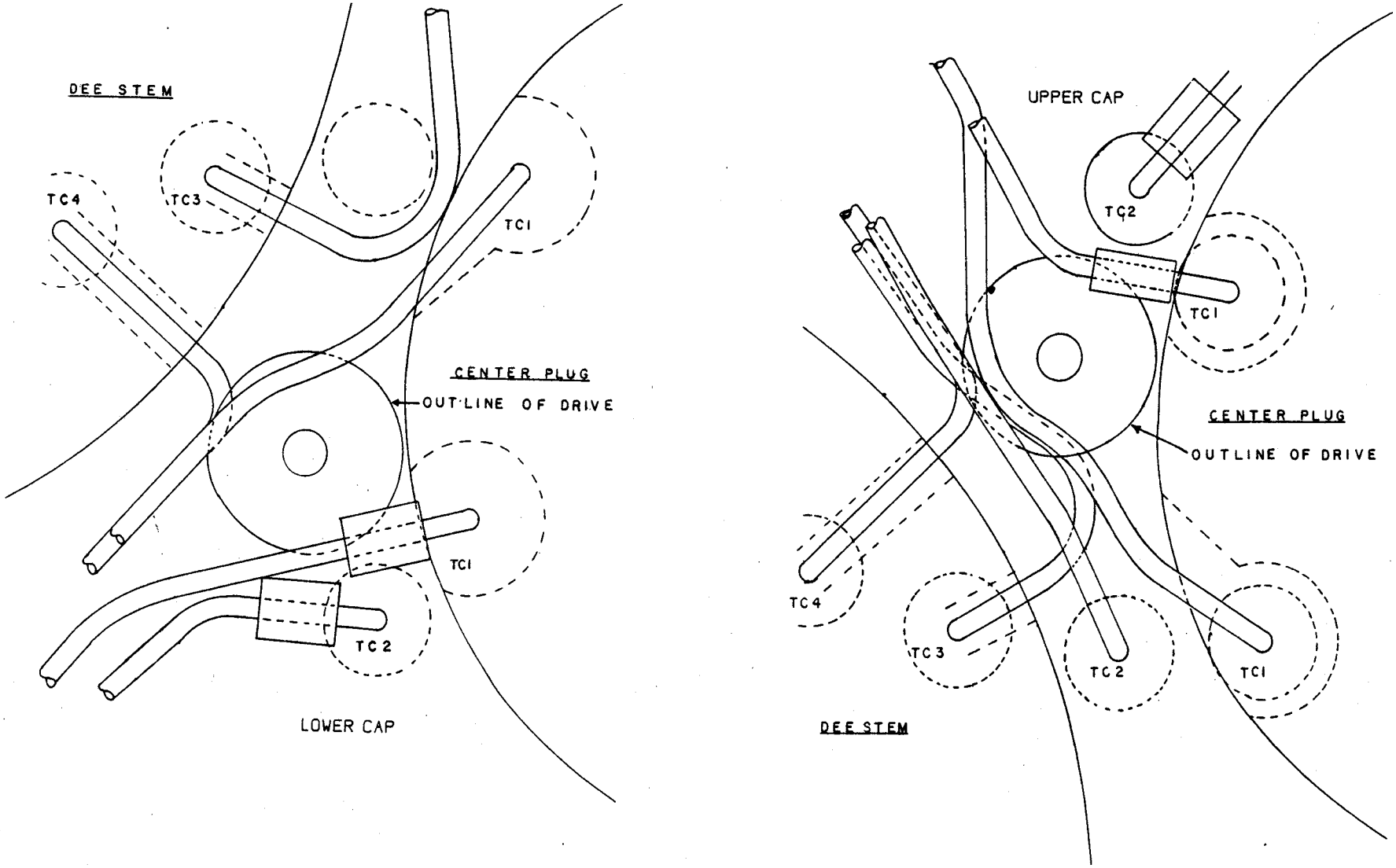

Figure 4-4. A schematic of the trim coil leads in their positions before moving. It can been seen that in both cases several leads seriously encroached on the phase slit drive space.

4.3 Installation of the Phase Slit Hardware

The photograph in Figure 4-3 shows the lower phase slit hole before installation of the hardware. As can be seen in this figure and in Figure 4-4, some trim coil leads passed through the space required by the phase slit drive. This would not have been true had the leads conformed to the designed configuration. Therefore the first part of the installation process was devoted to re-routing the errant leads. To facilitate this operation both the upper and lower center plugs were removed. Next the center plug extensions and the gate valves were removed. After removal of the the hill extensions, the center plug liners were unbolted and pulled out as far as the dee spinnings would allow, about six inches. This disassembly exposed the flare fittings on trim coil #1, and improved the access to the fittings on some of the other trim coils. In all cases the leads were either cut or unsoldered at the transitions between the 1/4" and 3/8" copper tube. In those cases where the feed-throughs were exposed, the flare fittings were undone and the segment of 1/4" line was re-manufactured. For trim coils #3 and #4 on the upper cap and trim coil #4 on the lower cap, the feed-through lies beneath the dee stem spinning. Here, with the cut end free, the leads were bent using the modified pliers shown in Figure 4-5. During this operation care was

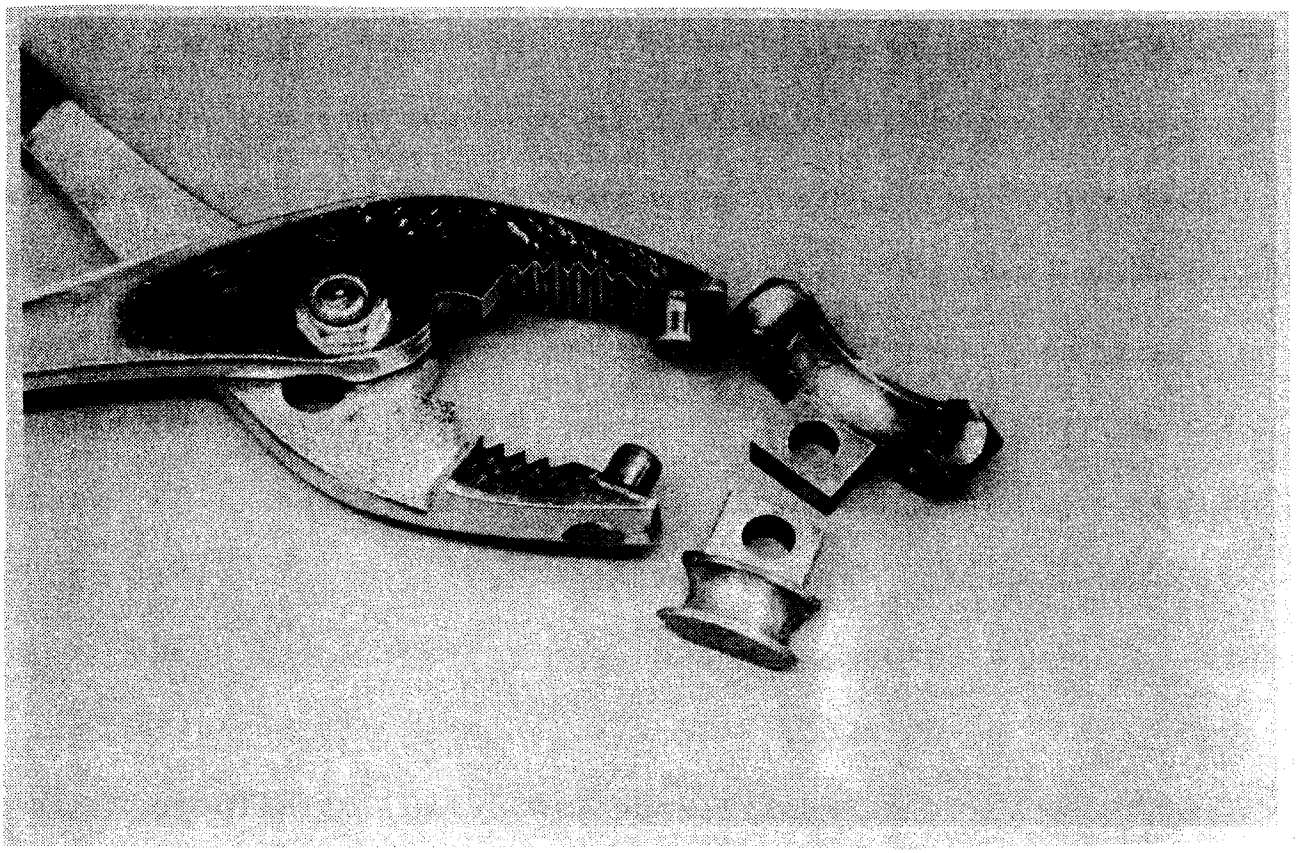

Figure 4-5. The special pliers built to allow bending those leads which were trapped under the dee stem spinning. With a little care they could be used to move the leads without crimping the lead or putting force on the feed-through.

taken to apply as little force to the feed-throughs as possible, because they are known to be fragile. With a little practice this bending technique proved to be quite efficient and simple. After the bending was complete the leads were re-insulated, the transitions were soldered together, and the leads water tested. At this point we also cleaned all the feed-throughs and repaired any damaged insulation on any of the other coils. (This work seems to have removed a short that existed in lower trim coil #1.)

With the trim coil leads in the proper locations, the phase slit base plate could be screwed on and the center plug liner re-installed, thus restoring the liner vacuum. Next came the task of making the access holes in the dee stem spinning and spinning flanges. Location of these holes was accomplished with the special tooling fixture shown in Figure 4-6. When the rod with the sharpened point was passed through the pole to the median plane, striking this rod with a hammer created a locating mark on the spinning. Using a right angle drill and a 19/32" bit, a hole was drilled perpendicular to the surface of the spinning and centered on the punch mark. Using a hand file, the hole was enlarged in the vertical direction so that an oval shaped hole was formed which would allow a 9/16" shaft to pass through freely. The holes in the upper flange were drilled with a

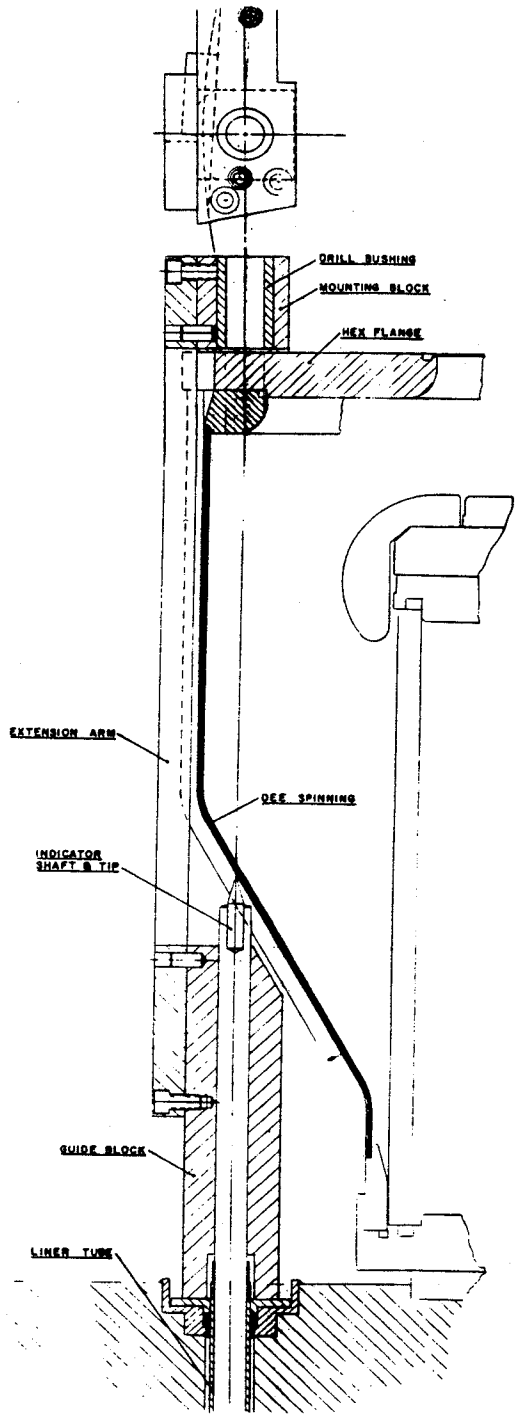

Figure 4-6. The fixture used for locating the hole in the dee stem spinning. The other end of the indicator shaft was at the median plane so it could be tapped with a hammer to mark the spinning with the sharpened point. The drill bushings provided alignment of the clearance hole and the two threaded holes for mounting the air cylinder on the hex flange.

portable drill press, while the lower ones were made with a hand drill motor. In both cases the drill was guided by the drill bushings in the locating fixture.

In order that the half-inch shaft might pass freely through to the median plane, the bead formed where the liner tube is welded to the liner was cleaned up with a combination of oversized hand reamers and a file. With this work complete, the drive mechanisms could be mounted and the shafts installed.

After the motors were installed it was found that there was excessive wind-up in the flexible drive cables. This difficulty was resolved by changing to a larger diameter drive cable and improving the alignment of the worm gear and the worm. With these modifications the drive performed quite well.

To calibrate the position of the pin, the fixture shown in Figure 4-7 is used. By placing the U shaped slot over the dowel pin in the dee locating fixture and rotating the phase slit shaft until the cap fits onto the the end of the shaft, the location of zero degrees can be found.

The complete installation of the phase slits excluding the drive cable modification and alignment took close to two weeks to complete. Over half of that time was devoted to re-routing the trim coil leads.

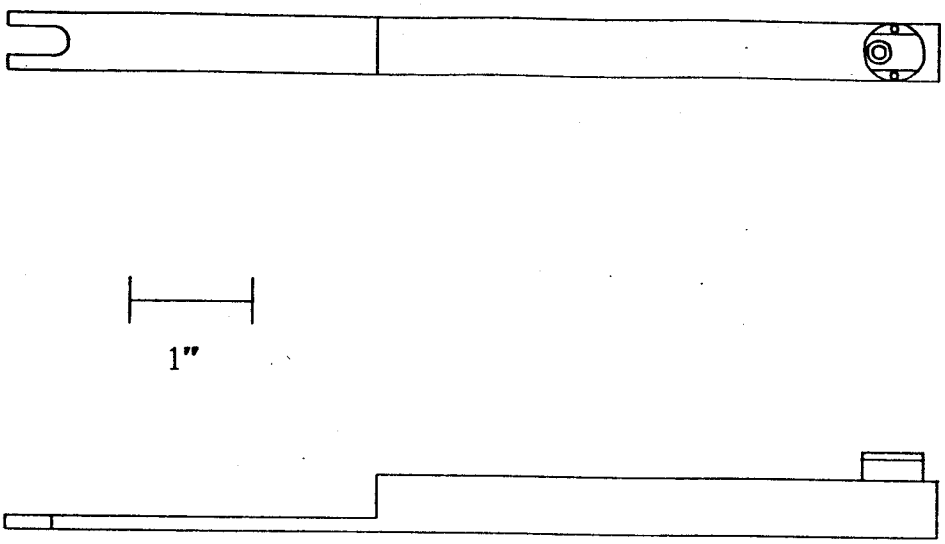

Figure 4-7. The fixture used for setting the angle of the drive. The cap on the end fits over the end of the shaft when the normal cap with pin is removed. The notch fits over the post on the center locating fixture so the rotation of the shaft is determined at either 0^0 or 180^0.

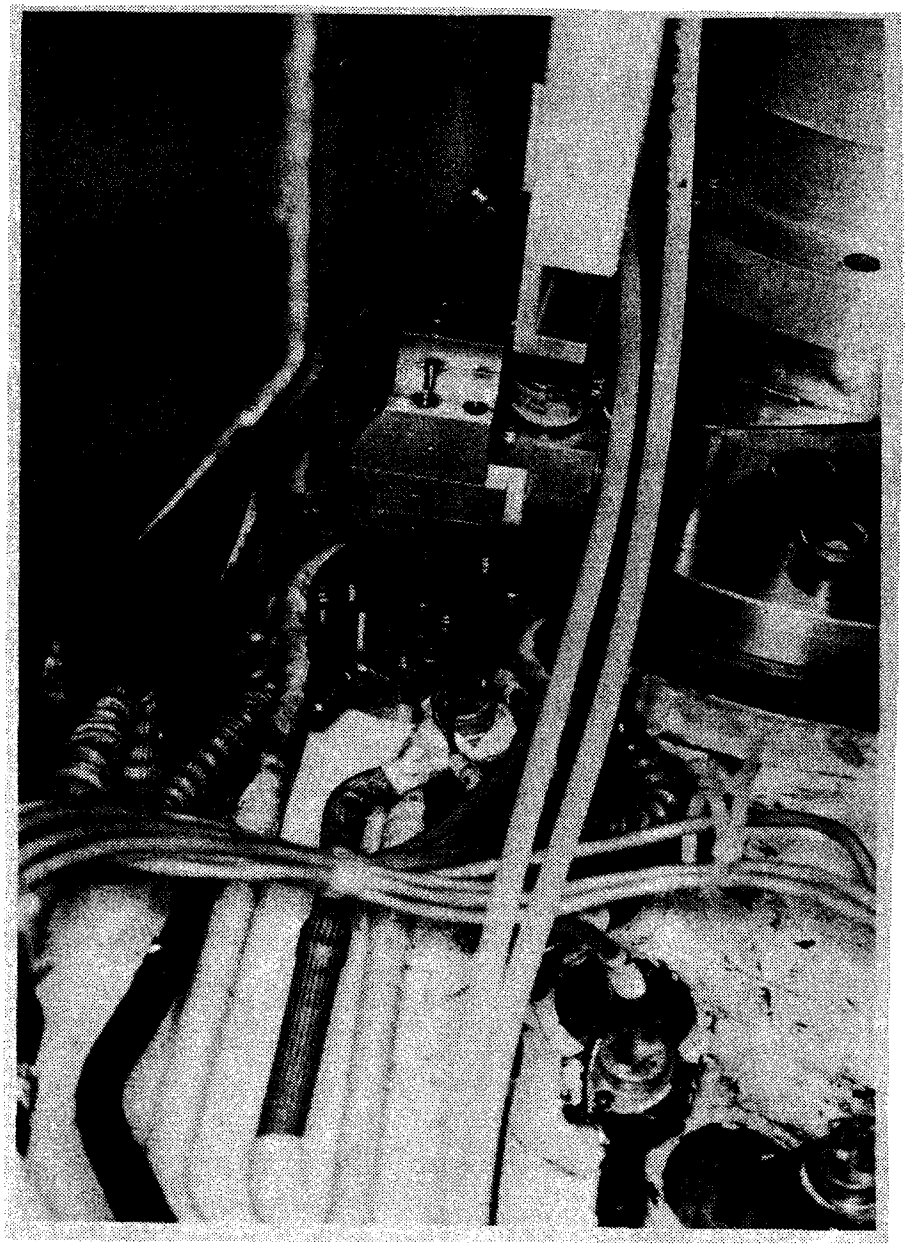

Figure 4-8. The lower drive mechanism installed. See text for a description.

4.4 Construction of the Viewer Port Probe

During commissioning of the K500 cyclotron, a relatively simple two jaw radial probe was installed in the extraction region. The success of this device led to a decision to construct a more sophisticated model which could be removed under vacuum and would increase the travel from 4" to 12". After extensive design and assembly work in 1985 such a device was installed on the cyclotron in November of that year.

Figure 4-9 is a schematic view of the probe as constructed. During normal operation the lower table is locked in the innermost position and the upper table (a precision slide table) is moved in or out with a ball screw driven by a stepping motor. In this 'running' condition the moving vacuum seal is provided by the stainless steel bellows mounted between the front plate and the upper table. To remove the probe the lower table is driven to its outer limit so that the end of the guide tube is in the lock chamber, and then the gate valve is closed. During this operation a pair of viton O-rings separated by a floating spacer ring (all labeled sliding O-ring in Figure 4-9) provides the vacuum seal. This division of seals means that the bulk of the time (during regular probe travel) the bellows are used, but for changing the probe, when the

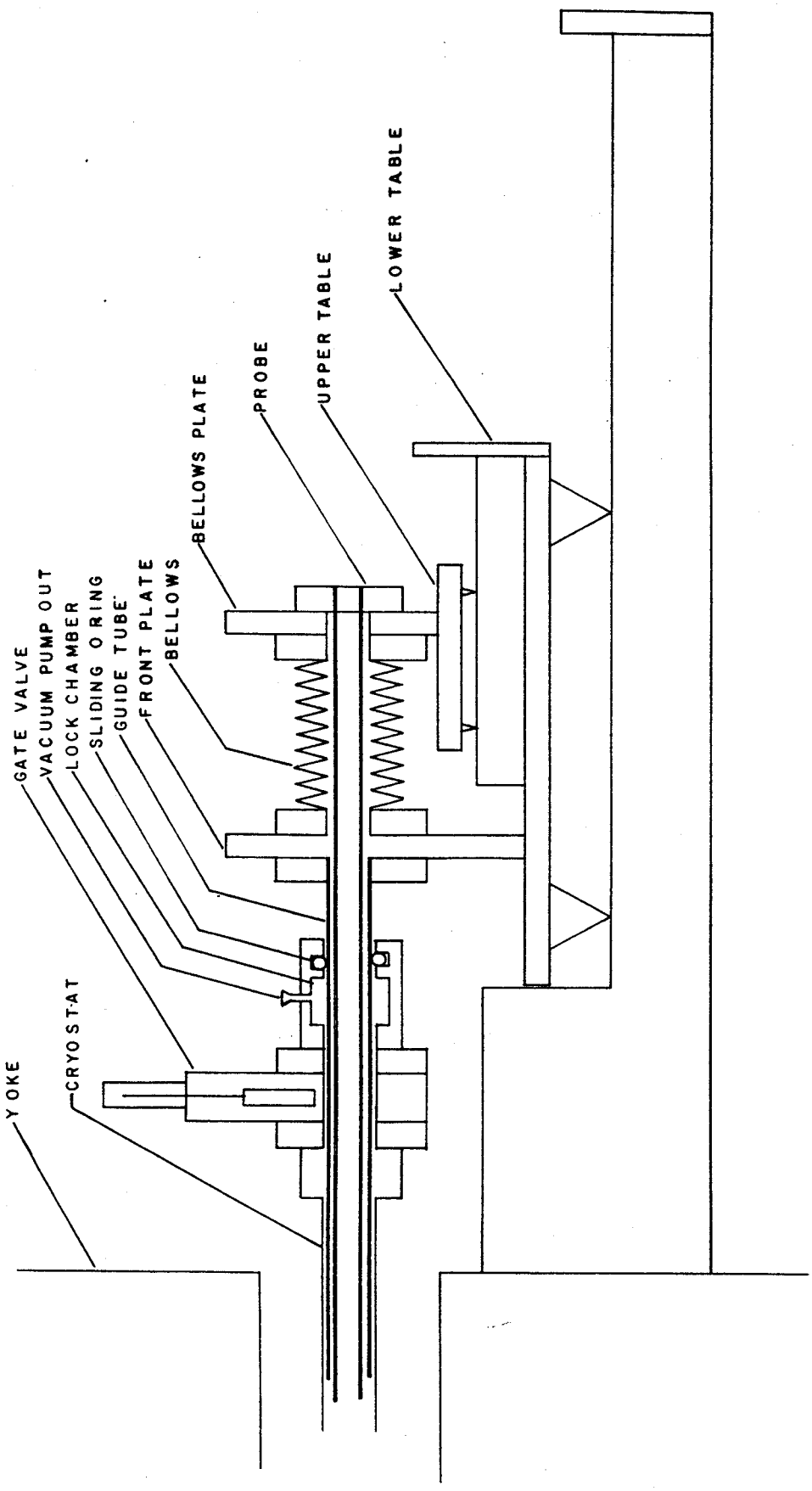

Figure 4-9 A schematic of the new viewer port probe drive showing the major components. The two separate drive systems allow for a bellows to be used in the regular range of travel and O-rings to be used for insertion and removal

travel is 40", the O-rings are used. The lower table is mounted on Thomson pillow blocks, and driven by a ball screw attached to a synchronous motor. A complete probe change can be accomplished in half an hour, making repairs and modifications relatively simple.

Another important feature of this design is the ability to accept any probe that meets the following simple requirements: that it match the bolt pattern on the plate, and that the maximum diameter from the plate inwards be 5/8". The length of the probe from the mounting flange to the tip may be anything from 45.5" to 59.325". Presently four different probes have been constructed. The first of the tested designs is shown in Figure 4-11. The object here was to provide isolated water and electrical circuits within the limited space. It also provided fairly good positioning of the tungsten jaws to ensure the correct differential lengths. Unfortunately the Kovar feed-throughs were poor thermal conductors, consequently after beam hit the probe for any length of time the temperature of the jaws rose dramatically and eventually the feed-throughs became electrical conductors. The design currently in regular use is shown in Figure 4-12. This one is the same as that orginally used with the 4" drive but with length changed. Also the jaws are now a single piece of molybdenum which

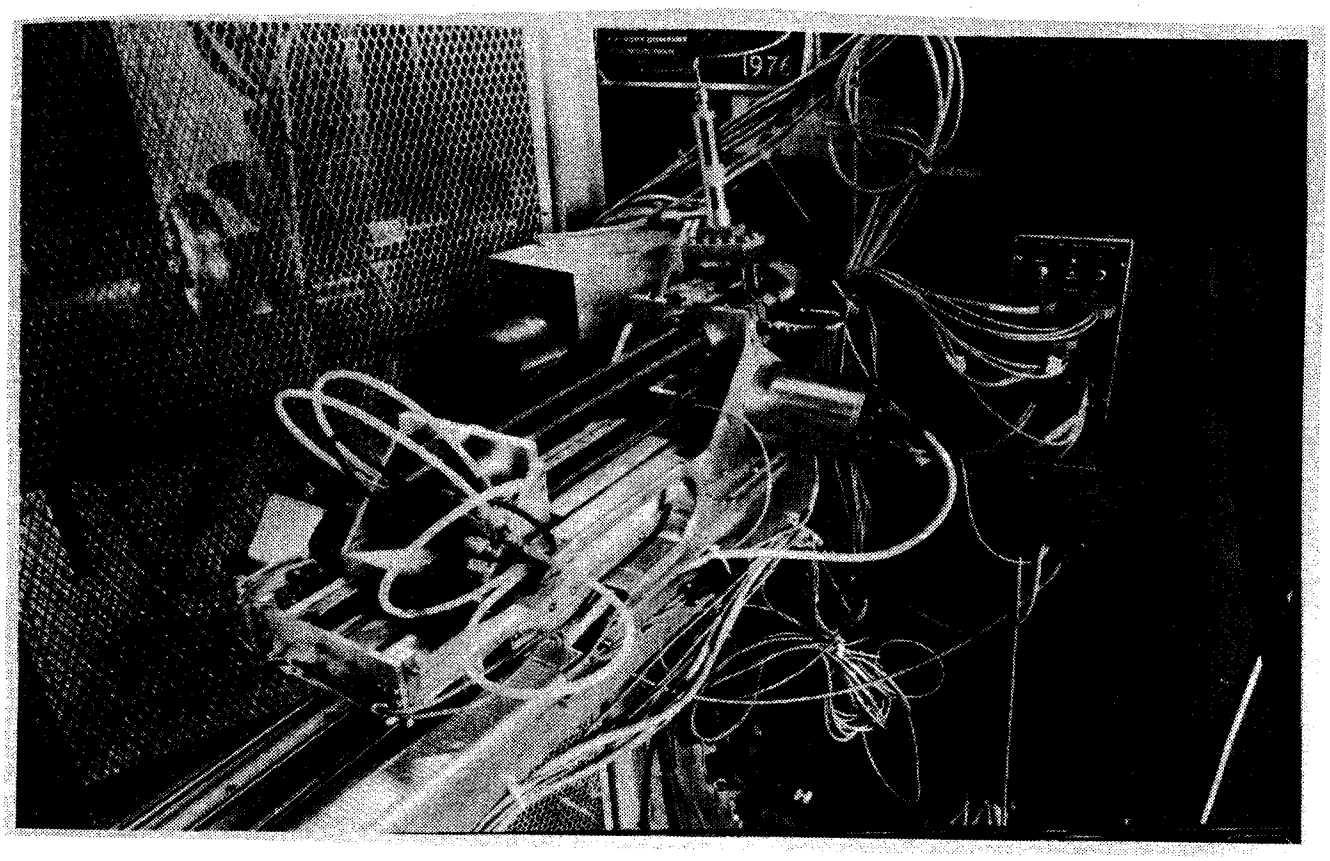

Figure 4-10. A photo of the new drive installed on the cyclotron. In this photo the drive is in the 'running' position and a probe has been installed.

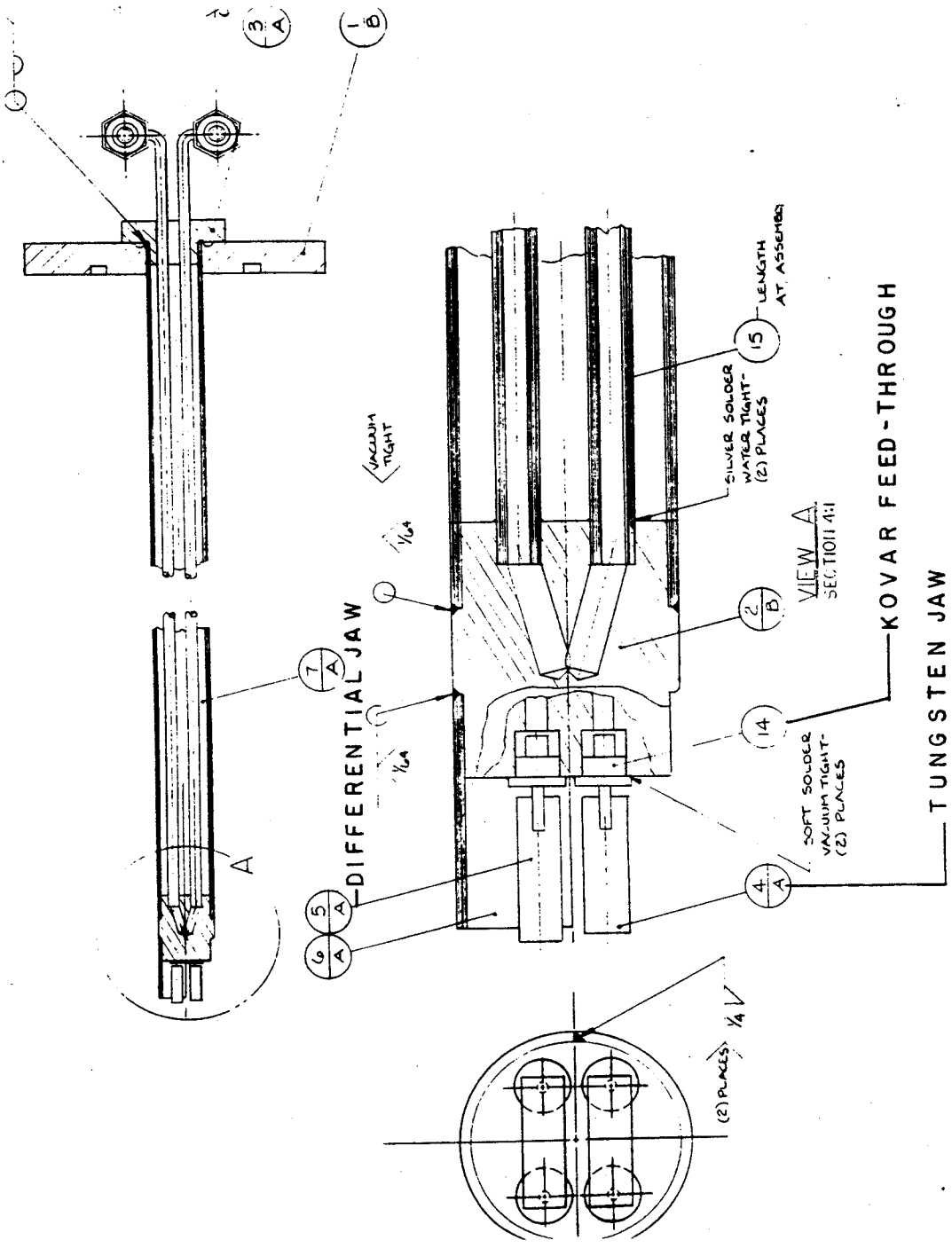

Figure 4-11. The first probe used with the new drive. The Kovar insulators were not sufficiently good thermal conductors, resulting in their becoming electrically conducting so this design was discarded.

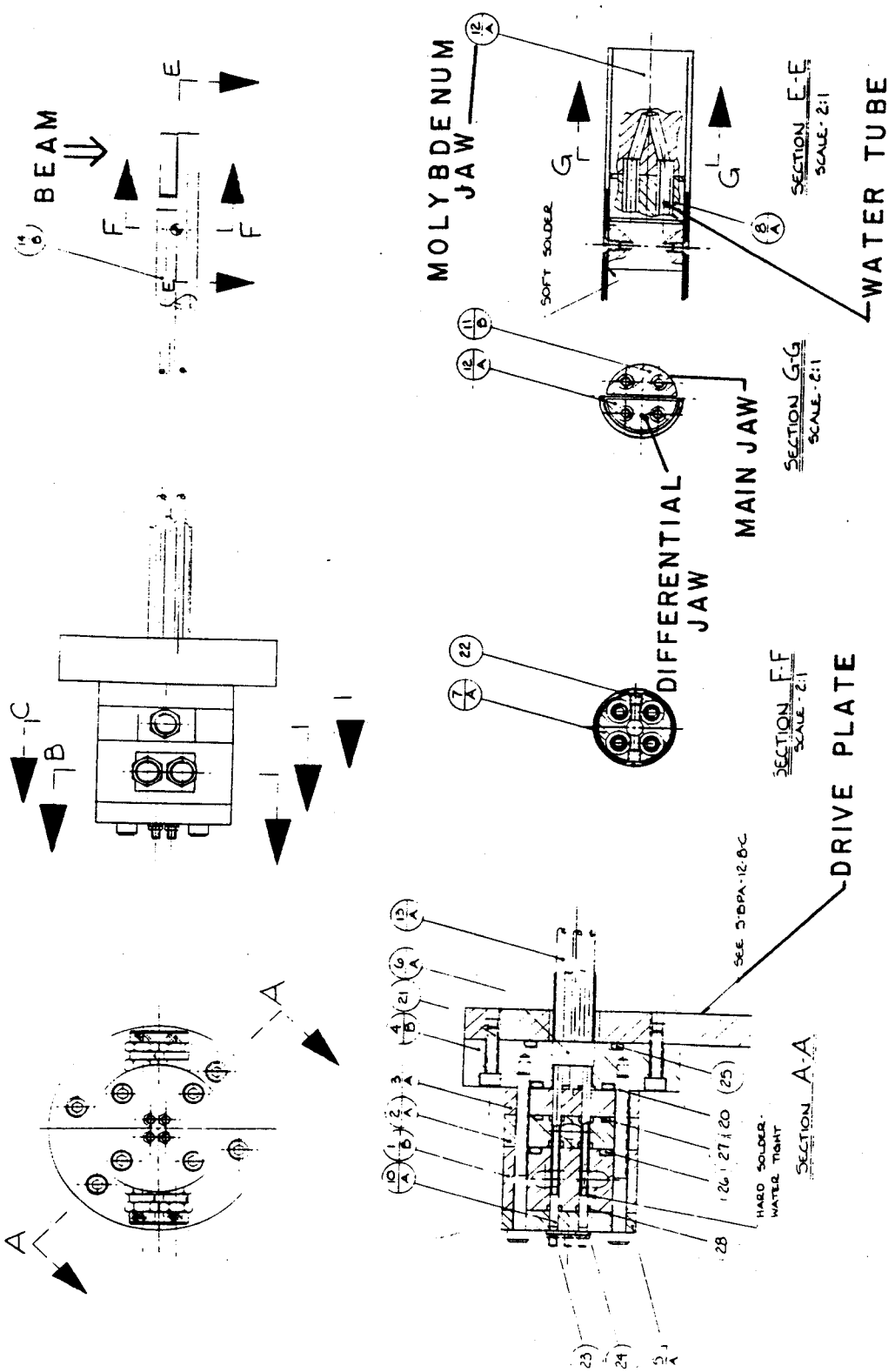

Figure 4-12. The 2 jaw differential probe currently in regular use. This design has proved to be very robust.

should improve the cooling while at the same time reducing the possibility of producing alpha emitters. One of the other probes developed is being used as the target for the radioactive beam experiments of M. Mallory et al[30].

4.5 The Gamma probe

The fourth probe, which has been constructed for use in the VP probe drive, is designed to measure the phase of the beam. This is to be done by detecting the gamma rays generated from the beam striking the probe tip with a PIN diode located just behind the probe tip. A schematic of the phase probe is shown in Figure 4-13. At the exit of the probe the signal is again amplified, and then sent to the control room. In the control room the signal is fed into a constant fraction discriminator (CFD). The output of the CFD is then used as the start signal for a time-to-amplitude conveter (TAC). The stop signal for the TAC is a pulse generated at every second positive zero crossing of the RF signal. Dividing the stop signal by two means that all the features in the time spectrum will appear twice, 360^0 apart. This then gives an immediate calibration between channels and degrees of phase, without any worry about cable length. The TAC output is digitized using a multichannel analyser

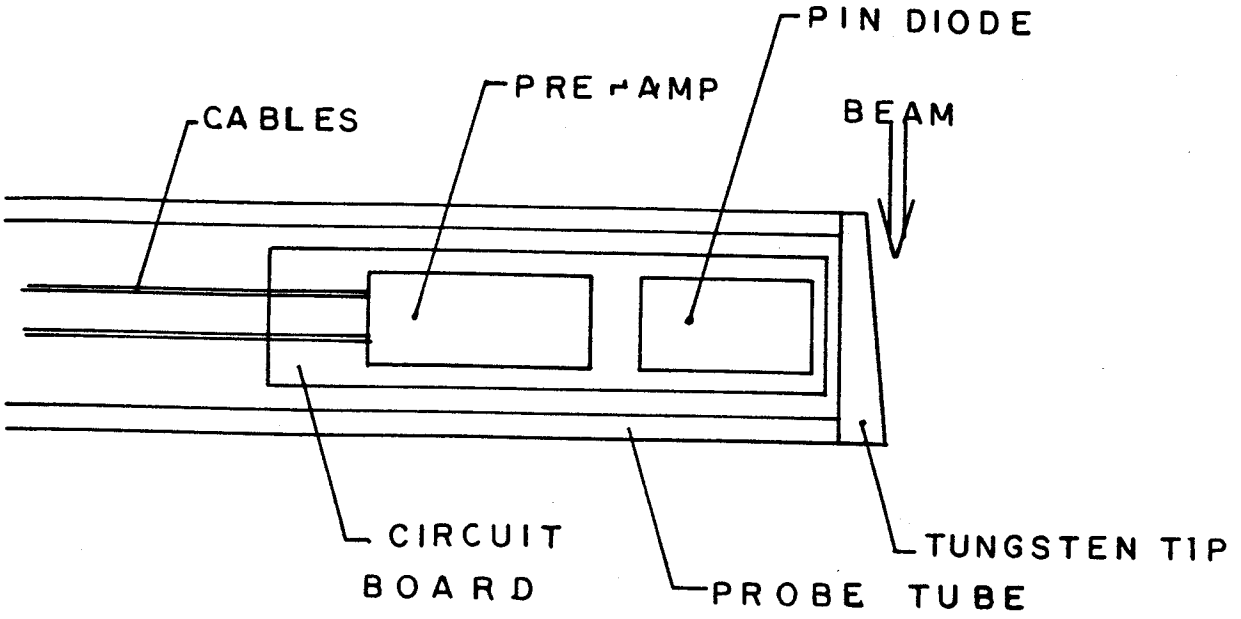

Figure 4-13. A schematic drawing of the phase probe. The PIN diode is used to detect gamma rays produced when the beam strikes the probe tip. The small size of the diode and amplifier allows it to be located near the probe tip so the count rates are high and the source is distinct from the background.

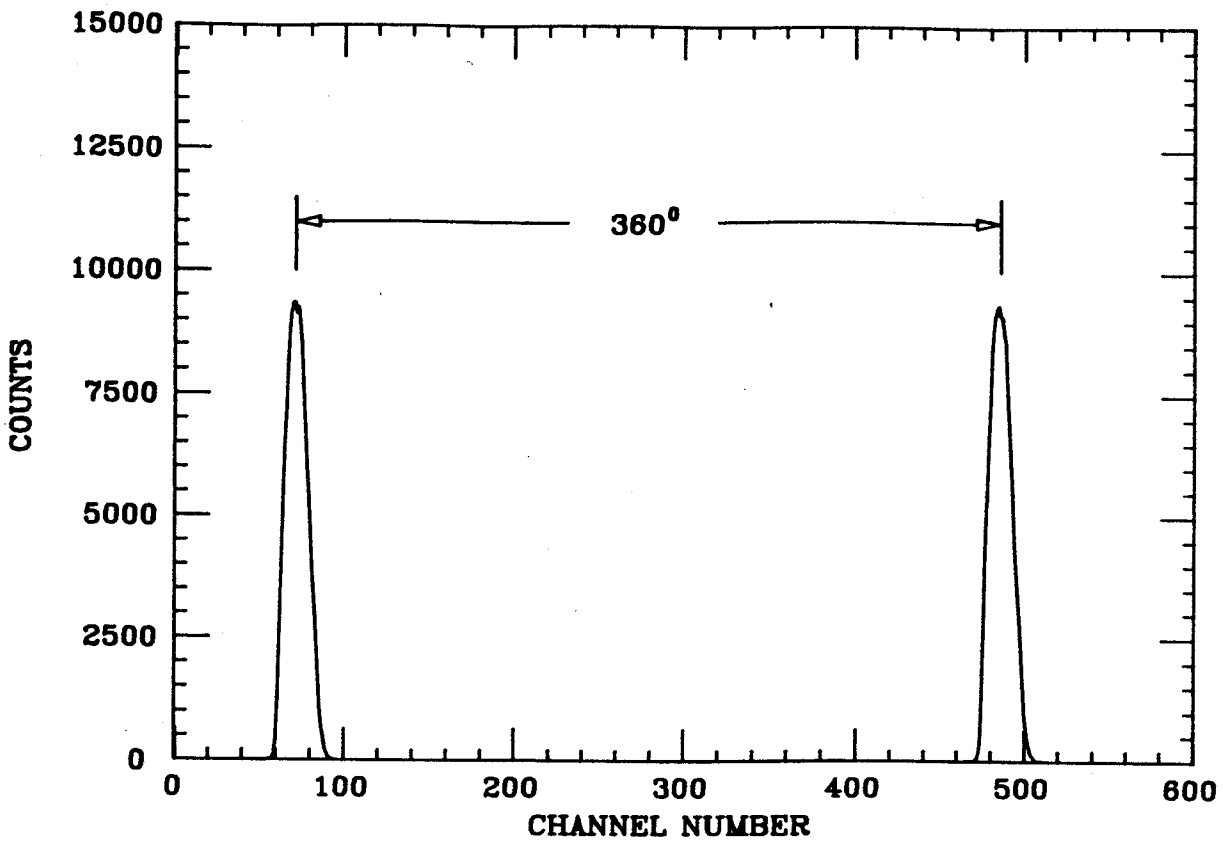

Figure 4-14. A typical spectrum of intensity versus time, as measured with the gamma probe. Notice that the divide by two of the RF stop signal causes all features to appear 360^0 apart.

for a preset length of time. A sample output is shown in Figure 4-14.

If the peak width in a spectrum, such as that in Figure 4-14, is to be attributed to the phase width of the beam, it is necessary to measure the time resolution of the PIN diode. This proved to be more difficult than expected, because the diode's small size resulted in too low a count rate for a coincidence measurement. What was done, was to measure the rise time of the diode when pulsed with a fast laser. These measurements concluded that the rise time was better than 500 ps. In Figure 4-15 the time spectrum of the external beam, as measured with the PIN diode, is compared to a measurement of the same beam made with a BaF detector. The time resolution of the BaF was known to be better than 300 ps, and the two detectors produced very similar results. Given that the gamma probe can make a reliable determination of the phase, it can be used to measure the phase width of the beam between 20" and extraction. As well it can be used to measure changes in the phase as a function of radius, but the determination of the absolute value of the phase will need to be done with a different technique, such as frequency detuning.

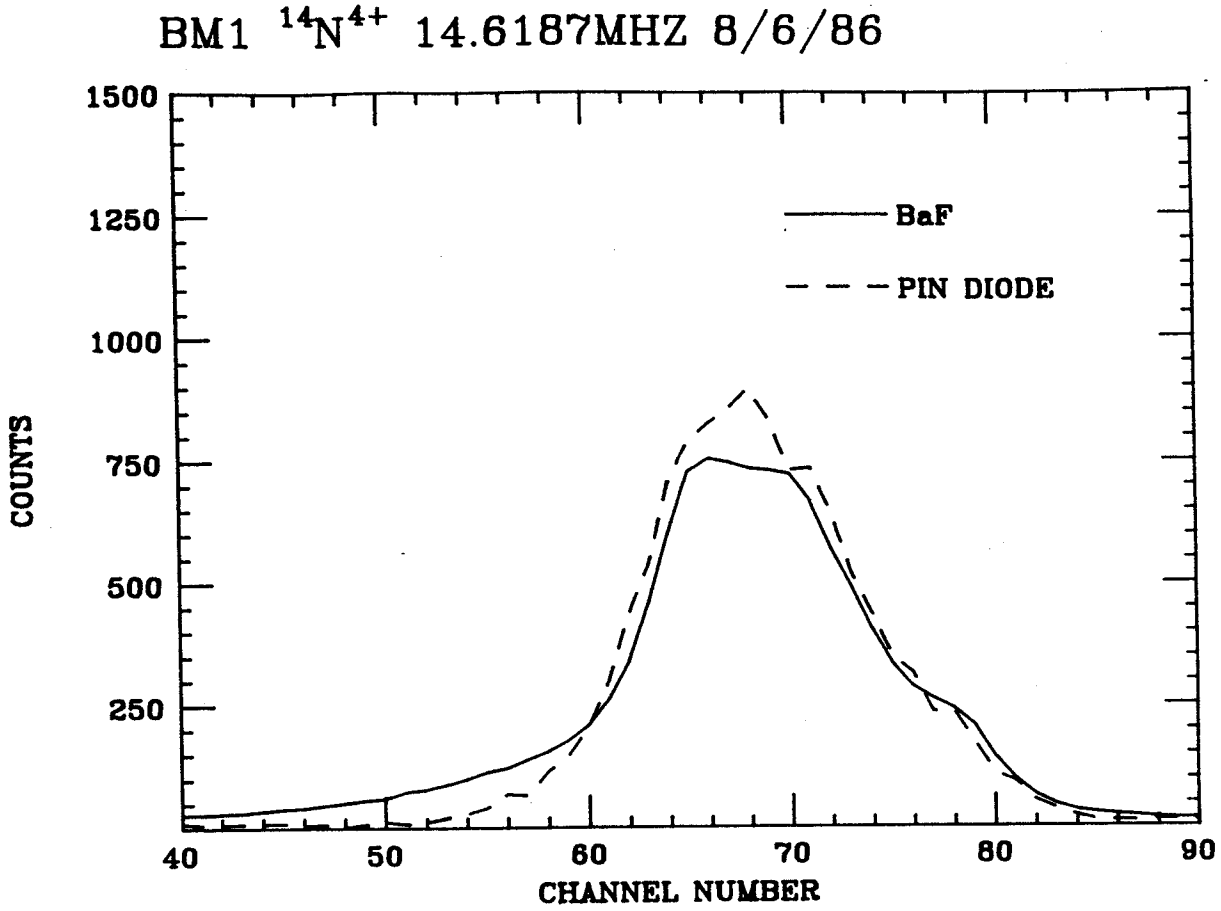

Figure 4-15. A comparision between the PIN diode and a BaF detector. Both detectors measured the same beam, which was striking beam stop 1. The measured beam widths are very similar.

5. Experimental Results

5.1 Frequency Detuning

The phase history of the beam is a very sensitive function of the magnetic field, thus an independent measure of the phase would verify the procedures used to compute the magnetic field. Several methods are available to measure the phase, but the frequency detuning method first proposed by Garren and Smith[31] is the most straightforward. The separated longitudinal equation is,

$$\sin \phi = \sin \phi_0 + \frac{2\pi h}{\delta E} \int_0^{E_f} \left(\frac{\omega_0}{\omega} - 1 \right) dE \qquad (5\text{-}1)$$

$$= \sin \phi_0 + \frac{2\pi h}{\delta E} F(E)$$

where, $F(E) = \int_0^{E_f} \left(\frac{\omega_0}{\omega} - 1 \right) dE$,

and δE is the energy gain per turn.

Since $F(E)$ depends only on the energy and not the initial value of the phase (ϕ_0), the width of the beam in $\sin \phi(E)$ is constant when equation 5-1 is valid. If the phase of any part of the beam reaches $\pm 90^0$, it decelerates inward, to

the machine center and is lost. If the central ray of the beam reaches 90^0 at a given radius this can be observed on an integrating probe as a reduction of the beam current to half amplitude at that radius.

Rewriting the longitudinal equation for a new RF frequency ω' gives,

$$\sin\phi'(E) = \sin\phi(E) + \frac{2\pi h}{\delta E} \frac{(\omega' - \omega_0)}{\omega_0} \{ F(E) + E \}, \qquad (5\text{-}2)$$

where $\phi'(E)$ is the phase obtained with the new RF frequency, and $\phi(E)$ is the phase at the operating frequency ω_0. Defining the frequencies ω_+ and ω_- as the frequencies which drive $\sin\phi$ to +1 and -1 respectively, equation 5-2 becomes,

$$+1 = \sin\phi(E) + \frac{2\pi(\omega_+ - \omega_0)}{\delta E\ \omega_0} \{ F(E) + E \}$$

$$-1 = \sin\phi(E) + \frac{2\pi(\omega_- - \omega_0)}{\delta E\ \omega_0} \{ F(E) + E \}.$$

Let $\epsilon_\pm = (\omega_\pm - \omega_0) / \omega_0$ and we find the expression for $\sin\phi$ is,

$$\sin\phi(E) = (\pm 1 - \frac{2\pi E}{\delta E} + \epsilon_\pm \sin\phi_0) / (1 + \epsilon_\pm).$$

Using this formulation instead of the more common[32],

$$\sin\phi(r) = \frac{2\omega_0 - \omega_{\pm}(r) - \omega_-(r)}{\omega_+(r) - \omega_-(r)}$$

means that the phase can be found at radii for which either ω_+ or ω_- cannot be found. The trade-off is that the energy gain per turn δE must be known.

Ideally, determination of the phase using this method requires only that the machine parameters (RF voltage, magnetic field etc.) are stable in time. In practice however there are several limitations. First of all the centering of the beam affects the results by shifting the radius at which the half intensity is observed. As is well known it is not possible to center the beam at all radii at once[33], so usually the best centering is reserved for the large radii where the turn density is greatest. In the K500 even this is not possible, because, in order to minimize beam losses during the resonance crossings at the outer radii, it is necessary to run with the beam off center for most of the machine[34]. Another difficulty arises because the main probe in the K500 is a complicated set of train cars that travel on a spiral shaped track located on the center of one of the hills (see Figure 1-1). Because of its complex nature, determining the exact location of the probe is difficult, so the position read out can be wrong in some places by as much

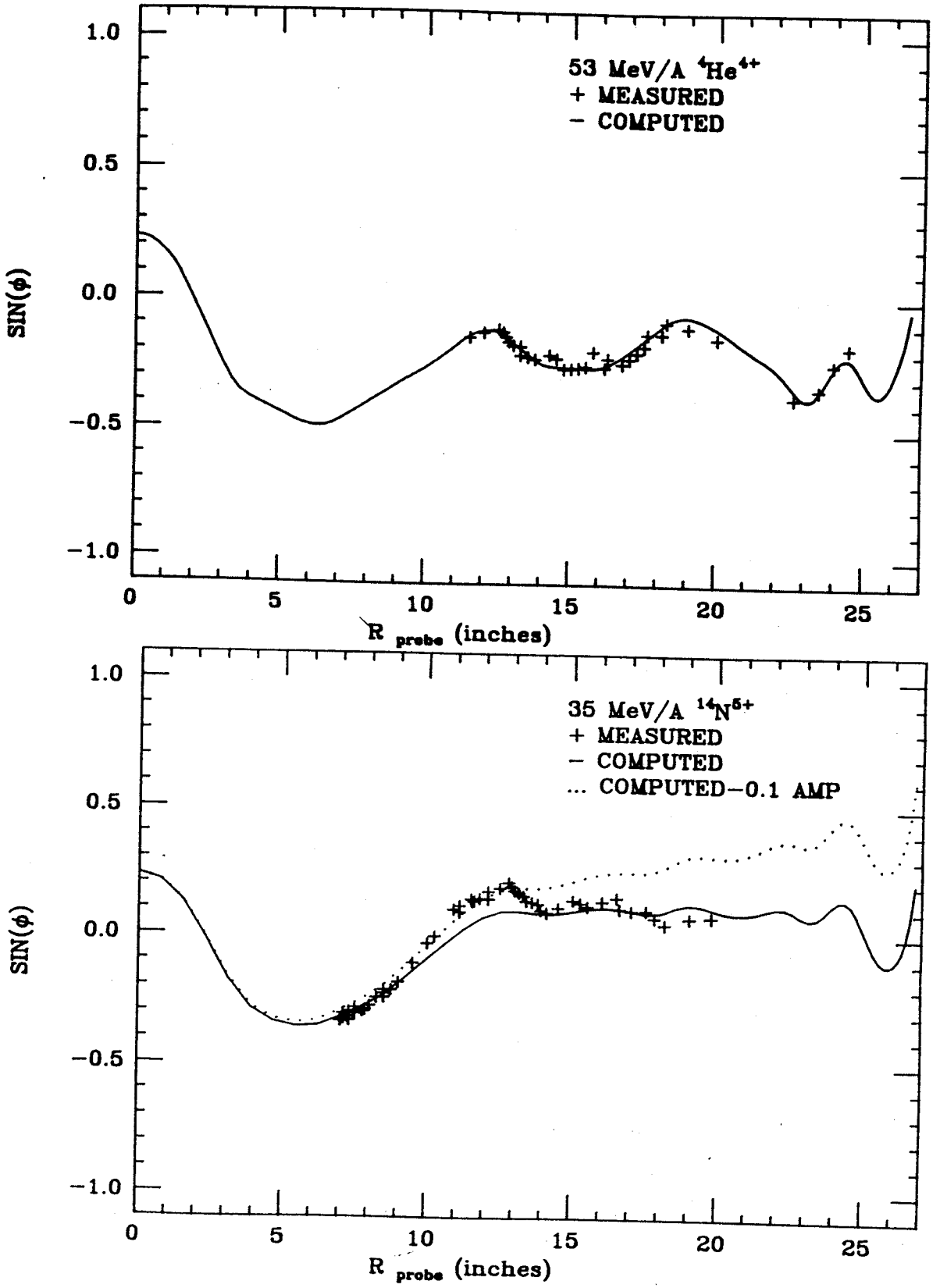

Figure 5-1. The calculated and measured phase curves for two different magnetic fields. The dashed curve for the N^{5+} case is the calculated phase curve when the mail coil currents are changed by 0.1 Amps.

as 0.5". If the phase curve changes rapidly, as it does at large radii, the frequency required to drive the phase to 90^0 becomes a constant. For example in Figure 5-1b the ω for radii larger than 26.0" will be a constant because the current will always be lost at 25.0"

In Figure 5-1 the results of measurements in two separate magnetic fields is shown. The agreement in both cases is quite good, except for a sharp bump in the N^{5+} case. Either this discrepancy is caused by a probe calibration error or it is a result of a change in the main field. During this particular run the main coils currents drifted by as much as 0.1 amperes, as the lead temperatures changed. Unfortunately the problem was not detected until late in the run so there is no way of determining when it happened. Since the data was taken in sequence it is possible that the bulk of the excursion took place as data between 14" and 12" were being collected. The dotted curve in the figure is the phase curve if the coil currents are reduced by 0.1 Amps.

5.2 Phase Selection

The previous chapters have discussed the phase selection hardware and how it is intended to achieve its

goals. In this section experimental results of a test run of the phase slits will be presented. As described in 3.2 the coarse selection is done with a slit located on the dummy dee between the puller and the second dee ("C" dee). The only way the aperture of this slit can be changed is to raise the cap, which is a one day job. As a result it is difficult to compare directly beam conditions with and without the small slit. In Figure 5-2 the output from the gamma probe, collected when the coarse selection slit was in place, is shown. This can be compared with the computed results in Figure 5-3. The computation was done by tracking particles through the axial injection system and around the first turn in the cyclotron. The initial beam filled the available aperture and any particle which hit either the inflector (including the collimator) or a dee post was removed from the beam. This calculation predicts that the phase width after the first turn would go from 43^0 to 14^0 (FWHM) when the narrow slit is installed. This is in excellent agreement with the γ-probe measurement done at extraction radius (Figure 5-2), that gave a result of 14.8^0. Figure 5-4 is shown for reference. It gives the results of a calculation similar to that shown in Figure 5-3, but with the collimator aperture reduced to 1mm. With a 1 mm collimator the starting emittance is reduced to 25π mm-mrad

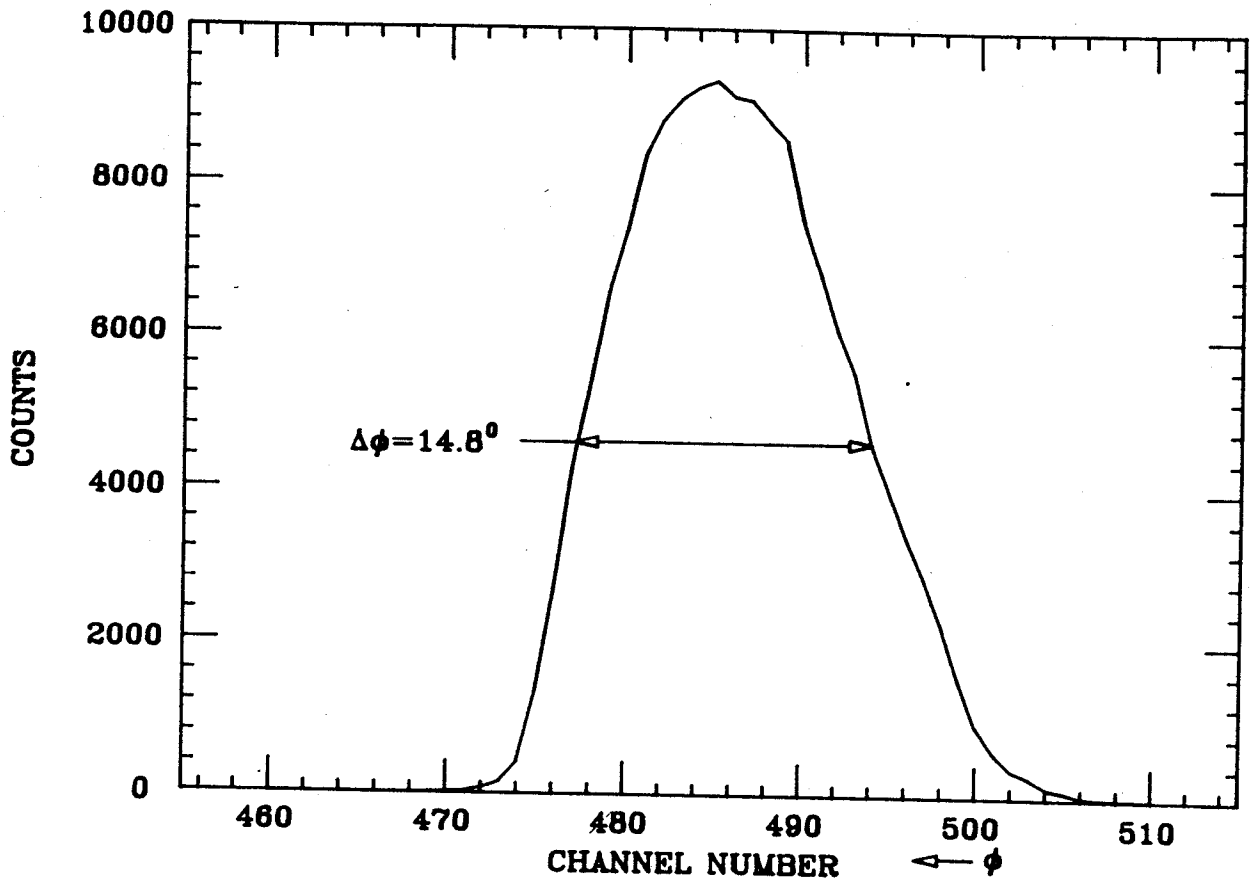

Figure 5-2. The phase width of the internal beam as measured with the gamma probe at extraction radius when the narrow first turn slit is installed

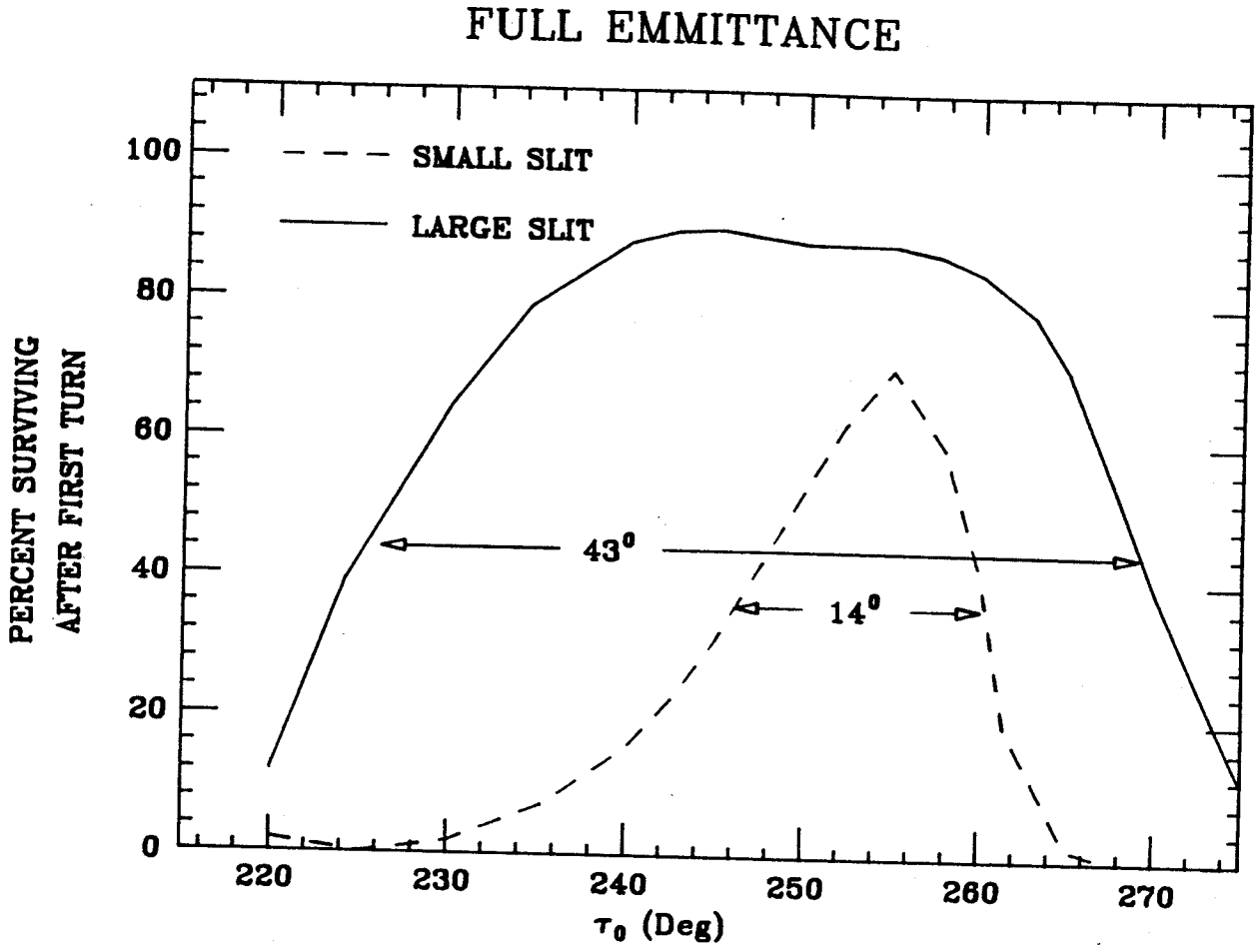

Figure 5-3. A calculation of the percent beam which survives the first turn in the cyclotron for the wide and narrow first turn slits. The inflector collimator is 4 mm in diameter.

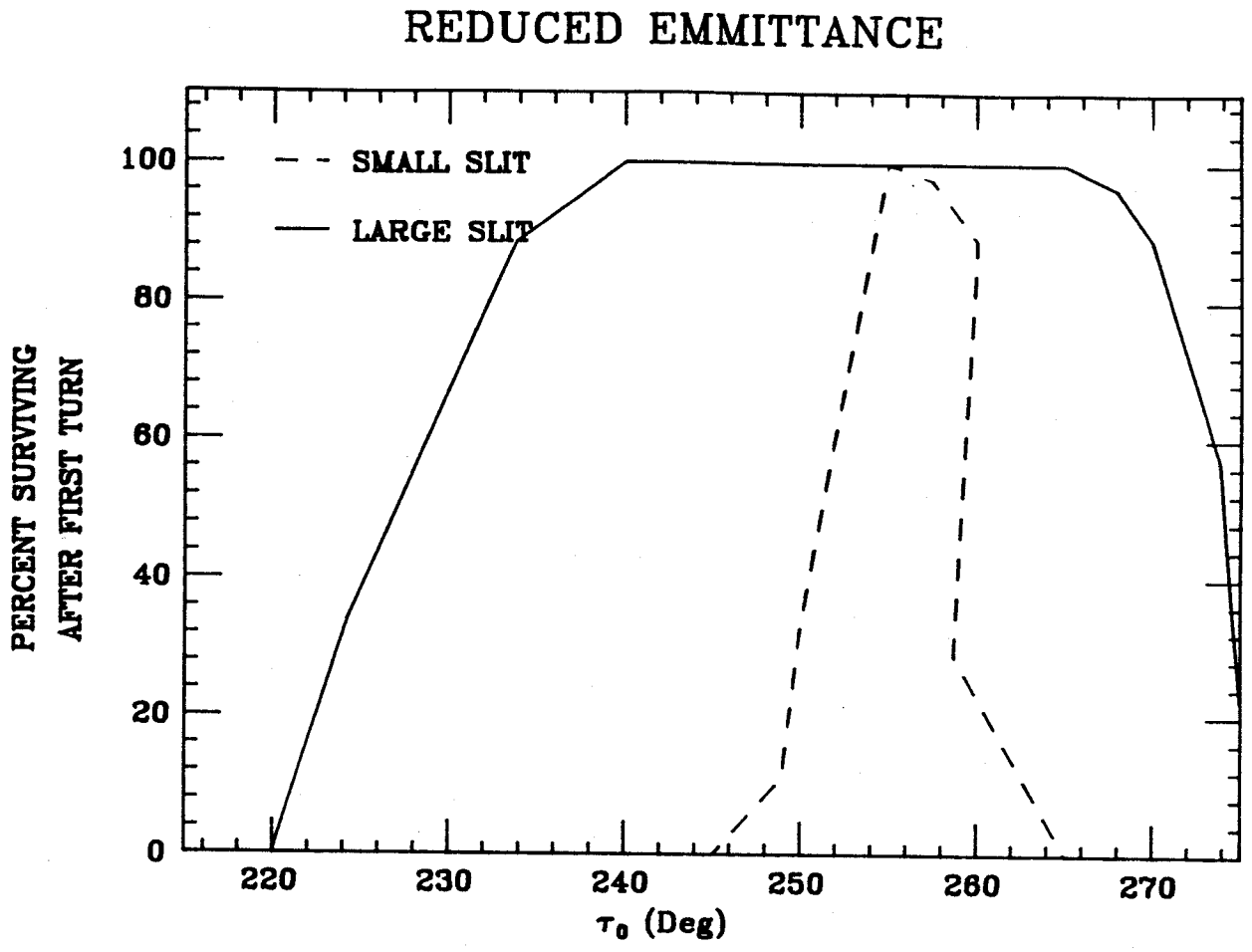

Figure 5-4. A calculation of the percent beam which survives the first turn in the cyclotron for the wide and narrow first turn slits. The inflector collimator is 1 mm in diameter.

as was discussed in section 3.3. At the time of the test run (when the first turn slit was installed) there was an alignment difficulty with the spiral inflector and so it was not possible to run the reduced emittance case, but in the future it may be possible to do so.

With the coarse selection in place the differential traces (Figure 5-5) showed a much more pronounced turn pattern than usual. The large periodic structure is a result of a coherent oscillation. In Figure 5-6 the computer program SOMA has been used to estimate what a probe plot would be like, given the calculated orbits. For this case it was assumed that the phase width was 14^0 and the starting conditions were an eigen-ellipse. The area of the ellipse was chosen to be 100π at the inflector entrance, and the center of the ellipse was located using the prescription of Figure 2-3. The computed and measured turn patterns are similar in all aspects; 1) the turn spacing is the same, indicating that the energy gain per turn is close to the calculated value, 2) the space between turns is reduced in the same regions, 3) the region of bunched turns due to the coherent oscillations occur at similar radii. The last point indicates that most of the centering error is induced by the central region (in the calculation the centering error is built into the initial conditions), since the field used in

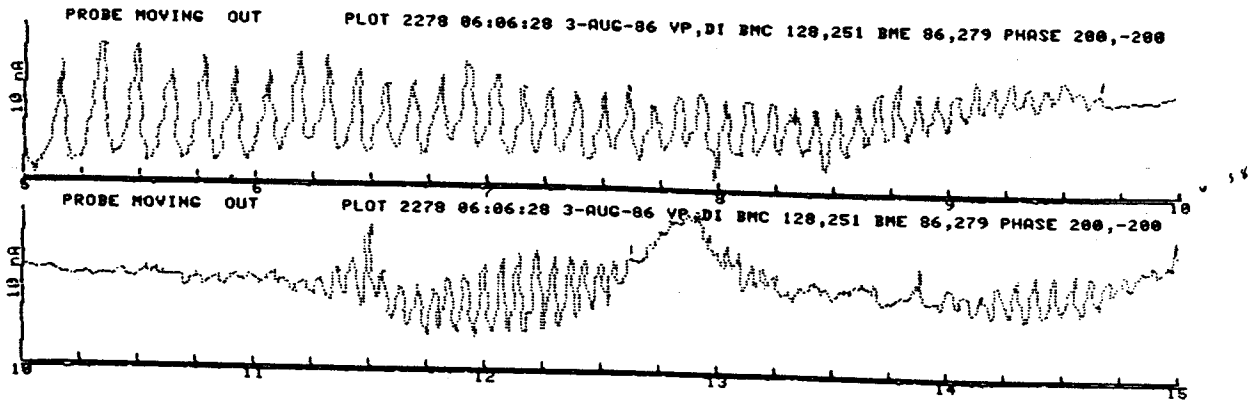

Figure 5-5. A differential probe trace, taken with the narrow first turn slit in place. The cyclotron was tuned for good extraction.

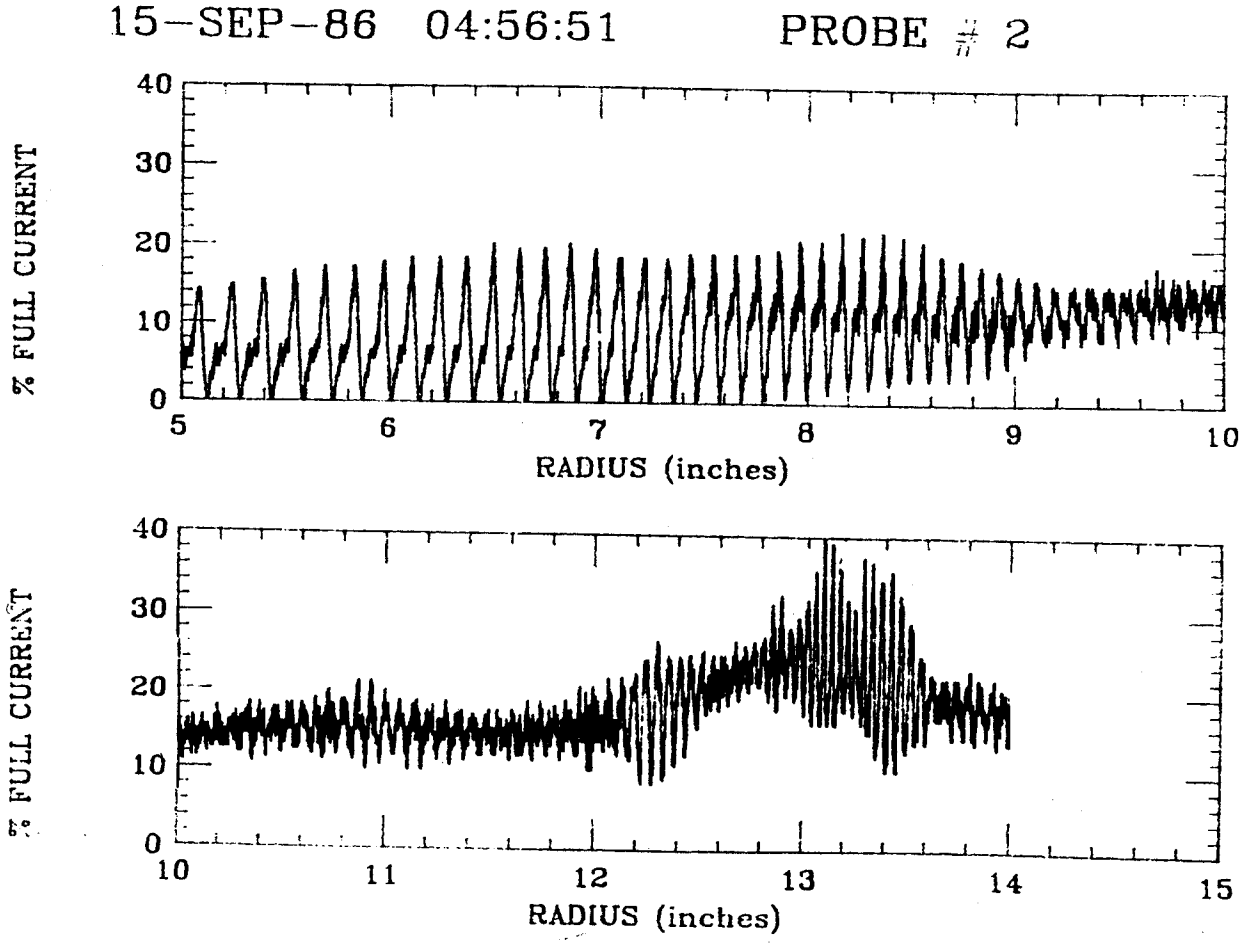

Figure 5-6. A differential probe trace, calculated with the program SOMA. Note the similarities in structure to the actual probe trace of the previous figure.

the computations does not contain the imperfection harmonics. Attempts to center the beam with the center bump usually result in large beam losses, probably from the reduced stability region which results when the bump coil is not cancelling the first harmonic at $\nu_r = 1$.

As described in section 3.4 the fine selection is accomplished with a pair of tungsten posts whose positions are adjustable. If proper selection is to take place, one must find the locations at which the posts lie between turns. Figure 5-7 shows the measured and calculated current distributions at the upper post azimuth. The arrows in the figure show optimal post locations. The computations were done with the program SOMA, using the differential probe option with the probe width equal to the post thickness. The measured points were obtained by placing the main probe at ±10." and recording the current as a function of slit position. Since the only possible loss mechanism is the post, the current lost must be the current hitting the post. The values for the lower slit are shown in Figure 5-8. The reduced amplitude variation at this location is caused by the increased turn width at this azimuth. The plots of Figure 3-10 show that at the lower slit position ($\theta=204^0$) the radius changes much more rapidly with phase. than at

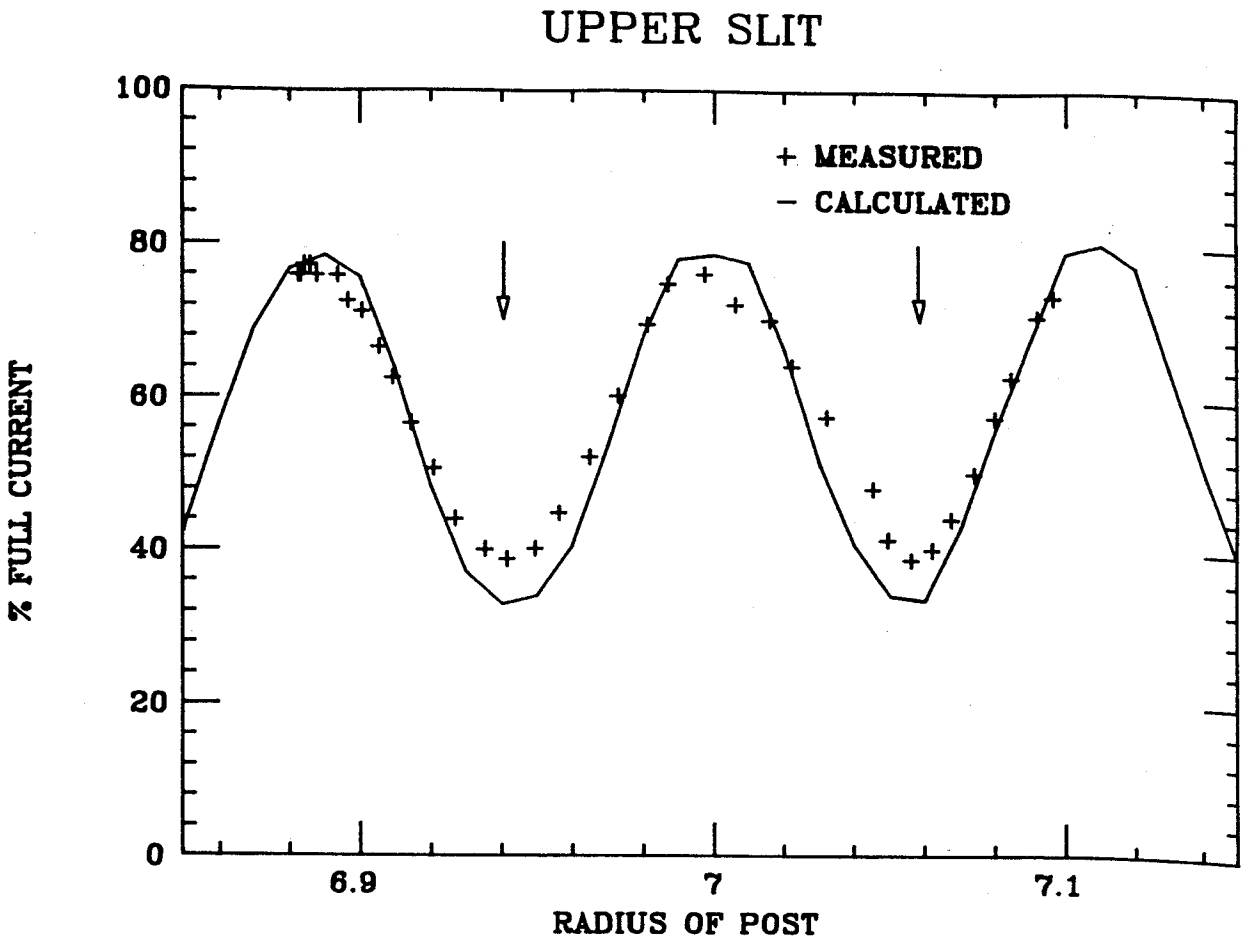

Figure 5-7. The current intercepted by the upper slit as a function of its radial position. The calculation values were obtained with the code SOMA.

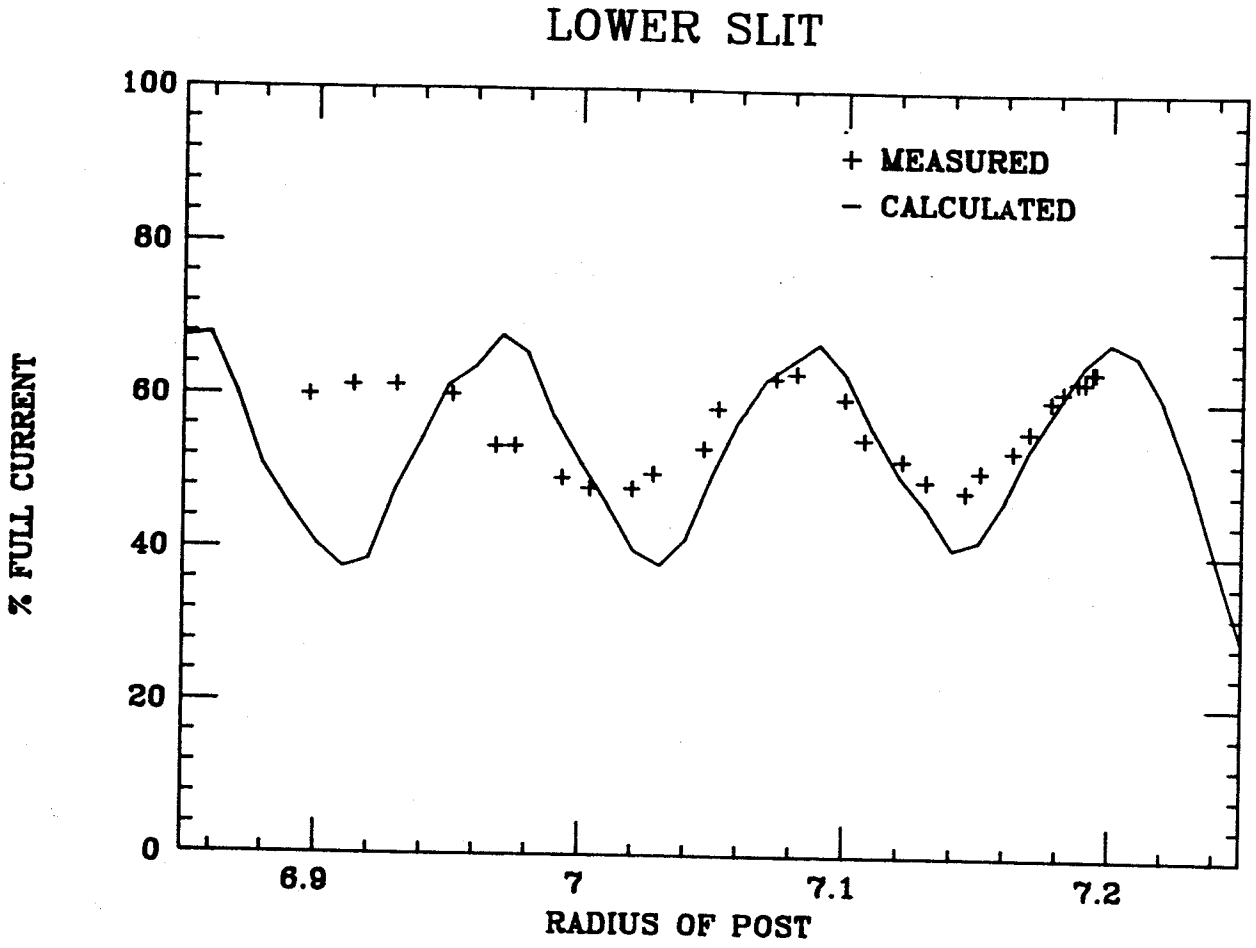

Figure 5-8. The current intercepted by the lower slit as a function of its radial position. The calculation values were obtained with the code SOMA. The poor agreement at lower radii is due to an encoder mal function.

$\theta=84^0$, and so the turns are more smeared. The poor agreement between measured and calculated results for the lower mechanism at smaller radii is a result of an encoder error (later measurements indicated the device is non-linear).

Another method of determining the optimum location for the posts is to look at the gamma probe data. The γ-probe output for two different positions of the upper slit is shown in Figure 5-9. With the upper slit at 71 (arbitrary display unit) the beam is being split by the post. As the post is moved to 125, more of the earlier phases survive the post and some of the later ones are removed. When the upper post is in position 125 the beam is being scraped from the outside of one turn and the inside of the next turn as it should.

The phase width with the upper slit at 125 is compared to no slits in Figure 5-10. With the post at this location the FWHM was 5.2^0. The same procedure was then followed for the lower slit. The reduced turn separation at $\theta=204$ (lower slit) made placing this slit a more difficult task, but it could be used to reduce the shoulders on the peak in Figure 5-10, as can be seen in Figure 5-11. The phase width with both slits inserted was 4.2^0 (FWHM). Table 5-1 compares the beam current on beam stop 0 (after extraction) with and without the slits Re-examing the calculations of chapter 3

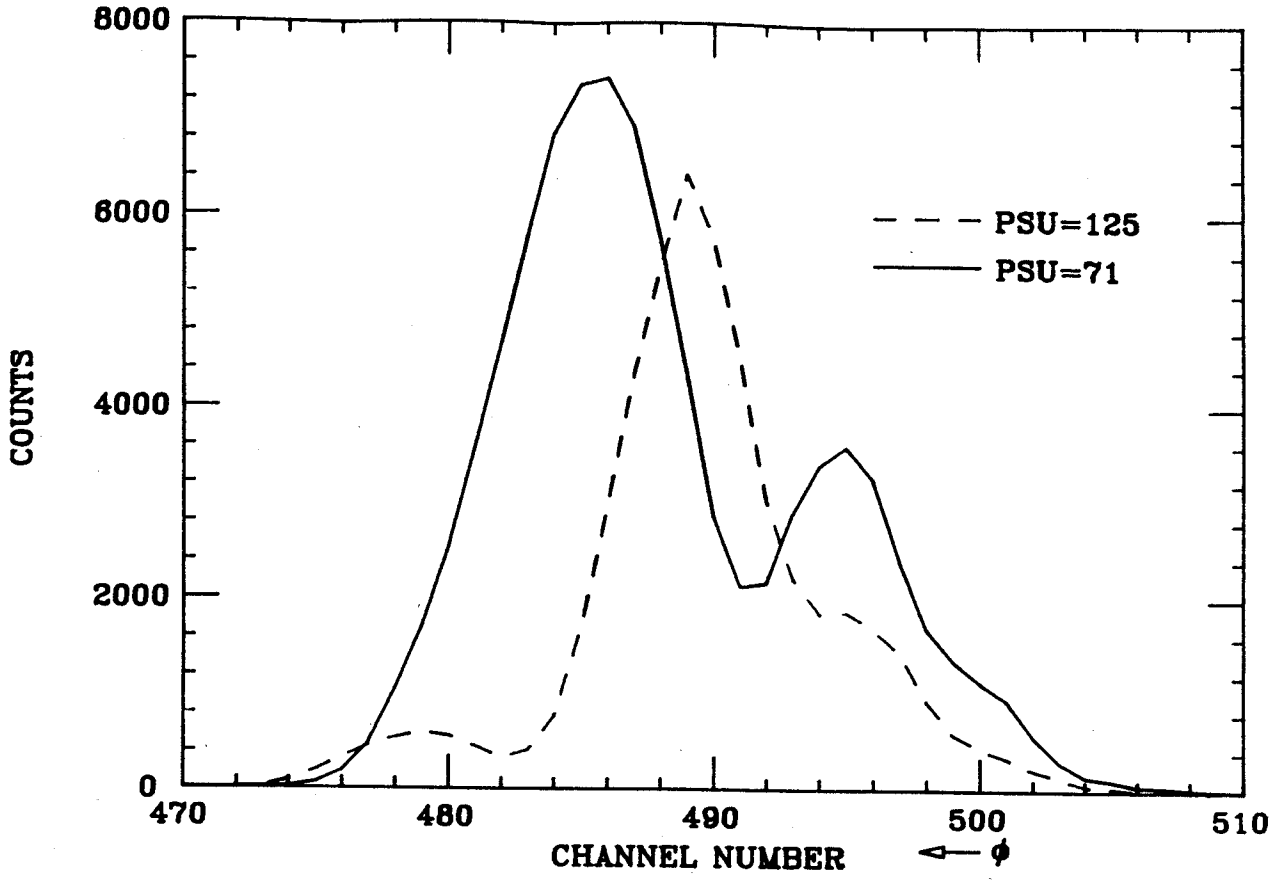

Figure 5-9 The phase width as measured with the gamma probe, for two different postions of the upper slit.

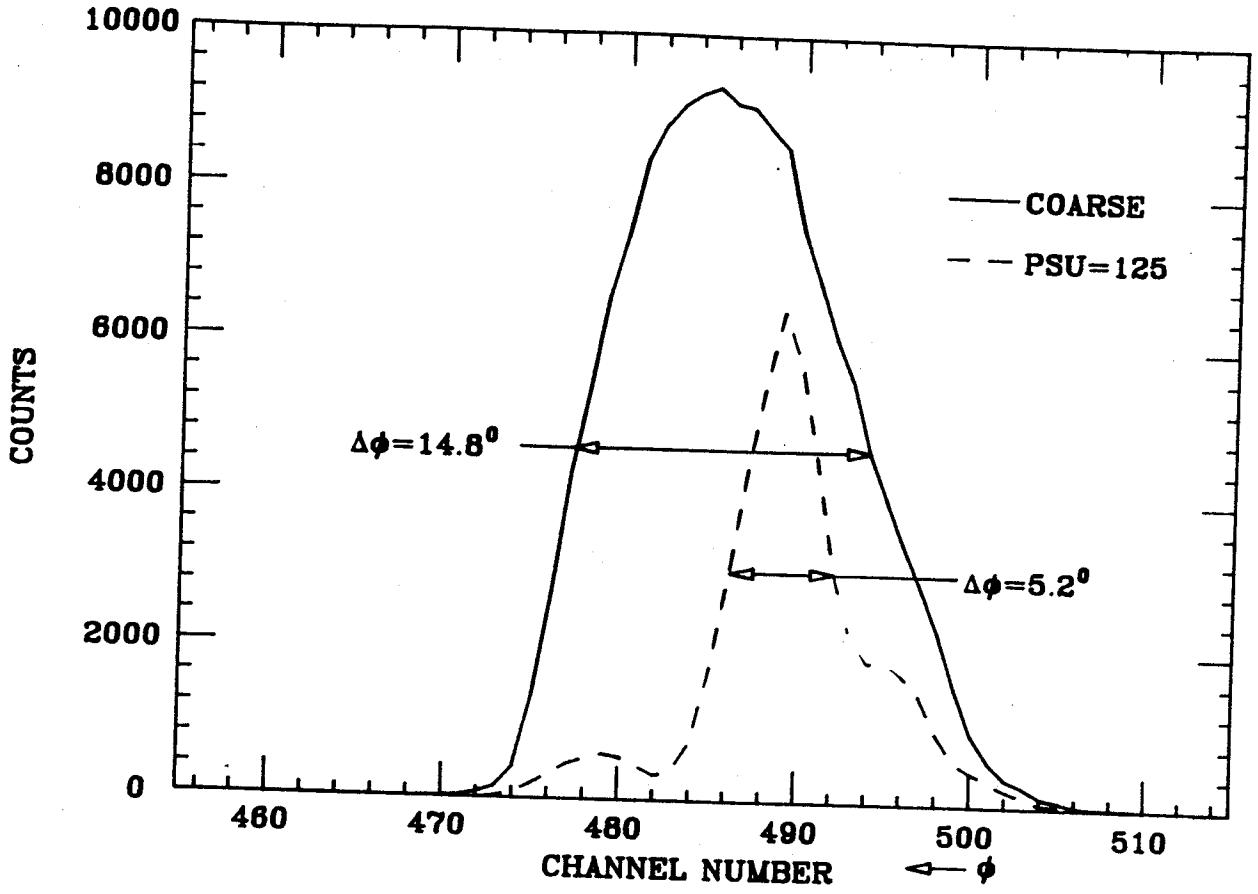

Figure 5-10. A comparision of the phase width at extraction with and without the upper slit. In both cases the narrow first turn slit is present.

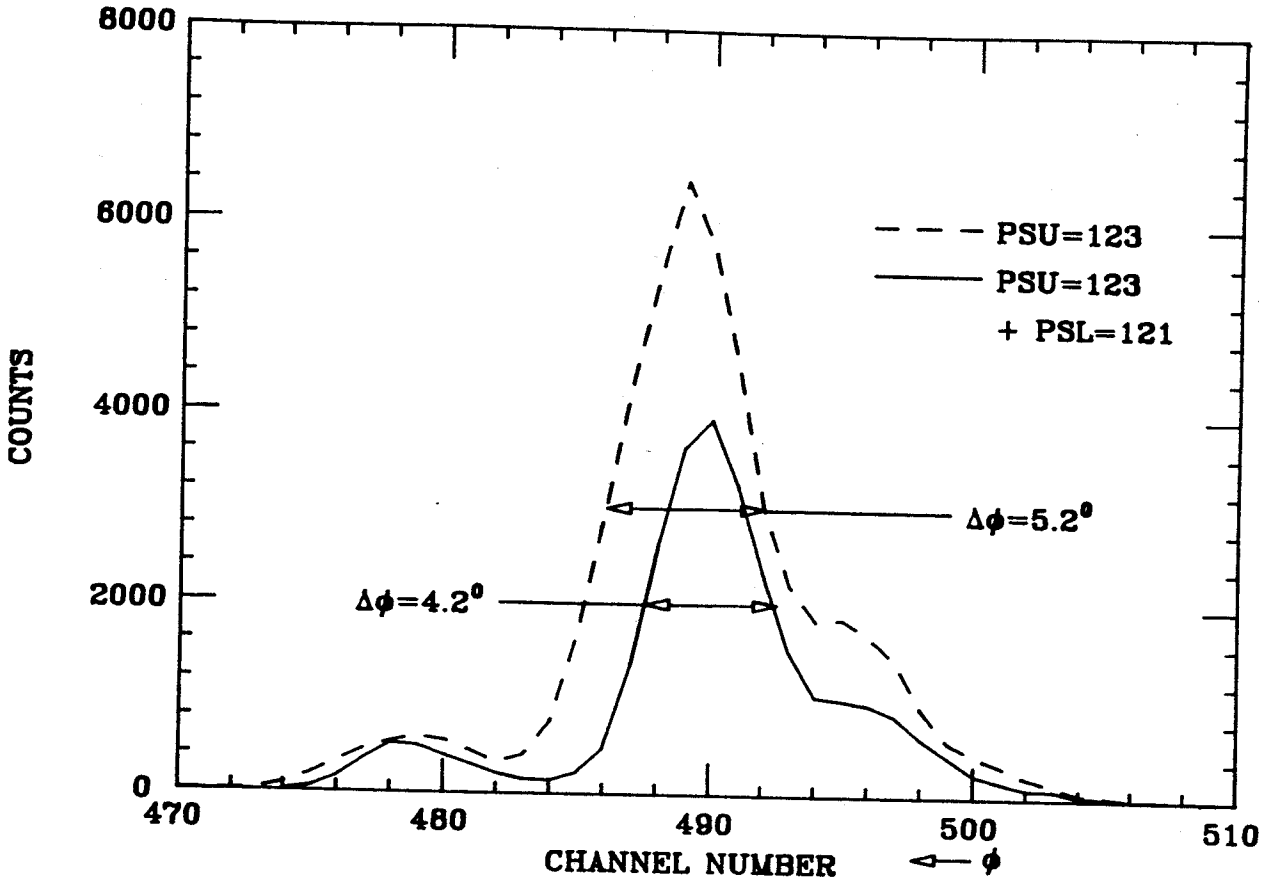

Figure 5-11. The phase widths at extraction with one slit inserted, and the combination of two slits. The extracted current is reduced by a factor of two when the second slits is inserted.

it would appear that if the lower post had a smaller diameter, the phase width could remain the same but the amount of beam surviving both posts would increase.

In Figure 5-9 the main peak is accompanied by tails on either side and this substantially increases the full width of the peak. As may be noticed these tails were not predicted by the computations shown in chapter 3. During the experiment the initial emittance was 100π mm-mrad, while the calculations assumed a starting emittance of 25π mm-mrad. To see if this increase in emittance could account for the tails a SOMA calculation was preformed. The calculation began at turn 8 with a phase width of 20^0 and an emittance of 26.5 mm-mrad. As seen in Figure 5-3, when 100π mm-mrad is run with the small first turn slit, the slit also acts to eliminate some of the horizontal emittance. To simulate this effect the dashed curve in Figure 5-3 was used as a weighting factor for the different starting times. Figure 5-12 compares the result of weighting the SOMA output to the measured phase width. As can be seen the weighting results in a very close agreement with the experimental data. Again using this weighting procedure the calculation was preformed with the upper slit in two different locations. These results are presented in Figure 5-13. In both cases the calculations predict the locations and relative heights

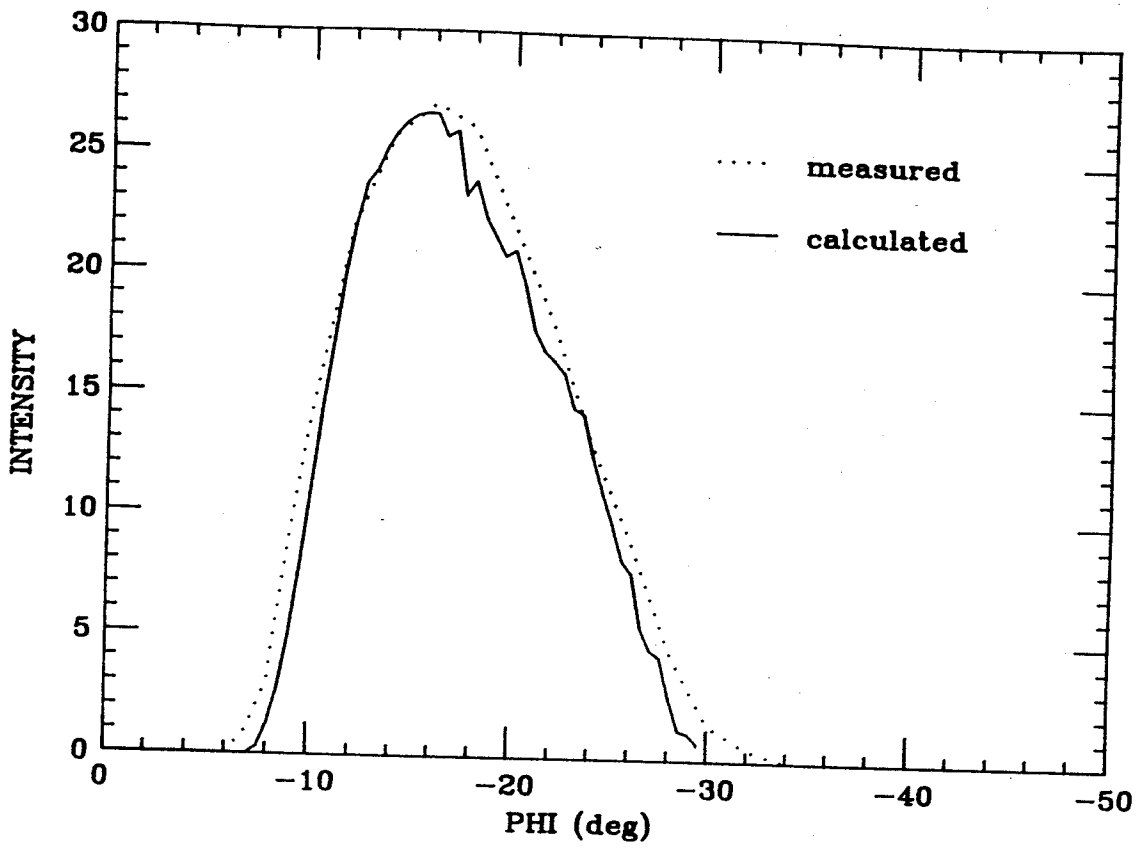

Figure 5-12. The weighted SOMA calculation is compared with the measurements. Only the first turn slit is in the machine.

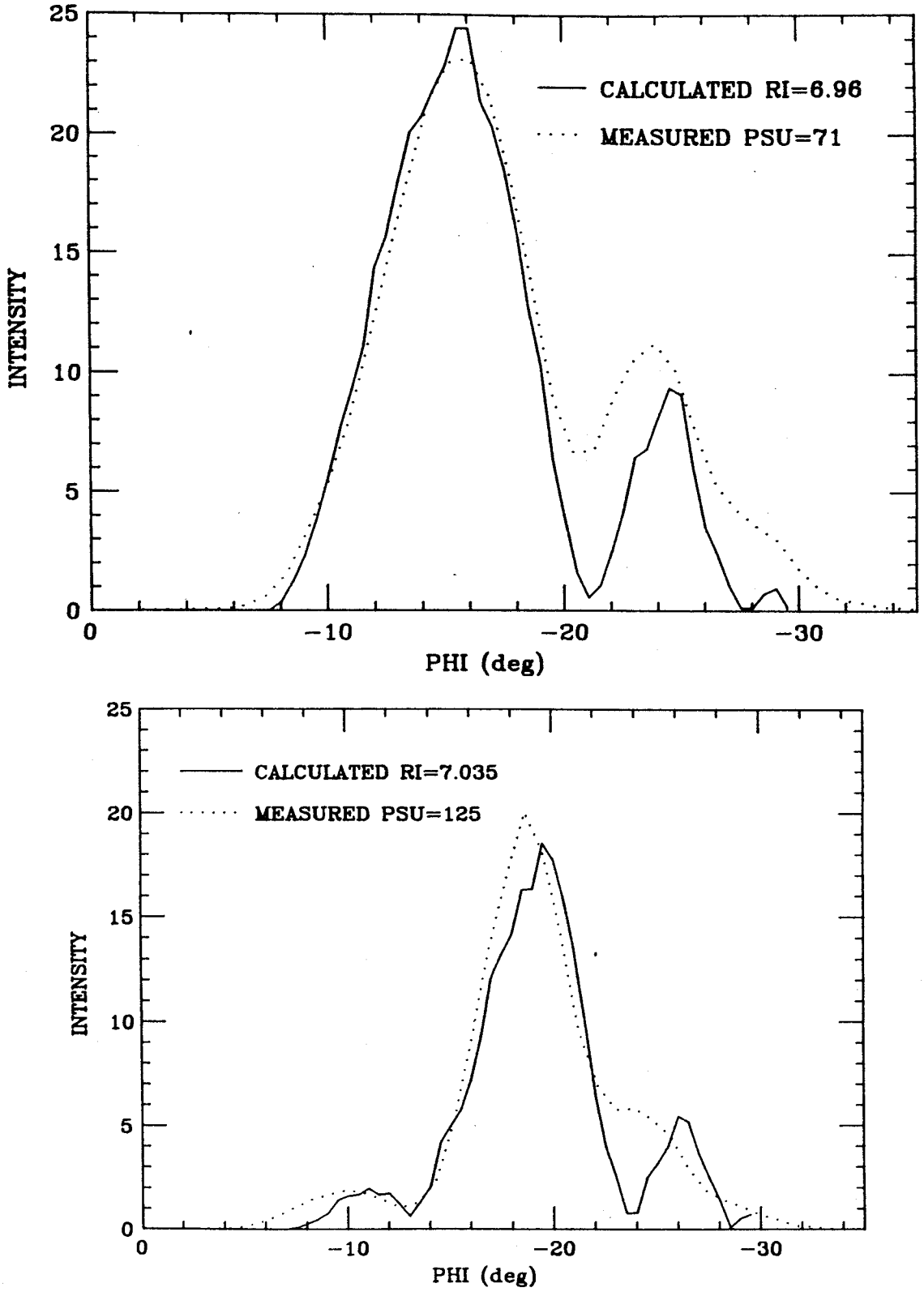

Figure 5-13. The weighted SOMA calculations are compared to the mesasurements for two different locations of the upper slit. Note the relative intensities of the peaks. These calculations assumed 100π mm-mrad initial emittance

of the peaks. The one difference between measurements and calculations is that the calculations tend to go to zero between peaks. There are several possible explanations for this. One possiblity is that because the detector was located at extraction radius, while the calculations end at 7.3" there has been some smearing in between. Another possibility is that the various starting conditions such as the initial emittance are not correct. It is also possible that unbalanced dee voltages changed the centering and so the the turn separation at the slit has changed slightly. Nevertheless the similarity suggests that reducing the emittance will remove the tails.

Table 5-1 The phase width and the extracted beam current at beam stop 0 for different combinations of slits.

SLITS	PHASE WIDTH	CURRENT AT BS0
Coarse only	14.8^0	46 nA
Upper at 125	5.2^0	20 nA
Lower at 121		20 nA
PSU=125, PSL=125	4.2^0	10 nA

The calculations shown in Figure 3-10 suggest that the phase widths should be 7.5^0 (FW) for the upper slit alone and 4.5^0 when both the posts are inserted, which is in good agreement with the 5.2^0 and 4.2 obtained experimentally.

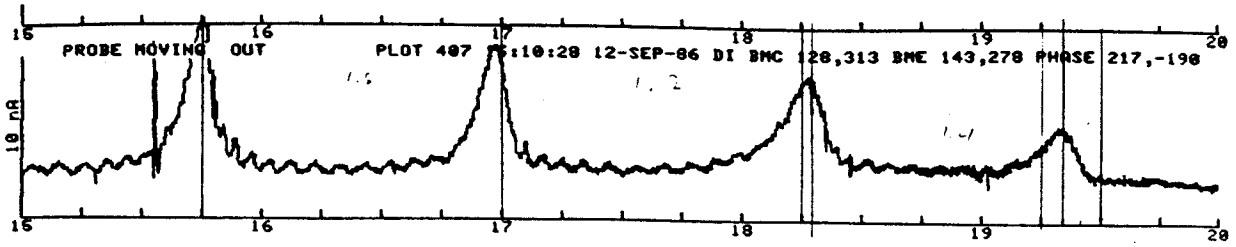

Figure 5-14. A differential probe trace taken during a $^{22}N^{8+}$ 35 MeV/A run. The wide first turn slit is installed. The radial focussing frequency can be determined from the coherent oscillation which is visible as the large amplitude oscillations.

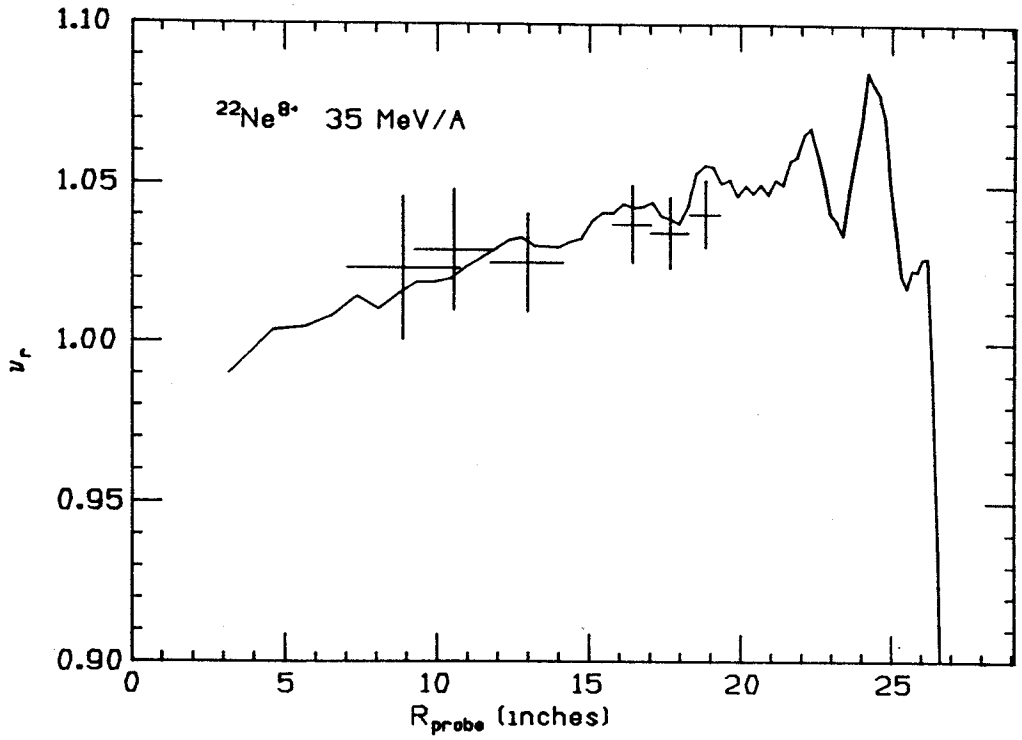

Figure 5-15. The radial focusing frequency as calculated with the equilibrium orbit code, and the values obtained from differential probe traces. The horizontal bars indicate the region over which the value of ν_r was averaged. The vertical bars indicate the possible error in determining the number of turns in a precession cycle.

5.3 Radial Focusing Frequency

The differential probe plots of Figure 5-14 show a large coherent oscillation. This coherent oscillation is produced by the initial centering error mentioned in section 5.2. The radial focusing frequency is related to the number of turns in a cycle, N_r, by;

$$\nu_r = 1 + \frac{1}{N_r} .$$

As can be seen in Figure 5-14 the number of turns in a cycle cannot be counted directly, because beyond 10." the spacing between turns is comparable to the thickness of the differential wire on the probe. Since we do know the relationship between energy and radius, we can estimate the number of turns in a cycle using,

$$N_r = \frac{E_2 - E_1}{3(q/A)V_{dee}\,Cos(\phi)} . \qquad (5-3)$$

Given in Figure 5-15 is the computed ν_r versus radius for the $^{22}Ne^{8+}$ 35 MeV/A field, along with the experimental values. The horizontal bars indicate the radial interval over which the number of turns is calculated, and the vertical bars indicate the error in the average ν_r value arising from the possible error in determining the radii. Each data point is determined by measuring the radius of the

beginning of a precession cycle and the radius of the end of the cycle. Then an equilbrium orbit program is used to determine the energies for the two radii, and the average value of cos(ø) in this range.

5.4 Axial Focusing Frequency

The head of the main probe is divided into three equal vertical sections, each 0.25" high. For these measurements a large coherent oscillation is induced by placing a .455" shim under the spiral inflector, thus moving the position at which the beam exits the inflector off the median plane. Plotting the current on each of the sections as the probe is drawn outwards gives a profile of the vertical position of the beam spot. In Figure 5-16 the current on the center and lower jaw are plotted over a 10" radial range. As can be seen in the figure the current moves back and forth between the two jaws. The negative values of the current result when electrons are knocked from the jaw, since the electron trapping system is only effective on the sum of the three jaws. From plots such as Figure 5-16 the number of vertical oscillations over a radial range can be determined. The number of turns in the same range can be determined using equation 5-3. The number of turns in a complete cycle of the axial motion is related to the focusing frequency:

$$N_z = \frac{1}{\nu_z} , \qquad \text{if } \nu_z < \frac{1}{2} .$$

The result of these measurements in the $^{14}N^{4+}$ 20 MeV/A field is shown in Figure 5-17 along with the computed values. The horizontal bars give the radial range over which the average value of ν_z is found, while the vertical bar gives the error which arises from incorrectly estimating the number of cycles in the radial range.

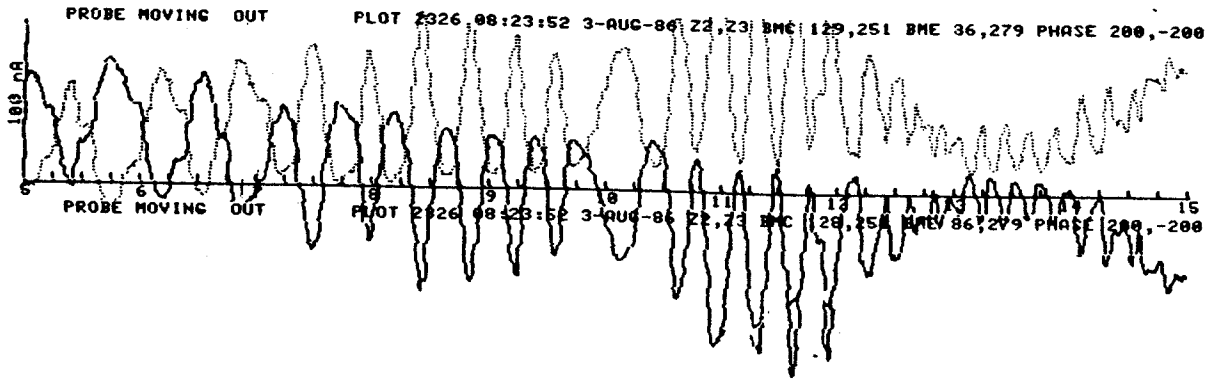

Figure 5-16. The current hitting the center and lower jaw of the main probe as a function of radius. A coherent oscillation is induced in z by raising the inflector 0.445".

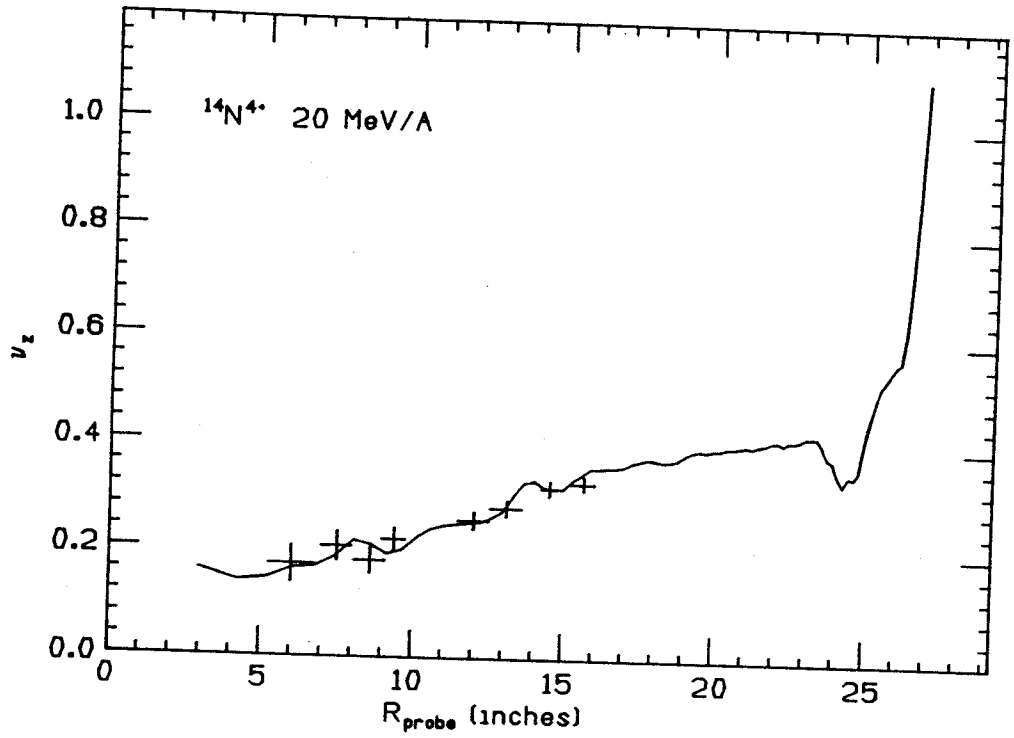

Figure 5-17. The values of the axial focusing frequency as computed by the equilibrium orbit code, and the values obtained from probe traces such as the one shown in Figure 5-14. The horizontal bars indicate the region over which the value of ν_z was averaged. The vertical bars indicate the possible error in determining the number of turns in a precession cycle.

6. Conclusions

If the sucess of a computer program lay solely in its speed, then SOMA will be a huge sucess. In a run such as those done to produce the plots shown in chapter 5, 300 particles were accelerated for approximately 90 turns, using a total CPU time of 15 min. By comparison, a rule of thumb for the orbit integration code SPRGAPZ is, 1 minute to run one particle 100 turns. That is to say a similar run with SPRGAPZ would have used approximately 270 minutes of CPU time, a factor of 18 increase. Of course speed is not the only determining factor. For example flexibility is of great importance. Currently SOMA has several sophisticated input-output (IO) routines, that make the handling of large numbers of particles much easier. The bookkeeping alone would make an orbit integration code run with 300 particles a tedious task. A case in point is the probe option; it reduces the problem of determining the patterns that would be exhibited if there were a given set of orbit conditions, to a trivial problem. With the orbit codes previously available, this was a difficult undertaking, and it seemed

as if one could never run enough particles to get a truly smooth curve.

As with all new programs SOMA will need constant upgrading for some time, as users request more specific features. As mentioned in section 2.6 the equilibrium orbits as calculated between gaps do not close perfectly, and this could be improved by adding an extra iteration to the EO search. Last, but not least, the IO routines could use some cosmetic improvements. In particular, software needs to be developed for the plotting of the calculated probe traces, as the present system is cumbersome and slow.

A transfer matrix program such as SOMA lends itself to the study of several sets of phenomena . two that come to mind immediately are an investigation of beam conditions that lead to better extraction, and an investigation of centering. Obviously for the centering study SOMA will not be useful for the first few turns, and care must be taken when displacements are large. Nevertheless centering often takes over 50 turns, and is phase dependant, so the increased speed of SOMA would be useful. It may also be possible to use SOMA, along with other programs, to determine the centering error from a probe trace. The situation for extraction studies is very similar. Again a

large number of particles needs to be run since the radial-longitudinal coupling is very important. Also the region of interest (the two resonance crossings), requires close to 100 turns, so the turn number times the number of particles is very high.

The results presented in section 5.2 show basic agreement with the computations, which suggests that the calculations presented in chapter 3 could be expanded upon using SOMA. The programs also show that with the correct operating conditions it is possible to achieve a narrow phase width. Combined, the computations and the experiments show that phase selection in the K500 is feasible. Naturally this leads one to wonder about the possibility of single turn extraction, which Figure 3-13 suggests is theoretically possible. In practice it will require considerable effort. For example the small, slow oscillation of the main coil currents in time must be reduced if sufficient stability is to be maintained. At the same time a large effort is needed to reduce the centering error which appears to arise from the central region. On the mechanical side, these studies could be made considerably easier if the main probe were improved. In particular, correctly calibrating the probe, reducing the vertical bounce as the probe moves, and improving the electron traps on the jaws, are all things

that would make probe data more reliable. From a practical point of view, if the phase selection system is to be useful for beams other than those produced in copious amounts by the ECR, the transmission into the cyclotron has to be improved. Separated turns (and single turn extraction) would be helped significantly by reducing the initial emittance. Perhaps this can be done by reducing the inflector collimator to 2 mm in diameter, but again this would result in unacceptably low beam currents unless the transmission improves.

It is probably fair to say, that in most cases the computed values are more easily interpreted than the measured ones, but often ignore important machine conditions. When it comes to making measurements in the K500 it can be very difficult to achieve repeatable results, so there will always be a need for both computational and experimental studies of the K500. Now that the basics of phase selection are understood and confirmed, it is hoped that much further progress towards single turn extraction can be made.

APPENDICES

APPENDIX I

SOMA INPUT

The input and output to SOMA has been distributed among many FORTRAN IO units in order to simplify modifications. The primary input file (unit 5) contains most of the program switches and the cyclotron parameters. Other information such as the magnetic field, harmonic bumps, and the spiral locations are on separate files. Table 7-1 gives a complete listing of all the IO units used by the program and a short description of the information kept on each one.

The first line of the unit 5 file must contain the values of the two logical variables LMATRICES and LPROBE, in that order. If LMATRICES is true then the run begins by calculating the transfer matrices requested on unit 11, otherwise the program attempts to read the transfer matrices from units 51 and 52. When LPROBE is true then the program will either calculate or read in (again depending on the value of LMATRICES) the transfer matrices for the main probe. Following this first line are any number of lines containing the values of various input parameters. Each line

Table 7-1. -- The input-output units used by SOMA.

Unit #	Description
INPUT	
5	input parameters
11	initialization of transfer matrix computation
12	initial conditions
13	spiral locations
14	harmonic field bump data
44	magnetic field
OUTPUT	
30	orbit parameters of particles which hit flags
31	printout at constant theta
33	probe output (binary)
34	printout at gap locations
35	printout at end - for restart
BOTH	
51	gap to gap matrices (binary)
52	constant theta matrices (binary)
53	main probe matrices (binary)

begins with the number (between 1 and 50) of the input parameter being set. All input parameters have default values so only those differing from the default need be entered. The parameters may appear in any order and the list is terminated by a "-1". The input parameters divide into three groups. Those with ID numbers 1 through 9 give the descriptions of the probes and flags to be used. The parameters 10 through 34 are all single entry real numbers while 35 through 50 are single integer values, so this last group contains most of the switches.

Input parameter number 2 is used to indicate the number of flags to be described. Immediately following the line which began with a "2" there must be one line containing the values of; θ_f, ITYPE, RMIN, RMAX, for each flag. The flag is assumed to be located at angle θ_f and is only in effect when the orbit radius lies between RMIN and RMAX. The flag angle must have a transfer matrix, but many flags can share the same matrix if they have the same azimuth. Up to 20 flags may be requested. There are three types of flags. The first type (ITYPE =1) is called a transparent flag. In this case when the orbit radius lies inside the flag, then the orbit parameters are saved but the orbit is unaffected. If ITYPE is 2 then the flag is opaque, in which case when RMIN <

$R(\theta_f)$ < RMAX then the orbit parameters are saved, the particle is considered lost, and the program proceeds to the next particle in the input distribution. When ITYPE=3 then the orbit parameters at θ_f are recorded on unit 31 whenever the particle radius lies inside the flags range.

A line beginning with a 3 contains information on the snapshots to be produced at the end of the run. A snapshot is a scatter plot of any two of the possible 9 orbit parameters. A snapshot will be produced for the initial conditions, the final conditions, and all flags of types 1 and 2. For each snapshot desired a pair of integers are given, with the first integer specifying the orbit parameter to be put on the horizontal axis, and the second doing the

Table 7-2. -- The ID codes for each of the parameters that are saved.

ID	Parameter	Description
1	r	orbit radius
2	p_r	radial component of the momentum
3	z	vertical position
4	p_z	vertical component of the momentum
5	τ	time
6	E	energy
7	x	displacement in radius from the EO
8	p_x	displacement in p_r from the EO
9	$\bar{\phi}$ = PGAV	average of the phase at the last 6 gaps

same for the vertical axis. The labeling of the various parameters is given in Table 7-2. For example the line "3, 1, 2, 9, 1, " would produce scatter plots of p_r vs r and r vs ϕ at the run's conclusion.

The "4" line provides the description of the probes to be considered during the run. A maximum of two probes, one radial and the other the main probe are allowed. The parameters on the '4 card' are;

4, NP, R_i, R_f, ΔR, IBIN, ΔBIN, ΔDIFF, θ, THICK.

Probe information will be accumulated between R_i and R_f, with a bin size of ΔR. IBIN determines if a second parameter is to be binned as well. If IBIN=1 no other binning is done. When IBIN is 2, z is binned and when IBIN=3 the phase is binned. ΔBIN is the bin size for the z or phi bins (up to 60 phi bins are available). When NP is 1 the probe is radial and it is located at an azimuth θ. On the other hand if NP=2 the main probe matrices are used and θ is ignored. The parameters ΔDIFF and THICK give probe head dimensions as shown in Figure 7-1.

The various possible initial conditions discussed in section 2.5 are selected using parameter 42. A value of 2 for this parameter runs the restart option. In this case

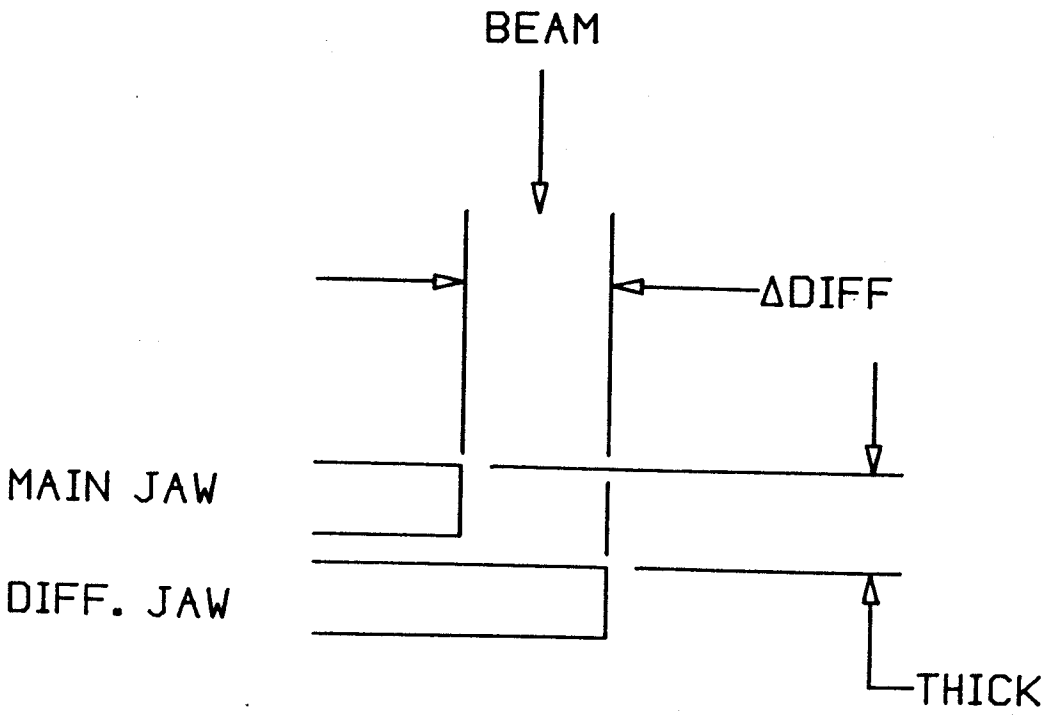

Figure 7-1. A schematic drawing of a probe head, as defined in SOMA. The two dimensions, ΔIDIFF and THICK, are input in inches.

unit 12 contains a line for each particle to be started. The format of these lines is;

d, r, p_r, E, τ, d, d, z, p_z(10X, 3f12.5, f12.6, f12.3, 4f8.4)

where d is a dummy variable. A file which meets these requirements is produced on unit 35 at the end of each run. When IP(42)=1 the program expects the initial conditions to have been generated by a separate program and stored on unit 12. The unit 12 file should contain one line for each particle to be run, with the following format;

Energy, x, p_x, z, p_z, ø (6f12.5).

Table 7-3 shows the remaining possiblities for parameter 42, each of which gives a different method for calculating the initial ellipses.

Table 7-3. -- The source of the initial ellipse values as determined by parameter #42.

IP(42)	X-PX ellipse	Z-PZ ellipse
3	calc. eigen-ellipse	calc. eigen-ellipse
4	calc. eigen-ellipse	input
5	input	calc. eigen-ellipse
6	input	input

The eigen-ellipses are computed for an EO energy equal to the central energy. P(28). The definitions of the various ellipse parameters are given in Figure 7-2. The X-P_x ellipse

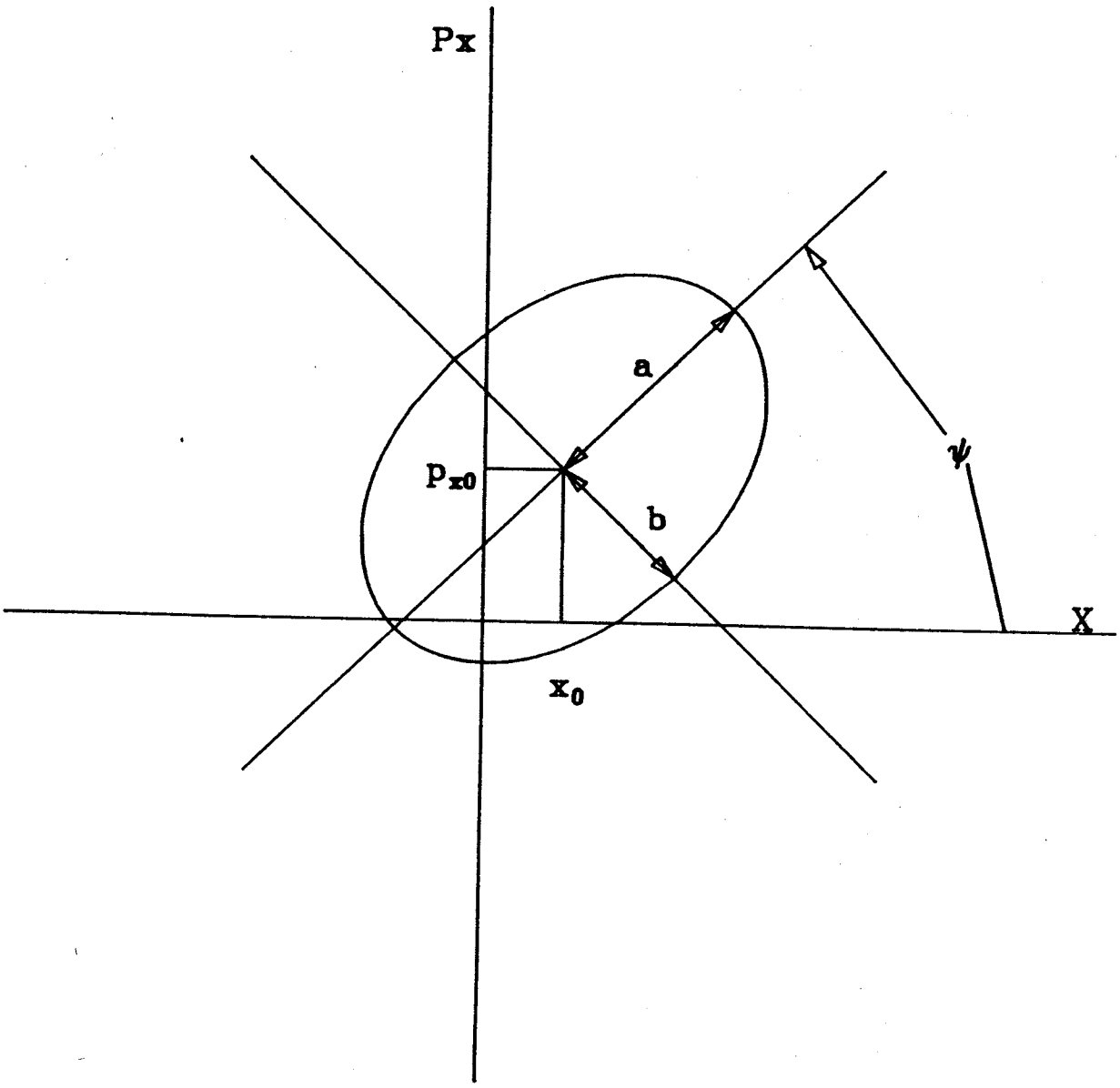

Figure 7-2. An illustration of the meaning of the various initial ellipse parameters. See text for an explanation of how they are input to SOMA.

center (x_o and p_{xo}) can be set in three different manners. If IP(48)=IP(45)=0, then the values of x_o and p_{xo} will be P(30) and P(31) respectively. If IP(48)=0 and IP(45)=1 then the program will calculate the AEO for a particle starting with the central energy, P(28). The AEO is found by running 3 particles for one turn with acceleration. A linear fit is then used to determine the starting condition which will result in the x, p_x values remaining the same after one turn. These initial conditions are then run and the process repeats until the closure is better than 10^{-8} or 10 iterations have been made, which ever comes first. The final method of setting x_o and p_{xo} is to make them a function of the initial phase. If IP(48)=1 then unit 12 contains one line which is,

$$a_1,\ b_1,\ a_2,\ b_2 \qquad (4f12.5).$$

Then

$$x_o = a_1 + (\phi - \phi_r)\ a_2,$$

$$p_{x0} = b_1 + (\phi - \phi_r)\ b_2,$$

$$E = E_{cen} \cos(\phi - \phi_r),$$

where, E_{cen} = P(28) central energy,

ϕ_r = P(29) reference phase.

A full ellipse is started for each value of the phase (ϕ), where the phase, ϕ, is;

$$\phi = \phi_0 + i \times \Delta\phi, \qquad i=0, n\phi-1,$$

where,

$$\phi_0 = P(27), \quad \Delta\Phi = P(26), \quad \text{and } n\phi = IP(41).$$

When IP(44)=1 then ϕ_0 is calculated. The calculation is performed using;

$$\sin(\phi_1) = \sin(\phi_0) + \frac{2\pi h}{\delta E} \int_{E_0}^{E_1} \left(\frac{\omega}{\omega_0} - 1 \right) dE$$

so ϕ_1 is the phase at $E_1 = E_{cen}$, when ϕ_0 is the phase at the first energy E_0 at which transfer matrices are stored. The new value for ϕ_0 (to be used as described above to determine the starting phases) is computed to be;

$$\phi_0 = \phi_1 - P(26) \times IP(41)/2,$$

so that the phase group is centered about the phase given by an EO code.

Table 7-4 contains a listing of the input parameters 10 through 50 and their default values. It should be noted that the RF frequency is,

$$\omega_{rf} = h\,(1+\epsilon)\,\omega_0 \quad \text{if,} \quad \omega_0 = q\,B_0/m,$$

where ϵ is the frequency error and h is the harmonic number. Parameters 16, 17, 18 are a, b, ψ respectively for the X-P_x ellipse, while 20, 21, 22 are the same for the Z-P_z ellipse. The area per point (#24) is the area assigned to each particle in the uniform distribution, so there are approximately $\pi ab/P(24)$ particles populating the ellipse. The number of transfer equations (#39) is explained in Table 2-4. When IP(40) is zero the Z-P_z ellipse is uniformly populated. If it is one then the X-P_x ellipse is uniformly populated, and a value of 2 causes both ellipses to be uniformly populated. Those ellipses not uniformly populated will be randomly populated. IP(46) is used to stop the printing of the initial particle parameters in the log file (unit 6). IP(47) determines whether the gap correction is done to first or second order.

Unit 11 is read whenever transfer matrices are to be calculated. The five lines in this file contain;

E_i, ΔE, NE

N_ANGLE

TH_ANGLE(i), i=1, N_ANGLE

N_EQU

q, B_o, NSEC, NR, NSW

Matrices will be computed for the energies,

$$E = E_i + \Delta E \times i, \qquad i=0, NE-1.$$

N_ANGLE is the number of fixed angles for which transfer matrices will be calculated. Up to 10 fixed angles may be requested. The next line contains the azimuths of the fixed angles, and these must fall on a regular 2^0 Runge-Kutta step. When N_EQU is 1 only the first order transfer matrices are computed and stored, but when N_EQU=2 the full second order transfer matrices are calculated. The final line gives the particle charge in units of e, the central field, the number of sectors, and the number of radius values at which the field is stored. If NSW is non-zero the magnetic field is assumed to have a header which is concluded by an end of file mark.

The magnetic field is input on unit 44. This file begins with a header of up to 10 lines, concluded by an end-of-file mark. Following this is the magnetic field values in a regular r, θ grid. The data is stored so that theta varies most rapidly. The theta step size is one degree and there 120 theta values if NSEC=3 and 360 theta values if NSEC=1. The input format is 8F9.5 and there are NR radius values beginning at R=0.0" and increasing in 0.5" steps.

The gap locations are given on unit 13. The first record is,

NRGP, R0, ΔR (I5, 2F10.5).

The gaps themselves are given in the subsequent records as a table of angles,

$\theta_1(R0)$, $\theta_2(R0)$ (2F12.5)

$\theta_1(R0+\Delta R)$, $\theta_2(R0+\Delta R)$

⋮ etc. ⋮

(NRGP entries in the table).

θ_1 is the entrance to dee1 and θ_2 is the exit (gap2). It is assumed that there are 3 dees evenly spaced around the machine, so 6 gaps are defined. The θ vs R function for a gap is assumed to be linear between data points (a spiral in real space) for the purpose of interpolation and differentiation. There must be at least two r values, and any orbit to be computed must be between the r limits of the gap table. It is advisable to keep the table interval small enough that large discontinuities in the derivative are avoided. There is no restriction on the value of θ, but the following θ values must satisfy these conditions:

$$\theta_2(r) > \theta_1(r) + 10^0$$

$$\theta_2(r) - \theta_1(r) < 110^0$$

$$| \theta(r+\Delta r) - \theta(r) | < 90^0.$$

These limits ensure that no two spiral lines fall in the same integration step, and there is no +/- 360^0 ambiguity in the table. Note that in most cases, a table with only two r values would require more than a 90^0 difference in successive theta values. Gap print-outs are done at the gaps;

IG = IG0 +IDG × i, i=0, ng-1

where,

IG0= IP(37), IDG=IP(36), and ng=IP(38).

These print-outs appear on unit 34, and if a large number of particles are run this file can become extremely large.

When IP(49) is different from zero then the program expects information about the harmonic field bumps to be located on unit 14. The file should contain;

b_1, b_2, ϕ_1, ϕ_2 (4F9.5)

R0, ΔR, NR (2F, I5)

BUMP1(i) i=1, NR (8F9.5)

BUMP2(i) i=1, NR (8F9.5)

where b_1 and ϕ_1 are the amplitude and angle of the first harmonic bump, and b_2 and ϕ_2 are the same but for the second harmonic bump. The bump field will be specified at the radial positions:

Table 7-4. -- The input parameters 10 through 50, that are entered on unit 5. The default values are in brackets.

PARAM(10)	DEE VOLTAGE (KV)	0.00000 (50.00000)
PARAM(11)	HARMONIC NUMBER	1.00000 (1.00000)
PARAM(12)	FREQUENCY ERROR	0.00000 (0.00000)
PARAM(13)	PHASE ERROR OF DEE1 IN DEGREES	0.00000 (0.00000)
PARAM(14)	PHASE ERROR OF DEE2 IN DEGREES	0.00000 (0.00000)
PARAM(15)	PHASE ERROR OF DEE3 IN DEGREES	0.00000 (0.00000)
PARAM(16)	X RADIUS OF ELLIPSE (INCHES)	0.01071 (0.01000)
PARAM(17)	PX RADIUS OF ELLIPSE (INCHES)	0.01071 (0.01000)
PARAM(18)	TILT OF X-PX ELLIPSE (DEG)	0.00000 (0.00000)
PARAM(19)	AREA OF X-PX ELLIPSE (MM-MRAD)	9.14804 (5.00000)
PARAM(20)	Z RADIUS OF ELLIPSE (INCHES)	0.01071 (0.01000)
PARAM(21)	PZ RADIUS OF ELLIPSE (INCHES)	0.01071 (0.01000)
PARAM(22)	TILT OF Z-PZ ELLIPSE (DEG)	0.00000 (0.00000)
PARAM(23)	AREA OF Z-PZ ELLIPSE (MM-MRAD)	9.14804 (15.00000)
PARAM(24)	AREA PER POINT (IN**2)	0.00500 (0.00500)
PARAM(25)	+/- % DELTA E	0.00000 (0.00000)
PARAM(26)	INCREMENT IN PHASE (DEG)	1.00000 (1.00000)
PARAM(27)	PHASE OF FIRST GROUP (DEG)	0.00000 (0.00000)
PARAM(28)	CENTRAL ENERGY (MEV)	0.00000 (0.00000)
PARAM(29)	REFERENCE PHASE (DEG)	0.00000 (0.00000)
PARAM(30)	DELTA X (IF 45=0)	0.00000 (0.00000)
PARAM(31)	DELTA PX (IF 45=0)	0.00000 (0.00000)
PARAM(35)	NUMBER OF TURNS	50 (100)
PARAM(36)	SPACING BETWEEN GAP PRINTS	1 (1)
PARAM(37)	INITIAL GAP PRINT	1 (1)
PARAM(38)	NUMBER OF GAP PRINTS	1 (0)
PARAM(39)	NUMBER OF TRANSFER EQUATIONS	6 (6)
PARAM(40)	IF 0 THEN Z-PZ UNIFORM	1 (1)
PARAM(41)	NUMBER OF PHI GROUPS	1 (1)
PARAM(42)	INPUT DATA TYPE	1 (3)
PARAM(43)	RANDOM NUMBER SEED	249279641 (249279641)
PARAM(44)	IF NE 0, CALC PHI INITIAL	0 (0)
PARAM(45)	IF 1 THEN USE ACCEL EO	0 (0)
PARAM(46)	IF 1 SUPRESS INITIAL PRINT	0 (0)
PARAM(47)	ORDER OF GAP CORRECTION	2 (2)
PARAM(48)	IF 1 READ ELLIPSE CENTER	0 (0)
PARAM(49)	IF 1 USE FIRST HARM. BUMP	1 (0)
FINAL VALUE OF RANDOM NUMBER SEED WAS		249279641

$$R = R0 + i \times \Delta R \qquad i=0, NR-1.$$

The product $b_1 \times$ BUMP1(i) should give the first harmonic component of the field at the radius step i in kilogauss.

APPENDIX II

ORBIT CODE PARAMETERS

Chapter 2

All tests were run in a K500 magnetic field trimmed for 30 MeV/u $^{12}C^{4+}$. The central field was B_0=34.50535 kG, and the RF voltage was V_{dee}=60.4 kV. The field had perfect 3 fold symmetry and the RF frequency was equal to B_0. When not specified test runs began at E=11.0 MeV/u. All tests with acceleration began with ø=0.0. The z motion study began at E=5.0 MeV/u and ran for 300 turns.

Chapter 3

The PIG cases were run in the K500 30 MeV/u $^{12}C^{4+}$ field with B_0=34.50535 kG and V_{dee}=60.4 kV. The ECR case studies were done in a K500 field for 25 MeV/u $^{16}O^{4+}$, with B_0=42.20057 kG, and V_{dee}=73.06 kV. Except where noted, the magnetic fields had perfect three fold symmetry.

Chapter 5

Comparision to the experimental results in section 5.2 was done in a K500 field for 20 MeV/u $^{12}N^{4+}$, which has B_0=33.3192 kG, V_{dee}= 51.5 kV, and 3 fold symmetry. The initial phase width was -18^0 to 2^0 at E=0.38717 MeV/u. The centering conditions using the technique of Figure 2-3 are,

$$x_0 = -0.034 - 0.0033(\phi - \phi_r)$$

$$p_{x0} = +0.030 - 0.0061(\phi - \phi_r)$$

$$E = E_{cen}\cos(\phi - \phi_r)$$

$$\phi_r = -13.0^0$$

$$E_{cen} = .38717 \text{ MeV/u.}$$

The relative densities of the different starting times was determined using Figure 5-3 for the case of 100π initial emittance and a small first turn slit.

REFERENCES

REFERENCES

1. H.G. Blosser, "The Michigan State University Superconducting Cyclotron Program", IEEE Trans. NS-26(2), 2040(1979).
2. H.G. Blosser and F. Resmini, "Progress Report on the 500 MeV Superconducting Cyclotron", IEEE Trans. NS-26(3), 3653(1979).
3. M.L. Mallory, "Initial Operation of the MSU Superconducting Cyclotron", IEEE Trans. NS-30(4), 2061(1983).
4. H.G. Blosser, 9th Int. Conf. on Cyclotrons and their Appl., G. Gendreau, ed., Les Editions de Physique 147, (1981)
5. J. Riedel, "RF Systems", IEEE NS-26(2), 2133(1979).
6. J. Riedel, "Three Phase RF Systems for Superconducting Cyclotrons", IEEE Trans. NS-30, 3452(1983).
7. F. Marti, to be published in the procedings of the 11th Int. Conf. on Cyclotrons and their Appl., Tokyo (1986).
8. M.M. Gordon, "Effects of Spiral Electric Gaps in Superconducting Cyclotrons." NIM, 169, 327(1980).

REFERENCES

1. H.G. Blosser, "The Michigan State University Superconducting Cyclotron Program", IEEE Trans. NS-26(2), 2040(1979).
2. H.G. Blosser and F. Resmini, "Progress Report on the 500 MeV Superconducting Cyclotron", IEEE Trans. NS-26(3), 3653(1979).
3. M.L. Mallory, "Initial Operation of the MSU Superconducting Cyclotron", IEEE Trans. NS-30(4), 2061(1983).
4. H.G. Blosser, 9th Int. Conf. on Cyclotrons and their Appl., G. Gendreau, ed., Les Editions de Physique 147, (1981)
5. J. Riedel, "RF Systems", IEEE NS-26(2), 2133(1979).
6. J. Riedel, "Three Phase RF Systems for Superconducting Cyclotrons", IEEE Trans. NS-30, 3452(1983).
7. F. Marti, to be published in the procedings of the 11th Int. Conf. on Cyclotrons and their Appl., Tokyo (1986).
8. M.M. Gordon, "Effects of Spiral Electric Gaps in Superconducting Cyclotrons." NIM, 169, 327(1980).

9. C.J. Kost and G.H. Mackenzie, "COMA a Linear Motion Code for Cyclotrons," IEEE NS-22, 1922(1975).

10. J.C. Collins, "Phase Selection Mechanisms in Isochronous Cyclotrons Producing High Resolution Beams", Ph.D. thesis, Michigan State University, 1973, pg. 1.

11. B.F Milton et al., "Design of Beam Phase Measurement and Selection System for the M.S.U. K500 Cyclotron", Proc. 10th Int. Conf. on Cyclotrons and their Appl., F. Marti ed., 55,(1984).

12. K.L. Brown, "A First and Second Order Matrix Theory for the Design of Beam Transport Systems and Charged Particle Spectrometers." Adv. in Particle Phy. 1, 67,(1967).

13. M.M. Gordon, "Computation of Closed Orbits and Basic Focusing Properties for Sector Focused Cyclotrons and the Design of 'CYCLOPS'", Particle Accelerators, 16, 39(1984).

14. P. Kramer, H.L. Hagedoorn and N.F. Verster, "The Central Region of the Phillips AVF Cyclotron", Proc. of the CERN Cyclotron Conference 193,(April 1963).

15. S. Gill, "A Process for Step-by-Step Integration of Differential Equations in an Automatic Digital Computing Machine", Proc. Cambridge Philos. Soc., 47, 96(1951)

16. M.M. Gordon, "Green's Function for the Mathieu-Hill Equation", internal NSCL memo, June 1985.

17. M.M. Gordon, "Notes for 2nd Order Transfer Matrix Code", internal NSCL memo, 1986.

18. R.E. Berg, "Precise Methods for Pre-Calculation of Cyclotron Control Settings", Ph.D. Thesis, Michigan State University, 43 (1966).

19. M.M Gordon and T.A. Welton, ORNL-2765 (1959).

20. M.M. Gordon, "Possible Treatment of Field Bump Effects Within a Transfer Matrix Code", internal NSCL memo, Feb 2 1986.

21. M.M. Gordon, "Single Turn Extraction" IEEE Trans. NS-13(4), 48 (1966).

22. Loc. Cit. 10, pg. 12.

23. Ibid. pg. 3

24. F. Marti, "Design of the Axial Injection System for the NSCL Cyclotrons" IEEE Trans. NS-32(5), 2450(1985).

25. T.I. Arnette, "Program CYCLONE", Michigan State University internal report (1966).

26. Loc. Cit. 10, pg. 43.

27. W.B. Wilson et al., "Beam Diagnostics and Improvements at TAMVEC", IEEE Trans. NS-18(2), 299(1971).

28. M.M. Gordon, "Canonical Treatment of Accelerated Orbits in Sector-Focused Cyclotrons" Part. Accel. 12, 13(1982).

29. Loc. Cit. 20, pg. 51.

30. M.M. Mallory, to be published, in the procedings of the 11th International Conf. on Cyclotrons and Their Appl. Tokyo (1986).

31. Garren and Smith, "Diagnosis and Correction of Beam Behavior in an Isochronous Cyclotron", Proc. of the Int. Conf. on Sector Focused Cyclotrons and Meson Factories. Cern, April 1963.

32. R.E. Berg, "Precise Methods for the Pre-Calculation of Cyclotron Control Settings", Ph.D. Thesis, Michigan State University, 1966, pg. 86.

33. Ibid. pg. 87.

34. F.Marti et al, "Effect of Orbit Centering and Magnet Imperfections on Beam Properties in a Superconducting Cyclotron", Proc. 10th Int. Conf. on Cyclotrons and their Appl., F. Marti ed., 46, (1984).

35. M.M. Gordon, "Perturbation of Radial Oscillations in Superconducting Cyclotrons Due to Asymetric Dee Voltages and Phases", IEEE Trans. NS-30, 2439(1983).

36. M.M. Gordon and V. Taivassalo, "The Z^4 Orbit Code and the Focusing Bar Fields Used in Beam Extraction Calculations for Superconducting Cyclotrons", NIM A247, 423(1986).

37. D.A. Johnson and H.G. Blosser, "Computor Program for Tracking of Linear Cyclotron Orbits", Michigan State University Internal Report MSUCP-4(1960).